eXPRESS Polymer Letters Vol.4, No.2 (2010) 54
Available online at www.expresspolymlett.com
DOI: 10.3144/expresspolymlett.2010.9

Editorial corner – a personal view

Purposeful surface treatment of nanoparticles for tuning structure and properties of polymer based nanocomposites

*M. Q. Zhang**

Materials Science Institute, Zhongshan University, Guangzhou 510275, P. R. China

Polymeric nanocomposites have been an area of intense industrial and academic research for the past twenty years. As viewed from literature, however, the properties of nanocomposites are sometimes not significantly improved or even worse than those of the matrices. This used to result from direct incorporation of nano-scale building blocks into polymers. Because of the strong tendency of nanoparticles to agglomerate, nano-size fillers are hard to be uniformly dispersed in polymers by conventional techniques. In this context, surface modification of the nano-fillers, that is able to increase hydrophobicity of the inorganic fillers, enhance interfacial adhesion via physical interaction or chemical bonding, and eliminate the loose structure of filler agglomerates, should be a key issue.

Comparatively, the achievements in modern chemistry (incl. grafting techniques, click chemistry, non-covalent bonding, etc.) are much more prominent than those in compounding techniques. Therefore, there are enormous possibilities for modifying nanoparticles. The combination of different surface treatment methods with existing mixing machines would generate nanocomposites with tailor-made structure and performance and enrich the measures of nanocomposites manufacturing.

In general, homogeneous dispersion of the fillers is considered to be the main concern, but in fact, it can not guarantee good properties of the nanocomposites. In addition to the dispersion, filler/matrix interaction and filler/filler interaction exert critical influence on the composites properties. A proper surface functionalization approach should take account of all these issues and eventually leads to the optimal microstructure with the help of carefully designed processing parameters.

Naturally, a problem has arisen: what is the desired arrangement of the nanoparticles in matrix according to different properties requirements? So far, theoretical consideration of the mechanisms involved in nanocomposites with adequate predictability is relatively less reported. Design and production of polymer nanocomposites have to be mostly conducted on a trial and error basis. Empirical extrapolation of the parameters related to components selection and processing technique is not very successful.

On the basis of analysis hereinbefore, it can be concluded that one has to firstly have a clear image of the proposed nanocomposites and the microstructure, and then start to work out a feasible route of surface treatment of nanoparticles and the way of compounding. The importance of each step mentioned above should be equally considered.

Prof. Dr. Ming Qiu Zhang
Member of International Advisory Board

*Corresponding author, e-mail: ceszmq@mail.sysuedu.cn

eXPRESS Polymer Letters Vol.4, No.2 (2010) 55–61
Available online at www.expresspolymlett.com
DOI: 10.3144/expresspolymlett.2010.10

Mechanical properties and environmental stress cracking resistance of rubber toughened polyester/kenaf composite

N. N. Bonnia[1], S. H. Ahmad[2], I. Zainol[3], A. A. Mamun[4], M. D. H. Beg[5], A. K. Bledzki[4]*

[1]Material Technology Department, Faculty of Applied Sciences, Universiti Teknologi Mara (UiTM), 40450 Shah Alam, Selangor, Malaysia
[2]Department of Material Science, Faculty of Applied Physics, Universiti Kebangsaan Malaysia, 43600 Bangi, Selangor, Malaysia
[3]Chemistry Department, Faculty of Science and Technology, Universiti Sultan Idris 35900 Tanjung Malim, Perak, Malaysia
[4]Institute of Material Engineering, University of Kassel, Moncheberg str. 3, 34125 Kassel, Germany
[5]Faculty of Chemical and Natural Resources Engineering, Universiti Malaysia Pahang, Kuantan, Malaysia

Received 10 June 2009; accepted in revised form 29 October 2009

Abstract. In this study rubber-toughened polyester-kenaf fibre composites were prepared by adding various percentages of kenaf fibre in unsaturated polyester resin and subsequently cross linked using a mixture of organic peroxide methyl ethyl ketone and cobalt octanoate. Three percent (3%) of liquid natural rubber (LNR) were added as a toughening agent. The mechanical properties of the composites were evaluated by impact and flexural testing. Environmental stress cracking resistance (ESCR) of polyester-kenaf composite in acid and base medium was also studied. It was found that the addition of LNR increased impact strength by about 66% and flexural strength by 70%. Measurement of ESCR shows that the composite has the fastest diffusion rate in acid medium, followed by that in base medium and then without medium. Bonding mechanisms were assessed by scanning electron microscope and FTIR analysis.

Keywords: *polymer composites, polyester, toughened, liquid natural rubber (LNR), kenaf*

1. Introduction

In recent decades, growing environmental awareness has resulted in renewed interest in the use of natural materials for various applications. Increasingly more stringent environmental policies have forced industries such as the automotive, packaging and construction industries to search for new materials that can substitute traditional composite materials consisting of a plastic matrix and inorganic reinforcement [1]. The availability of bio-based structural composites offer the opportunity for environmental gains, reduced consumption of more expensive materials, lighter weight, improved insulation and sound absorption properties, and reduction in dependence on petroleum-based and forest product materials. The production of synthetic fibres, such as glass, aramid and carbon fibres, are energy-intensive and are petroleum based. Kenaf, *Hibiscus cannabinus* L. fiber is obtained from renewable resources, which is biodegradable, environmentally friendly and offer CO_2 neutral life cycle [2]. The most rapidly expanding application for kenaf at present is as reinforcement in composites. The matrix materials popularly used in kenaf fibre composites ranges from thermoplastics, such as polypropylene and polyethylene, to thermosets, such as polyester, epoxy [3–5].

*Corresponding author, e-mail: najlinn@yahoo.com

Unsaturated polyester resins are the most frequently used thermosetting system owing to their low cost and adaptability to be transformed into large composite structures. The most frequently used reinforcement in this system is provided by sized glass fibres available as fabrics of various orientation, shapes and densities. More recently, the possibility of using cellulosic fibres as reinforcement in composites has yielded several studies. For instance, Dash *et al.* [6] reported the mechanical properties of jute fibre/unsaturated polyester composites. The authors optimised the fibre loading (60 wt%) that has the maximum tensile strength of 132 MPa and Young's modulus 2.9 GPa for composites. Acha *et al.* [7] used jute fabric to reinforce unsaturated polyester resin. The results showed that the Young's modulus of all the composites increased significantly (fibre content 46 to 56 wt%) tensile strength of the composite was, however, not improved.

Although polyester resins are widely used as a matrix in polymer composites, curing of these resins results in brittleness due to their high cross-linking level. The addition of a low molecular weight reactive liquid rubber can improve fracture toughness and impact strength of the cured polyester resin. The purpose of introducing dispersed rubber particles into the primary phase in these systems is to enhance their toughness. It is known that both rubber particle size and volume fraction affect the degree to which the polyester is toughened [8]. Dahlan *et al.* [9] has extensively studied the utilization of liquid natural rubber (LNR) as a compatibilizer on various natural rubber/polyolefin blends. They found that the LNR has the same microstructure as NR but with short chains of polyisoprene and a different in molecular weight (M_w). The M_w for LNR is around 5000 whereas for NR it is 900 000. The LNR with some active terminals like –OH is expected to react with the plastic particles and thereby bond the plastic particles to the NR matrix. Studies on NR and various PE with LNR as a compatibilizer have successfully shown that LNR can act as plasticizer or cross linking agent, depending on its molecular weight [9, 10]. Therefore, this study investigates the effects of the addition of liquid natural rubber (LNR) and kenaf to a polyester matrix on the mechanical properties of the composites.

2. Material and methods

2.1. Preparation of fibres

The kenaf fibres used had been harvested at 4 months of age. Fibres were then cut and ground with an Ika Werke MF10 heavy duty grinder (Staufen, Germany) and finally sieved into 300–500 micron sizes. The kenaf fibre diameter was 20–55 μm.

2.2. Preparation of the matrix

LNR is prepared according to a method described by Abdullah and Ahmad [11]. The M_w for LNR is about 5000. Unsaturated polyester Reversol UN 8100 P-8542CSH from Revertex Sdn. Bhd., Malaysia was used in this research. For the composites without LNR, the polyester resin was mixed with the initiator methyl ethyl ketone peroxide (MEKP) and cobalt octanoate 1%. For the composite with LNR, the polyester resin and the LNR were stirred for 30 minutes before mixing with the initiator.

2.3. Preparation of composites board

Dried kenaf fibres were measured into 5, 10, 15, 20 and 25% (by weight) and mixed with polyester resin and LNR. The mixture was put into the mould and pressed at 70 MPa pressure at 90°C for 15 minutes. Aziz *et al.* reported that the curing of polyester at different temperatures with different durations ensures full cure and provides better performance [12]. The resulting board was cured at room temperature for 24 hours and post cured successively at 60°C for 2 hours, 90°C for 90 minutes, 120°C for 1 hour and 150°C for 30 minutes. The mechanical properties of each type of board were then evaluated after cutting the samples to the required shape for different test. PK is abbreviation for polyester kenaf composites, PKL is abbreviation for polyester kenaf composites with LNR.

2.4. Composite characterization

Flexural strength was measured under a three-point bending approach using a Universal Testing machine (Testometric 350, UK) according to ASTM D 790-91. The dimensions of the samples were 120 mm×20 mm×3 mm. The distance between

the spans was 100 mm, and the test speed was 5 mm/min. Impact testing was carried out with a Ray Ran Pendulum Impact System (Warwickshire, UK) according to ASTM D 256. Fracture toughness was determined according to ASTM E 399 using a three-point bending flexural test. The test speed was 2 mm/min. For mechanical testing 5 specimens were tested for each batch to get the average values.

Environmental stress cracking resistance (ESCR) tests were carried out using a Universal Testing machine (Zwick 1440, Germany) according to ISO standard 22088-3:2006. Samples were prepared with dimensions of 80 mm×4 mm×10 mm. The specimen was bent using a three-point bending jig mounted in a chemical environment chamber. The test was undertaken in control medium (Air), 1% sodium hydroxide (pH 13.5) and 1% hydrochloride acid (pH 2.5) medium. Three conditions of the environment were used in this test:

– Without medium (om)
– With acid medium (am)
– With base medium (bm)

After t_0, defined as the time necessary to stabilize the loading condition, the chemical was rapidly introduced into the chamber under stress. The variation of the stress was recorded using a sensitive load cell 100 N connected to multimeter incrementally at t_0 = 120 s, t_1 = 120 s, t_2 = 180 s, t_3 = 180 s, t_4 = 300 s, t_5 = 300 s, t_6 = 300 s. When the stressed composite is exposed to a chemical environmental, polymer resistance will vary with time. Since micro crazes, crazes or cracks weaken the chemically exposed polymer, it will tend to have both a shorter time to rupture and a lower stress value in comparison with the control specimen (without medium). The test was carried out under laboratory conditions in an air conditioned room, controlled at 23±°C and 50% relative humidity. The *E* factor was calculated as the stress in control medium divided by the stress in corrosive medium at a certain time.

Morphological observation of the flexural fracture surface of the composite with different compositions was done by a scanning electron microscope (Philips XL 30 ESEM). FTIR spectrum of samples was recorded using FTIR (Perkin Elmer 500, Nicolet 6000, UK) spectroscopy from 4000 to 400 cm^{-1} using KBr disk. 20% kenaf fibre composites were chosen for SEM and FTIR experiment.

3. Results and discussion

3.1. Impact properties

The impact strength of matrix and composites are presented in Figure 1. It can be seen that the impact strength of the matrix was higher than that of the composites with lower fibre content, then the impact strength increased in general with increasing fibre loading. The lower value of impact strength at lower fibre content could be due to the introduction of flaws created by the fibre ends. These flaws act as stress concentrations, and cause the bond between fibre and matrix to break. At higher volume fractions, the matrix is sufficiently restrained and the stress is more evenly distributed. This results in reinforcing effects outweighing the effects of the stress concentrations and results in increase of impact strength at higher fibre loading [13]. Although, benefit was seen in higher fibre loading, however, the fibre loading was limited to 25 wt% due to limited wettability of the resin; and higher than 25 wt% (for example 30 wt%) the polyester resin could not wet the fiber sufficiently and could not penetrate into the fiber mass. The impact test is a standardized high strain-rate test which determines the amount of energy absorbed by a material during fracture. This absorbed energy is a measure of a given material's toughness and acts as a tool to study brittle-ductile transition. The impact strength of composites may also be influenced by many other factors including the toughness of the reinforcement, the nature of the interfacial region, and the frictional work involved in pulling the fibres from the matrix [14, 15]. Addition of liquid natural rubber (LNR) was found to improve the impact properties of composites by 35 to 125%, probably due to the presence of rubber particles in the polyester which may have acted as impact modifier in the composite. The highest impact strength

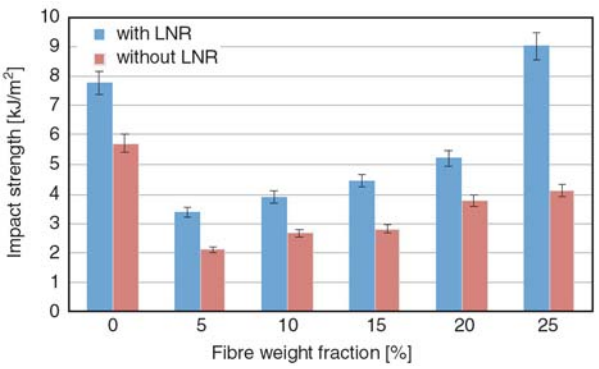

Figure 1. Impact properties of polyester/kenaf composites

was found for 25% fibre loading composites with LNR which was about 125% higher than that of compositions without LNR. It may be the reason that the fibre loading was reached the critical fibre load for this system in which fibres were distributed evenly and absorbed more energy.

3.2. Flexural strength of composite

Figures 2 and 3 present the effects of fibre loading and addition of liquid natural rubber (LNR) on the flexural properties of the polyester kenaf composites. Both flexural strength and modulus were found to be higher than that of composites containing lower amount of fibre loading, however, both flexural strength and modulus were found to be increased significantly as the fibre volume fraction increased. As discussed earlier, at lower fibre content, below critical fibre volume fraction, fibre ends act as stress concentrations, and cause the bond between fibre and matrix to break. At higher volume fractions, the matrix is sufficiently restrained and the stress is more evenly distributed. This results in reinforcing effects outweighing the effects of the stress concentrations and results in increase in flexural strength and modulus [13, 16]. Although, the flexural behavior of composites without LNR tended to behave like composite with LNR, however, generally a slight reduction of strength and modulus were found for composites with LNR. This reduction of flexural properties could be due to the plasticizing effect of rubber particle which increased flexibility and reduced toughness.

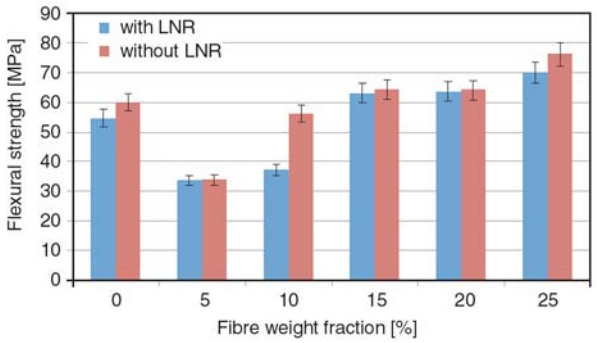

Figure 2. Flexural strength of polyester/kenaf composites

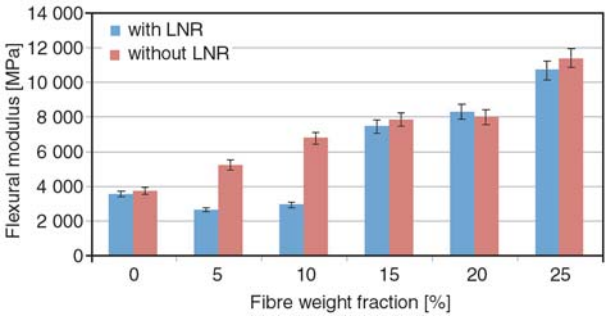

Figure 3. Flexural modulus of polyester/kenaf composites

3.3. Fracture toughness of composite

The crack growth behaviors of composite are compared in Figure 4 based on K_{ic} values. Fracture toughness of composites both with and without LNR were increased with increasing fibre volume, however, the values dropped after 15% of fibre loading for composites without LNR and 20% fibre loading for composites with LNR. The reduction of K_{ic} at higher fibre content composites may be due to increased fibre-fibre contacts which would make it comparatively easier for the fibre to debond from the resin than for composites at lower fibre fraction composites. Therefore, larger force could be required for the fibre to be debonded from the matrix at lower fibre content. The addition of higher percentages of kenaf also could interfere with the cross linking process and decrease the K_{ic} values [3, 17]. It was also noted that the fracture toughness values were higher for composites with LNR which could be due to the plasticizing effect of rubber particle which increased flexibility and needed more force to debonding.

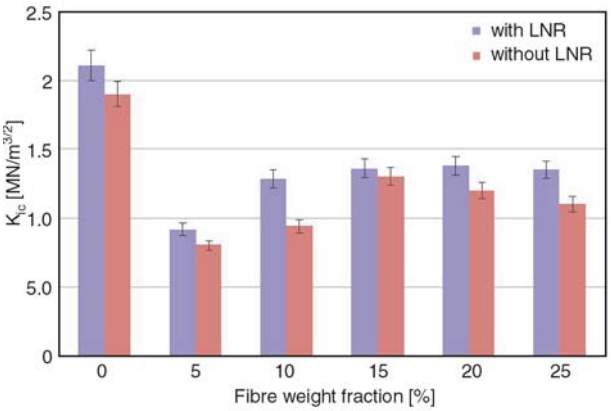

Figure 4. Fracture toughness of composites

3.4. Environmental stress cracking resistance (ESCR)

Environmental stress cracking resistance is the premature initiation of cracking and embrittlement of a plastic due to the simultaneous action of stress and strain in contact with a specific fluid. This phenom-

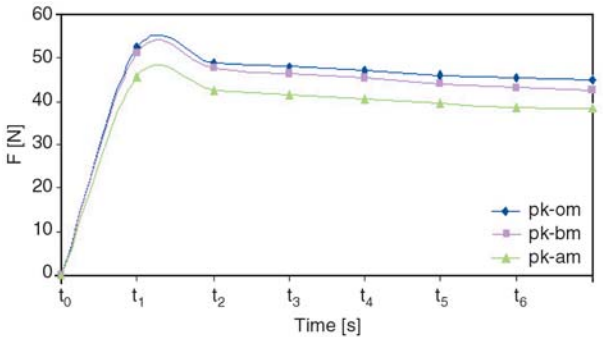

Figure 5. Comparison on ESCR effect of the kenaf composites

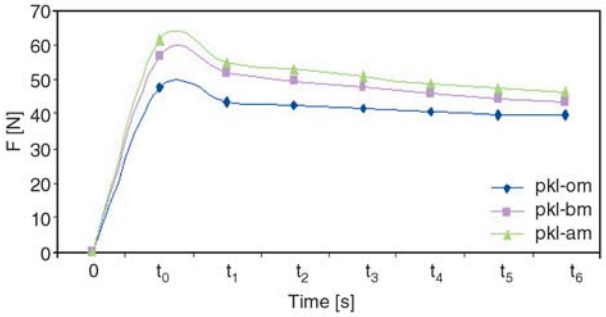

Figure 6. Comparison on ESCR effect of the kenaf composites toughened LNR

enon is also described as environmentally assisted cracking [18]. Figures 5 and 6 show that stress values rapidly decreased, whether the composites had acid or base medium. The stress values of composites without medium declined over time but the reduction was found to be less than that of composites with medium. Both composites, without LNR and with LNR showed the same trend across the three different medium conditions. However, acid medium weakened the composite more rapidly than the base medium. Figure 5 indicates that over time, polyester composite with LNR decreased the stress by 25% with acid medium and 23% with base medium. Figure 6, however, shows that the stress value of polyester composite without LNR decreased 16% on acid medium and 20 % on base medium. The stress value of composites LNR declined about 17% with control medium whiles those composites without LNR declined by about 14%. Figures 5 and 6 reveals that when the stressed composite is exposed to a chemical environment, the polymer resistance to acid and base varies with time. Since micro crazes, crazes or cracks weaken the polymer exposed to chemicals, it will tend to have both a shorter time to rupture and a lower stress value, compared to those of a control specimen without medium. It can also be noted that composites without LNR are more resistant in different chemical environment which could be due to rubber particle may debonded or degraded out from composites more easily than the resin.

3.5. Infrared spectroscopy

A series of Fourier transform infra red (FTIR) spectra were obtained to detect any chemical interaction between polyester-kenaf composites and polyester-kenaf with LNR composites. The FTIR spectra of cured polyester- kenaf composites and polyester-kenaf with LNR composites are shown in Figure 7. A new peak was observed on FTIR spectrum of modified polyester as compared to unmodified polyester. An aromatic functional group (C–C stretch in ring) was observed from the absorption band 1600 and 1475 cm^{-1} and an alkanes group (CH_3) from the absorption band 1376 cm cm^{-1} for composites with LNR [19]. It can be note that the aromatic functional group can also appear from matrix polymer. A hydroxyl group was observed for both peaks from the absorption band 3600–3300 cm^{-1}. It was identified with existing stretching band on 1300–1000 cm^{-1} (C–O) .The carbonyl region (1800–1600 cm^{-1}) reveals probably the presence of carbonyl group from the isoprene chain of liquid natural rubber. Carbonyl absorption was observed in both spectra but with different intensity.

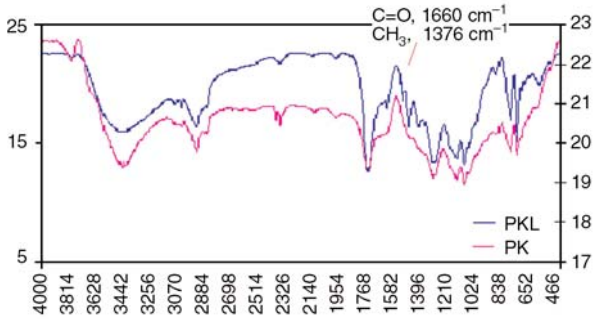

Figure 7. Infrared spectroscopy of the composites

3.6. Morphological analysis

Figure 8 shows the flexural fracture surface of composites. Good bonding was evident from both type composites with and without LNR. Fibre fracture can be seen and there is absence of hole and fibre pullout. However, for composites without LNR, it can be seen a gap between fibre and

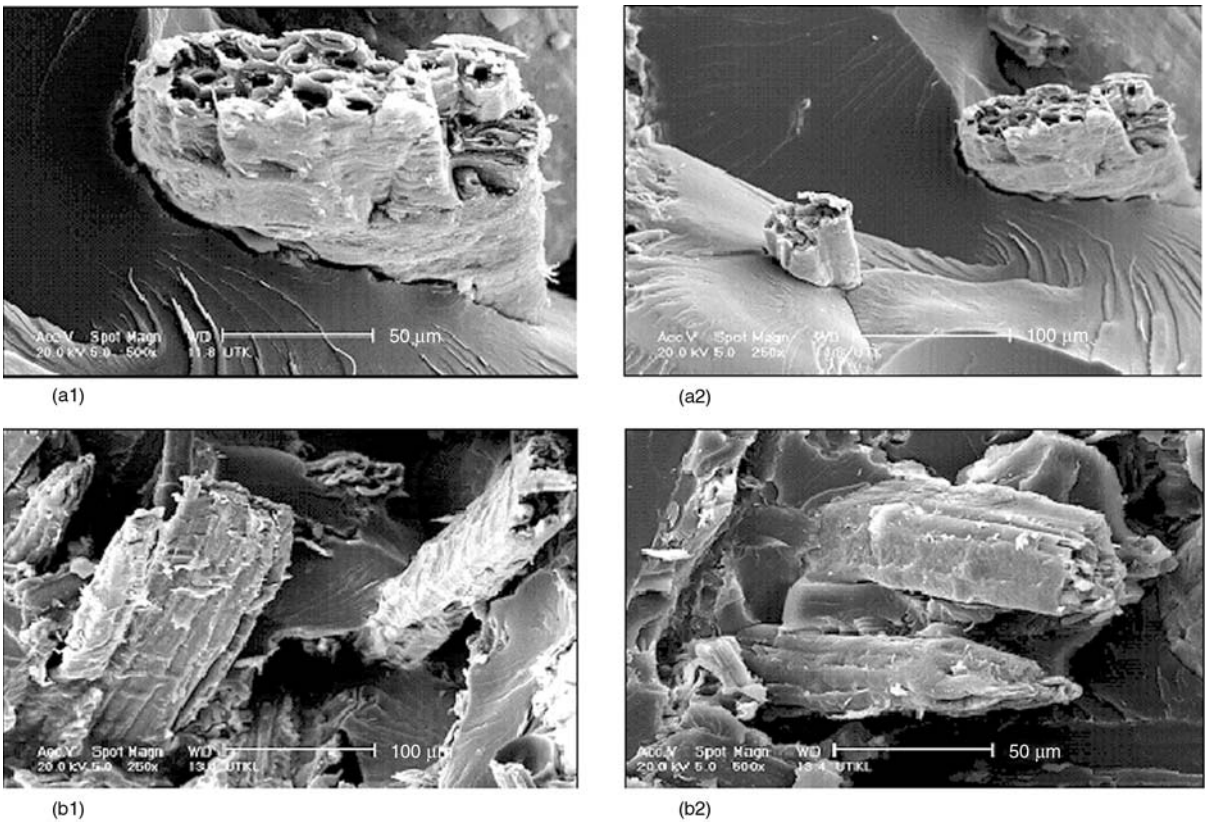

Figure 8. SEM micrograph of composites at 250× and 500× magnifications: (a) polyester-kenaf composites, (b) polyester-kenaf with LNR composites

embedded resin (Figures 8a1 and 8a2). It is well known that unsaturated polyester networks shrink considerably after curing. This shrinkage reduces the specific volume of the matrix, and it results in free spaces between the matrix and the fibre. On the other hand, for composites with LNR the region surrounding the cellulosic filler seems to be continuous with the matrix phase (Figures 8b1 and 8b2).

4. Conclusions

1. The result shows that liquid natural rubber is a good potential toughening agent for polyester resin.
2. Impact, flexural and fracture toughness properties were found be improved significantly with increasing fibre volume faction, however, optimum mechanical properties were found be around 20% fibre loading.
3. Fracture toughness and impact strength of polyester kenaf composite noticeably increased with the addition of a small amount of liquid natural rubber in composites.
4. Environmental stress cracking resistance shows that the composites are more affected on acid medium followed by base medium.

Acknowledgements

The authors acknowledge financial support for this research work from: the Malaysian Ministry of Science and Technology (MOSTI) under ScienceFund 03-01-02-SF0l223; Universiti Kebangsaan Malaysia, Bangi, Malaysia; SIRIM Bhd, Shah Alam, Malaysia; Universiti Technology Mara, Shah Alam, Malaysia; and the Institute of Material Engineering, Sophie Henschel Haus, Plastic and Recycling Engineering, Kassel University, Kassel, Germany.

References

[1] Espert A., Vilaplana F., Karlsson S.: Comparison of water absorption in natural cellulosic fibres from wood and one-year crops in polypropylene composites and its influence on their mechanical properties. Composites Part A: Applied Science and Manufacturing, **35**, 1267–1276 (2004).
DOI: 10.1016/j.compositesa.2004.04.004

[2] Annuar H., Ahmad S. H., Rasid R., Ahmad A., Wan Busu W. N.: Mechanical properties and dynamic mechanical analysis of thermoplastic-natural-rubber-reinforced short carbon fibre and kenaf fibre hybrid composites. Journal of Applied Polymer Science, **107**, 4043–4052 (2007).
DOI: 10.1002/app.27441

[3] Aziz S. H., Ansell M. P.: The effect of alkalization and fibre alignment on the mechanical and thermal properties of kenaf and hemp bast fibre composites: Part 1 – polyester resin matrix. Composites Science and Technology **64**, 1219–1230 (2009).
DOI: 10.1016/j.compscitech.2003.10.001

[4] Bledzki A. K., Mamun A. A., Faruk O.: Abaca fibre reinforced PP composites and comparison with jute and flax fibre PP composites. Express Polymer Letters, **1**, 755–762 (2007).
DOI: 10.3144/expresspolymlett.2007.104

[5] Kafi A. A., Abedin M. Z., Beg M. D. H., Pickering K. L., Khan M. A.: Study on the mechanical properties of jute/glass fiber-reinforced unsaturated polyester hybrid composites: Effect of surface modification by ultraviolet radiation. Journal of Reinforced Plastics and Composites, **25**, 575–588 (2006).
DOI: 10.1177/0731684405056437

[6] Dash B. N., Rana A. K., Mishra H. K., Nayak S. K., Mishra S. C., Tripathy S. S.: Novel, low-cost jute-polyester composites. Part 1: Processing, mechanical properties, and SEM analysis. Polymer Composites, **20**, 62–71 (2006).
DOI: 10.1002/pc.10335

[7] Acha B. A., Marcovich N. E., Reboredo M. M.: Physical and mechanical characterization of jute fabric composites. Journal of Applied Polymer Science, **98**, 639–650 (2005).
DOI: 10.1002/app.22083

[8] Zainol I., Ahmad I. B., Zakaria F. A., Ramli A., Marzuki H. F. A., Aziz A. A.: Modification of epoxy resin using liquid natural rubber. Materials Science Forum, **517**, 272–274 (2006).
DOI: 10.4028/www.scientific.net/MSF.517.272

[9] Dahlan H. M., Khairul Zaman M. D., Ibrahim A.: Liquid natural rubber (LNR) as a compatibiliser in NR/LLDPE blends II: The effects of electron-beam (EB) irradiation. Radiation Physics and Chemistry, **64**, 429–436 (2002).
DOI: 10.1016/S0969-806X(01)00491-1

[10] Ibrahim A., Dahlan H. M.: Thermoplastics natural rubber blends. Progress in Polymer Science, **23**, 665–706 (1998).
DOI: 10.1016/S0079-6700(97)00052-X

[11] Abdullah I., Ahmad S.: Liquid natural rubber as a compatibilizer in the blending of natural rubber with polypropylene. Material Forum, **16**, 353–357 (1992).

[12] Aziz S. H., Ansell M. P.: The effect of alkalizations and fibre alignment on the mechanical and thermal properties of kenaf and hemp bast fibre composites: Part 2 – Cashew nut shell liquid matrix. Composites Science and Technology, **64**, 1231–1238 (2004).
DOI: 10.1016/j.compscitech.2003.10.002

[13] Bibo G. A., Hogg P. J.: The role of reinforcement architecture on impact damage mechanisms and post-impact compression behaviour. Journal of Materials Science, **31**, 1115–1137 (1996).
DOI: 10.1007/BF00353091

[14] Bledzki A. K., Gassan J.: Composites reinforced with cellulose based fibres. Progress in Polymer Science, **24**, 221–274 (1999).
DOI: 10.1016/S0079-6700(98)00018-5

[15] Bledzki A. K., Mamun A. A., Lucka-Gabor M., Gutowski V. S.: The effects of acetylation on properties of flax fibre and its polypropylene composites. Express Polymer Letters, **2**, 413–422 (2008).
DOI: 10.3144/expresspolymlett.2008.50

[16] Sreekala M. S., Jayamol G., Kumaran M. G., Sabu T.: The mechanical perfomance of hybrid phenol-formaldehyde based composites reinforced with glass and oil palm fibres. Composites Science and Technology, **62**, 339–353 (2002).
DOI: 10.1016/S0266-3538(01)00219-6

[17] Ismail H., Shuhelmy H., Edyham M. R.: The effects of a silane coupling agent on curing characteristics and mechanical properties of bamboo fibre filled natural rubber composites. European Polymer Journal, **38**, 39–47 (2002).
DOI: 10.1016/S0014-3057(01)00113-6

[18] Wright D. R.: Environmental stress cracking of plastic. Rapra Technology, Shawbury (1996).

[19] Stuart B.: Biological applications of infrared spectroscopy. Wiley, New York (1997).

eXPRESS Polymer Letters Vol.4, No.2 (2010) 62–70
Available online at www.expresspolymlett.com
DOI: 10.3144/expresspolymlett.2010.11

Evaluating the effect of processing conditions and organoclay content on the properties of styrene-butadiene rubber/organoclay nanocomposites by response surface methodology

I. Ghasemi, M. Karrabi, M. Mohammadi, H. Azizi*

Iran Polymer and Petrochemical Institute, P.O.Box:14965/115, Tehran, I.R. Iran

Received 14 September 2009; accepted in revised form 4 November 2009

Abstract. In this work, basic mathematical models and response surface graphs have been used to illustrate the relationship between mixing parameters in internal mixer and properties of the SBR (styrene butadiene rubber)/organoclay composites. Using a Box-Behnken statistical design experiment methodology, the effects of mixing temperature (80–140°C), mixing time (4–12 min) and nano filler amount (3–9 phr) in SBR nanocomposites on the properties (tensile properties, scorch time and Mooney viscosity) were evaluated. It was found that the mixing parameters (time and temperature) have the predominant role in properties and morphology of nanocomposite. The R^2 values (the R^2 values indicate the degree of agreement between the experimental results with those predicted by model) of all responses were above 0.85. Increasing temperature and mixing time facilitated a better organoclay dispersion which resulted in a better tensile property. With increase in nanoclay amount in composite the scorch time and Mooney viscosity decreased. The morphology of nanocomposite was studied by XRD (X-ray diffraction) and TEM (Transmission electron microscope). Intercalation and exfoliation of the nanoclay were observed for samples with higher temperature and longer mixing time. Due to thermal degradation of the rubber matrix at 140°C, tensile properties of the nanocomposite were decreased.

Keywords: *nanocomposites, SBR, response surface methodology, tensile properties, Mooney viscosity*

1. Introduction

There is a large body literature which explains the enhancement of the properties by incorporation of nano filler into polymers. Depending on nano filler types (nanofibers: nanotubes and whiskers, nano particle: silicate layer, nano size isotropic: titanium dioxide) the obtained nanocomposites can offer [1–4]:

– better mechanical properties
– lower permeability against the gases
– higher heat deflection temperature
– higher flame retardancy.

To achieve all of aforesaid improvements, the presence of fully exfoliated or intercalated and well dispersed of nano fillers in polymer matrix is necessary.

In the melt intercalation method for producing of nanocomposite, the most important parameters which lead to gain this morphology are surface modification of nano filler by surfactants and proper processing conditions.

Many attempts have been focused on the description of the effects of processing parameters (in single and twin screw extruders and batch mixers) on the variation of nanocomposite morphology. Demirkol and Kalyon [5] studied different methods (batch and continuous) to produce nanocomposite. Their results point to the difficulty of the genera-

*Corresponding author, e-mail: I.ghasemi@ippi.ac.ir

tion of nanocomposites using melt compounding when the interfacial properties between the polymer melt binder and the organoclay are not favorable.

The effect of shear field on the morphology of nanocomposite has been reported by Homminga *et al*. [6]. They found the shear forces can facilitate the break-up of large-sized agglomerates, whereas the extent of further exfoliation of the mineral layers is determined by the compatibility between the polymer matrix and the mineral layers rather than shear forces.

Residence time and mixing efficiency as affective parameters in nanocomposite morpholology have been considered by many research groups. Borse and Kamal [7] reported that the larger residence time and higher mixing efficiency lead to higher degree of exfoliation and better mechanical properties of polyamide nanocomposites while Zhu and Xanthos [8] reported the residence time is a dominant factor in producing satisfactory polypropylene nanocomposite in extruder and that coupling of long residence time and high shear rate might result in poor exfoliation of nano filler.

Many attempts have been focused on the field of rubber/organo clay nanocomposites. The status and future trends [9], mechanical properties [10–12], rheology and thermodynamic [13] and effect of vulcanization ingredients [14] were studied.

In spite of many researches in the field of the extrusion of thermoplastic nanocomposites, there are only a few publications about affective parameters in batch mixer for producing rubber nanocomposite.

Other researchers [15] studied the effect of mixing on the properties of NR, SBR, BR and EPDM nanocomposites. Their results showed the mixing process plays a predominant role in formation nanometer scale dispersion structure. The effect of mixer type and mixing temperature on the properties of EPDM nanocomposite has been studied by Gatos and his coworkers [16]. It was found that increasing temperature and high shear mixing improve the mechanical performance of the rubber nanocomposite.

Using response surface methodology to optimize of process variables on flexural properties of epoxy/organoclay nanocomposites has been reported by Chow and Yap [17].

The purpose of the present work is to investigate the effect of mixing time and temperature in the internal mixer and nano filler amount on the properties of SBR nanocomposites. To analyze the results, response surface methodology were applied. The properties as response were scorch time, Mooney viscosity and the tensile properties (tensile strength, modulus, and elongation at break).

2. Experimental

2.1. Materials and sample preparation

Poliran SBR-1500 containing 23.5% of styrene was from Bandar Imam Petrochemical Co, Bandar Imam, Iran. The nanoclay was Cloisite 10A from Southern Clay, TX, USA with 1.92 nm initial gallery heights, modified with dimethyl benzyl hydrogenated tallow (2MBHT) quaternary ammonium, cation exchange capacity (CEC) was 110 mequiv/100 g. The activators (zinc oxide and Stearic Acid) and the curing agents (Sulfur and N-Cyclohexyl-2-benzothiazole sulfenamide (CBS)) purchased from local market. The formulation of nanocomposites was: SBR; 100 phr (per hundred rubber), nanoclay (variable 1, 3, 5 phr), Stearic acid; 1.5 phr, Zinc oxide; 5 phr, CBS; 1.5 phr, sulfur; 1.5 phr.

The compounding was carried out using HAAKE internal mixer (SYS 90, USA) with a Banbury blade. At first, SBR was fed into the mixing chamber, the nanoclay and CBS were then added into the chamber after 2 minutes and mixing continued until predetermined time (in internal mixer). The processing conditions of nanocomposites preparation (time and temperature of mixing) and nano amount were given in Table 1. The other curing ingredients were mixed on two-roll mill (Schwabenthan, model Polymix 200L) for 4 min at ambient temperature.

Table 1. The Box-Behnken experimental design

Sample No.	1	2	3	4	5	6	7	8	9	10	11	12	13	14	15
Mix temp. [°C]	80	140	80	140	80	140	80	140	110	110	110	110	110	110	110
Mix time [min]	4	4	12	12	8	8	8	8	4	12	4	12	8	8	8
Nano level [phr]	6	6	6	6	3	3	9	9	3	3	9	9	6	6	6

Vulcanization of the samples was carried out in a compression molding machine WCH202, Toyoseiki, Japan at 160°C for 15 minutes.

2.2. Measurements

Mooney viscosity ($ML(1+4)_{100}$) was investigated by 4309, ZWICK, Germany according to ASTM D1646 and rheometry test was made according to ASTM D2084 by 4308, ZWICK, Germany. The scorch time is the time to reach to 10% of maximum torque in the rheometry curing curve.

Tensile properties were measured according to ASTM D412 using Instron model 6025, UK. The cross head speed was 500 mm/min.

Wide-angle X-ray diffraction (XRD) measurements were carried out at room temperature on a D5000, Siemens, Germany. X-ray diffractometer with CuK_α = 1.541 nm with a generator voltage of 40 kV and a generator current of 100 mA. The scanning rate was 2°/min over a range of 20.

The morphology structure of the nanocomposites was investigated by an EM 208, Philips, Netherland transmission electron microscope (TEM) with an acceleration voltage of 100 kV. The ultrathin slides were obtained by an Ultracut UCT, Leica Germany at –55°C.

2.3. Experimental design

The Box-Behnken design was chosen as an experimental design for finding the exact quantitative relationship between properties of nanocomposite as the responses and different mixing conditions and content of nanoclay in the formulations. This design is rotatable which means that all the points in design area are at equal distance from the center points [18].

The number of design points (N) is calculated by Equation (1):

$$N = 2^k + 2k + m \quad (1)$$

where k and m are the number of factors and the number of replicates of the center points respectively. The replicate of center points is due to checking the reproducibility of the samples. The multiple linear regression analysis was used and the data were fitted as linear or second order equations. The order of equations are specified based on the lack of fit test and maximizing simultaneously three parameters viz. R^2 (the R^2 values indicate the degree of agreement between the experimental results with those predicted by model), adjusted R^2 and predicted R^2.

Table 2. Three levels Box-Behnken design

Variables	Low	Medium	High
Time [min]	4	8	12
Temperature [°C]	80	110	140
Nano level [phr]	3	6	9

A computer analysis has been done using commercially available package (MINITAB V13.2) to compute the equation constants.

In this study, the three variables in SBR nanocomposite at three levels Box-Behnken design was used which are shown in Table 2. According to this method 15 runs were necessary with three replicate of the center point. The design of experiment is shown in Table 2. A random sequence of experiments was implemented to minimize the sample preparation error.

Using response surface methodology with minimum number of experiments, it is possible to obtain quantitative equations for the effect of processing condition on the properties of SBR/organoclay nanocomposites. Application of this method has been reported in rubber field by Kukrejaa *et al*. [19].

3. Results and discussion

In Table 3 some statistical information and the equation of the model for each response are represented. The R^2 values for all responses are obtained in the range of 0.85–0.97. Although, R^2 closer to 1 means that the model is more valid but range achieved for R^2 in this study is an indication of a very good fitting of the experimental data by the response surface method in the models.

To interpret of the variation of the mechanical properties, it is useful to start by expressing the morphology of the nanocomposite. Figure 1 shows the XRD diffraction pattern of organoclay, SBR and samples No.4, 5 after curing. The diffraction peak of organoclay at $2\theta = 4.59°$ corresponds to 1.952 nm inter gallery distance (001). For sample No.5, it is obvious that after preparation of nanocomposites, diffraction peak of organoclay has been shifted to the lower 2θ (2.4 nm) value which means that the intercalation morphology is formed.

Table 3. Statistical data and the equation for different responses

Response	R^2	Adjusted R^2	Equation of the model
Scorch time [min]	0.967	0.924	2.3108 + 0.3488 (MTemp) + 0.0925 (MTime) – 0.8762 (NL) + 0.4887 $(MTemp)^2$ + 0.4087 $(NL)^2$ + 0.3900 (MTemp×MTime) + 0.2025 (MTemp×NL) – 0.1250 (MTime×NL)
Mooney viscosity (ML(1+4))	0.859	0.853	42.795 + 0.952 (MTemp) + 0.349 (MTime) + 1.489 (NL) – 2.515 $(NL)^2$ + 3.150 (MTemp×MTime) + 2.108 (MTemp×NL)
Tensile strength [MPa]	0.828	0.917	1.7893 + 0.0499 (MTemp) + 0.2135 (MTime) + 0.2704 (NL) – 0.0014 $(MTemp)^2$ + 0.0638 $(MTime)^2$ – 0.1154 (NL)2 + 0.2093 (MTemp×MTime) + 0.0710 (MTemp×NL) + 0.0692 (MTime×NL)
Elongation at break [%]	0.877	0.853	311.95 + 25.46 (MTemp) + 16.06 (MTime) + 29.69 (NL) + 31.07 $(MTemp)^2$ – 41.13 (MTime×MTemp)

mixing time: MTime, mixing temperature: MTemp, nanoclay level: NL

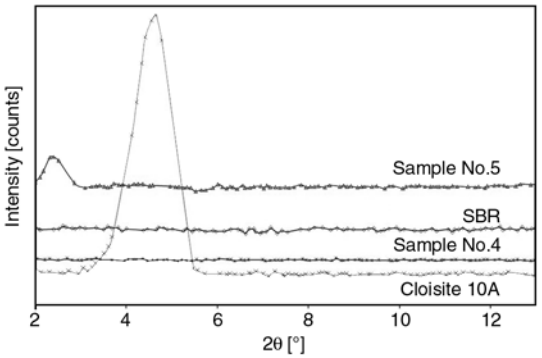

Figure 1. XRD diffraction patterns of organo clay, SBR and samples No.4 and No.5

The intensity of the X-ray patterns characterizing the degree of intercalation were changed with the mixing condition for samples with intercalation morphology. It seems that a good combination of time and temperature of mixing in sample No.4 (12 min, 140°C) could achieve a fully exfoliated morphology so that the peak of organoclay disappeared in XRD pattern. As discussed later the mechanical properties are affected by these morphologies. Similar XRD patterns have been reported for exfoliated and intercalated SBR/organoclay composites in literatures [20–22].

By TEM, one can obtain information on the real state of spatial distribution of the nano particles. Figure 2 shows the typical TEM micrograph from intercalation morphology which presents the dispersion state of the rubber-clay nanocomposites (sample No.5). The micrographs are given in low and high magnification. The dark lines represent the intersection of the nano silicate layers while the white background corresponds to rubber matrix. As can be seen, there is some stacking nano silicate layers with the thickness of about 10–20 nm.

The effects of mixing time and temperature on the tensile strength of SBR/organoclay composite at three levels of nanoclay are shown in Figure 3. As shown with increase of mixing time, the tensile strength increases. It seems the mixing time has the main role in the variation of tensile strength. The highest increment in this property is attributed to a combination of high temperature and long mixing time for the all ranges of nanoclay. This is because the aforesaid condition facilitates the nanoclay

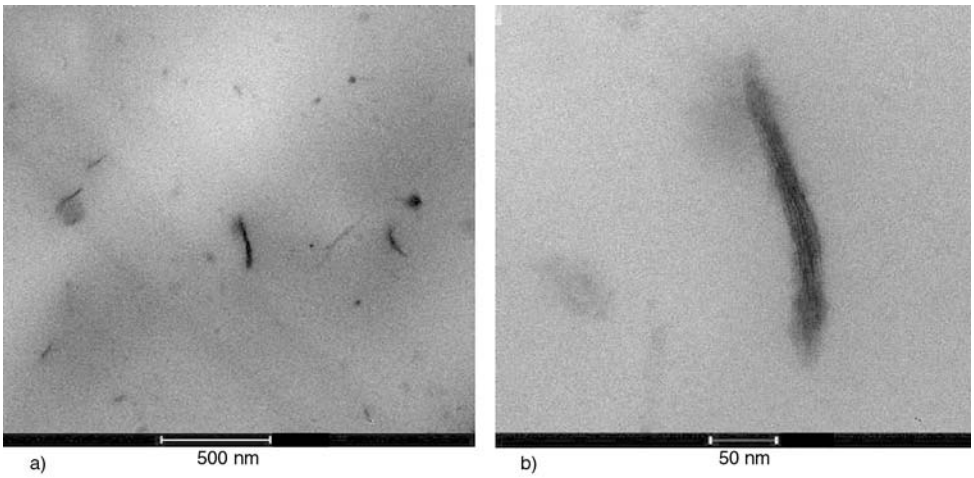

Figure 2. TEM micrographs of the sample No.5. a) low magnification, b) high magnification

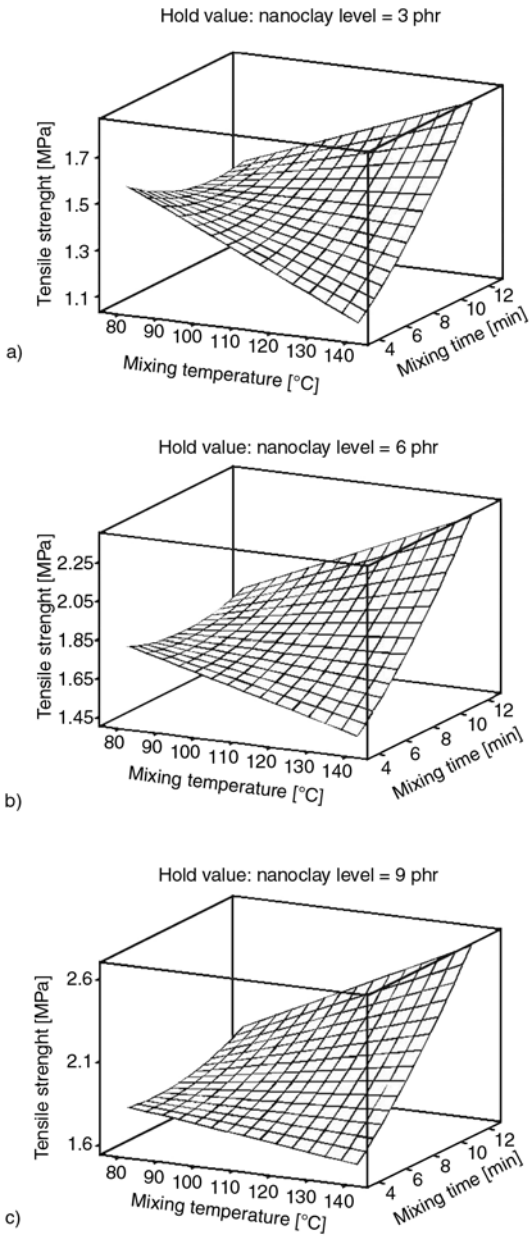

Figure 3. Tensile strenght versus mixing time and mixing temperature at different nanoclay contents: a) 3 phr, b) 6 phr, c) 9 phr

intercalation process. Vaia and Giannelis [23, 24] interpreted the intercalation process by thermodynamic approach. They believe that the intercalation process is influenced by enthalpy of the system which is affected by the rate of diffusion of polymeric chain into the gallery of nanoclay. If the diffusion process of chains obey the Arrhenius equation [$D = D_0 \exp(-\Delta E/RT)$], the diffusivity of polymer into the nano layers will increase with temperature, where D is the diffusion coefficient, D_0 is the pre-exponential factor of the diffusion process independent from the temperature, ΔE is the activation energy, T is the absolute temperature and R is the gas constant. In other words with the increase of temperature the mobility of rubber chains and consequently the rate of diffusion increases and so facilitates the intercalation process.

Another important point in Figure 3 is that at constant mixing time with increase of temperature, tensile strength decreases especially at 3 phr of nanoclay concentration. It can be explained as follows: the tensile strength is balanced by two opposite effects, the positive effect is the interaction between rubber chains and nanoclay and the negative effect is the rubber degradation during mixing at high temperature. It should be considered that at longer mixing time (above 8 minutes), the positive effect of intercalation on the tensile strength is stronger than that of thermal degradation. This phenomenon can also be seen in sample containing 9 phr of nanoclay where the slope of decreasing of tensile strength versus temperature (Figure 3c) is lower than those of other samples.

Elongation at break values versus time and temperature of mixing at three levels of nanoclays are demonstrated in Figure 4. As expected, the elongation at break is affected by temperature, mixing time and nanofiller content. It is well known that the elongation at break of rubber nanocomposite depends on the morphology of nanocomposites. Due to slippage of rubber chains in the presence of the free surfactant of nanoclay in exfoliated or intercalated morphology, the elongation at break increases [25–29]. In other words, the surfactant can act as a lubricant in the nanocomposites. In addition, the orientation of silica layers under tensile stress is another reason for increasing of elongation at break. The highest value for this property was related to sample No.8 which the conditions were 8 min, 140°C and 9 phr of nanoclay. This trend indicates the longer mixing time at highest temperature led to the thermal degradation of SBR and consequently the elongation at break decreases.

Mixing time and temperature dependency of scorch time is demonstrated in Figure 5 at three levels of nanoclay content. It is clear, with increase of nanoclay content in nanocomposite, the scorch time decreases. This can be attributed to presence of organic group of surfactant in nanaoclay. The formation of Zn-complex in the presence of sulfur and ammonium group of the surfactant has been reported for butadiene rubber with the sulfur/sulfonamide vulcanization systems by researchers

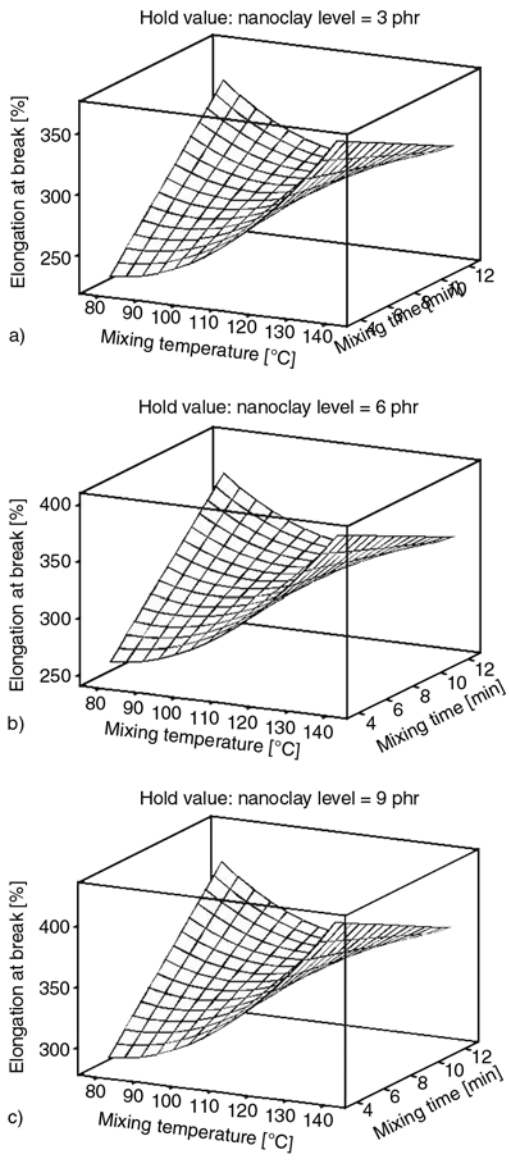

Figure 4. Elongation at break versus mixing time and mixing temperature at different nanoclay contents: a) 3 phr, b) 6 phr, c) 9 phr

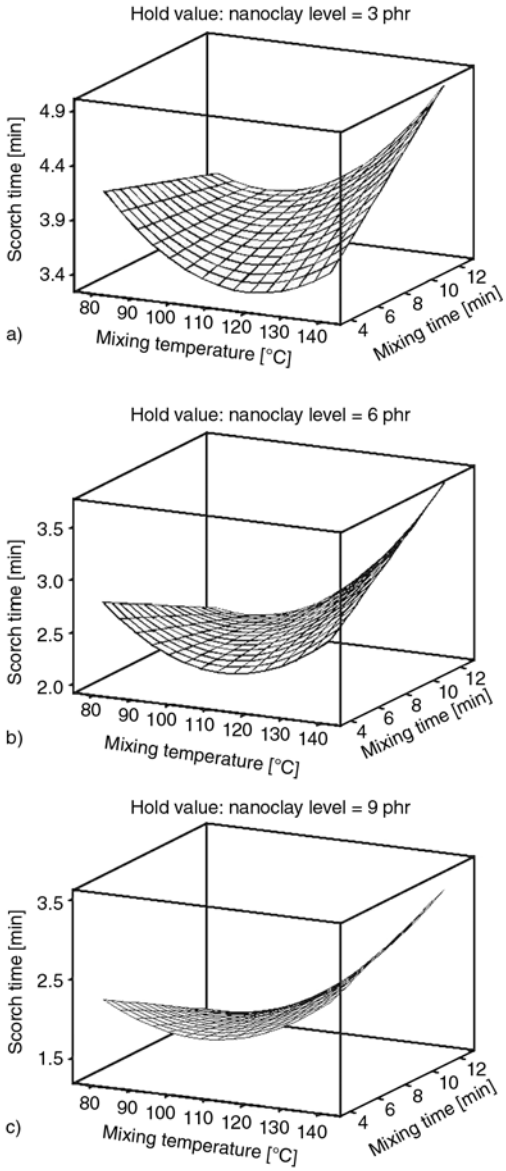

Figure 5. The variation of scorch time versus time and temperature of mixing at different nanoclay contents: a) 3 phr, b) 6 phr, c) 9 phr

[12]. They reported that the obtained chelate is more active than sulfenamid accelerators and it facilitates crosslinking reaction which leads to shorter scorch time. Similar results have been reported for scorch time of crosslinking of NR, SBR and ENR and it was found that the longer chain length of surfactant can also shorten the scorch time [11, 30–32]. As can be seen, the variation of scorch time versus temperature passes through a minimum of around 120°C for all samples. It seems, since at high temperature of mixing, the exfoliated morphology can be attained, ammonium groups are more available and so the possibility of formation of Zn-complex is higher and crosslinking reaction leads to a shorter scorch time. After minimum point (120°C) in this curve, the scorch time is affected by degradation of rubber chains especially at longer mixing time. In other words, during mixing, the chemical structure of rubber is changed by thermal degradation, and the rate of crosslinking reaction is somewhat affected by this phenomenon and the scorch time increases.

The variation of Mooney viscosity versus mixing time and nano content at three levels of mixing temperature is shown in Figure 6. As can be seen at lower temperature (Figure 6a) Mooney viscosity

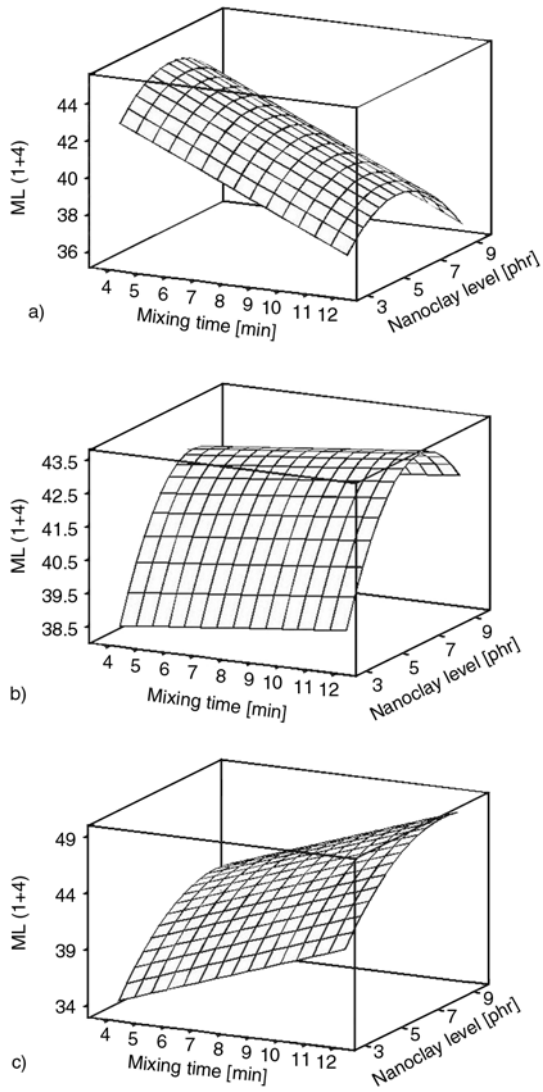

Figure 6. Mooney viscosity against mixing time and nano content at three levels of mixing temperatures: a) 80°C, b) 110°C, c) 140°C

decreases with increasing mixing time. Generally, viscosity of rubber nanocomposites may be affected by lubricating effect of pendant chains of surfactant in intercalation or exfoliation morphologies. At lower temperature and longer mixing time the viscosity decreases. Under these conditions, the good dispersion of nano particles can be attained and the organic surfactant cause the slippage of rubber chains. This behavior may be also attributed to the orientation of silicate platelets upon shearing in Mooney viscosity test [33].

With increasing of temperature (Figure 6b and 6c), the trend of Mooney viscosity variation changes and passes through minimum. The slope of increment at 140°C is higher than at 110°C. This is because the CBS accelerator can be activated at high temperature and partial crosslinking may occur in nanocomposites which was confirmed by extraction test before crosslinking. The undissolved part of this test implies partial crosslinking in the samples. The presence of rubber crosslink bonds in the compound is the main reason of increased viscosity which can overcome the effect of chain slippage and nanoclay orientations.

4. Conclusions

This study, aimed at investigating the effect of processing conditions (temperature and mixing time) and nano filler content on mechanical performance and structure of SBR/organoclay (MMT) composites using response surface methodology, the following conclusion can be drawn:

1. Mathematical models and response surface graphs are obtained to illustrate the relationship between mixing parameters in internal mixer and properties of the SBR/organoclay composites. It is obvious that this prediction suggests only a first approximation for other polymer grades and other equipments.
2. Increasing temperature and mixing time contribute to a better organoclay dispersion which results in improved mechanical properties.
3. Thermal degradation of the matrix occurred at high temperature (140°C) of mixing and mechanical properties were affected by this phenomenon.
4. Intercalation and exfoliation of the clay were noticed for samples containing higher temperature and longer mixing time.
5. With increase of nanoclay content in composite the scorch time decreases.

Based on the present work by using the response surface methodology with minimum number of experiment, it is possible to obtain quantitative equation for properties of SBR/organoclay composite vs. different processing variables and nano filler content. With this equation one can optimize the nano filler content and the processing parameters for producing the nanocomposite with optimum properties.

References

[1] Tjong S. C.: Structural and mechanical properties of polymer nanocomposites. Materials Science and Engineering Report, **73**, 53–64 (2006).
DOI: 10.1016/j.mser.2006.06.001

[2] Pegoretti A., Dorigato A., Penati A.: Tensile mechanical response of polyethylene-clay nanocomposites. Express Polymer Letters, **1**, 123–132 (2007).
DOI: 10.3144/expresspolymlett.2007.21

[3] Arroyo M., López-Manchado M. A., Valentín J. L. Carretero J.: Morphology/behaviour relationship of nanocomposites based on natural rubber/epoxidized natural rubber blends. Composites Science and Technology, **67**, 1330–1347 (2007).
DOI: 10.1016/j.compscitech.2006.09.019

[4] Hussain F., Hojjati M., Okamoto M., Gorga R. E.: Review article: Polymer-matrix nanocomposites, processing, manufacturing, and application: An overview. Journal of Composite Material, **17**, 40–53 (2006).
DOI: 10.1177/0021998306067321

[5] Demirkol E. A., Kalyon D. M.: Batch and continuous processing of polymer layered organoclay nanocomposites. Journal of Applied Polymer Science, **104**, 1391–1402 (2007).
DOI: 10.1002/app.24362

[6] Homminga D., Goderis B., Hoffman H., Reynaers H., Groeninckx G.: Influence of shear flow on the preparation of polymer layered silicate nanocomposites. Polymer, **46**, 9941–9957 (2005).
DOI: 10.1016/j.polymer.2005.07.059

[7] Borse K. N., Kamal M. R.: Melt processing effects on the structure and mechanical properties of PA-6/clay nanocomposites. Polymer Engineering and Science, **46**, 1094–1108 (2006).
DOI: 10.1002/pen.20578

[8] Zhu L., Xanthos M.: Effects of process conditions and mixing protocols on structure of extruded polypropylene nanocomposites. Journal of Applied Polymer Science, **93**, 1891–1899 (2004).
DOI: 10.1002/app.20658

[9] Karger-Kocsis J., Wu C-M.: Thermoset rubber/layered silicate nanocomposites. Status and future trends. Polymer Engineering and Science, **44**, 1083–1093 (2004).
DOI: 10.1002/pen.20101

[10] Sengupta R., Chakraborty S., Bandyopadhyay S., Dasgupta S., Mukhopadhyay R., Auddy K., Deuri A. S.: A short review on rubber/clay nanocomposites with emphasis on mechanical properties. Polymer Engineering and Science, **47**, 1956–1974 (2005).
DOI: 10.1002/pen.20921

[11] Varghese S., Karger-Kocsis J., Gatos K. G.: Melt compounded epoxidized natural rubber/layered silicate nanocomposites: Structure-properties relationships. Polymer, **44**, 3977–3983 (2003).
DOI: 10.1016/S0032-3861(03)00358-6

[12] Varghese S., Karger-Kocsis J.: Melt-compounded natural rubber nanocomposites with pristine and organophilic layered silicates of natural and synthetic origin. Journal of Applied Polymer Science, **91**, 813–819 (2004).
DOI: 10.1002/app.13173

[13] Mousa A., Karger-Kocsis J.: Rheological and thermodynamical behavior of styrene/butadiene rubber-organoclay nanocomposite. Macromolecular Materials and Engineering, **286**, 260–266 (2004).
DOI: 10.1002/1439-2054(20010401)286:4<260::AID-MAME260>3.0.CO;2-X

[14] Das A., Jurk R., Stöckelhuber K. W., Heinrich G.: Effect of vulcanization ingredients on the intercalation-exfoliation process of layered silicate in an acrylonitrile butadiene rubber matrix. Macromolecular Materials and Engineering, **293**, 479–490 (2004).
DOI: 10.1002/mame.200700375

[15] Wu Y-P., Ma Y., Wang Y-Q., Zhong L-Q.: Effects of characteristics of rubber, mixing and vulcanization on the structure and properties of rubber/clay nanocomposites by melt blending. Macromolecular Materials and Engineering, **28**, 890–894 (2004).
DOI: 10.1002/mame.200400085

[16] Gatos K. G., Thomann R., Karger-Kocsis J.: Characteristics of ethylene propylene diene monomer rubber/organoclay nanocomposites resulting from different processing conditions and formulations. Polymer International, **53**, 1191–1197 (2004).
DOI: 10.1002/pi.1556

[17] Chow W. S., Yap Y. P.: Optimization of process variables on flexural properties of epoxy/organo-montmorillonite nanocomposite by response surface methodology. Express Polymer Letters, **2**, 2–11 (2008).
DOI: 10.3144/expresspolymlett.2008.2

[18] Montgomery D. C. M.: Design and analysis of experiments. Wiley, New York (2001).

[19] Kukrejaa T. R., Kumar D., Prasad K., Chauhan R. C., Choe S., Kundu P. P.: Optimisation of physical and mechanical properties of rubber compounds by response surface methodology – Two component modelling using vegetable oil and carbon black. European Polymer Journal, **38**, 1417–1422 (2002).
DOI: 10.1016/S0014-3057(02)00005-8

[20] Song M., Wong C. W., Jin J., Ansarifar A., Zhang Z. Y., Richardson M.: Preparation and characterization of poly (styrene-*co*-butadiene) and polybutadiene rubber/clay nanocomposites. Polymer International, **54**, 560–568 (2005).
DOI: 10.1002/pi.1732

[21] Jia Q-X., Wu Y-P., Wang Y-Q., Lu M., Zhang L-Q.: Enhanced interfacial interaction of rubber/clay nanocomposites a novel two-step method. Composites Science and Technology, **68**, 1050–1056 (2008).
DOI: 10.1016/j.compscitech.2007.07.006

[22] Sadhu S., Bhowmick A. K.: Preparation and properties of styrene-butadiene rubber based nanocomposites: The influence of the structural and processing parameters. Journal of Applied Polymer Science, **92**, 698–709 (2004).
DOI: 10.1002/app.13673

[23] Vaia R. A., Giannelis E. P.: Lattice model of polymer melt intercalation in organically-modified layered silicates. Macromolecules, **30**, 7990–7999 (1997).
DOI: 10.1021/ma9514333

[24] Vaia R. A., Giannelis E. P.: Polymer melt intercalation in organically-modified layered silicates: Model predictions and experiment. Macromolecules, **30**, 8000–8009 (1997).
DOI: 10.1021/ma9603488

[25] Sadhu S., Bhomick A. K.: Morphology study of rubber based nanocomposites by transmission electron microscopy and atomic force microscopy. Journal of Materials Science, **40**, 1633–1642 (2005).
DOI: 10.1007/s10853-005-0663-2

[26] Lee S-I., Hahn Y. B., Nahm K. S., Lee Y-S.: Synthesis of polyether-based polyurethane-silica nanocomposites with high elongation property. Polymers for Advanced Technologies, **16**, 328–331 (2005).
DOI: 10.1002/pat.548

[27] Pramanik M., Srivastava S. K., Samantaray B. K., Bhowmick A. K.: Synthesis and characterization of organosoluble thermoplastic elastomer/clay nanocomposites. Journal of Polymer Science Part B: Polymer Physics, **40**, 2065–2072 (2002).
DOI: 10.1002/polb.10266

[28] López-Manchado M. A., Herrero B., Arroyo M.: Preparation and characterization of organoclay nanocomposites based on natural rubber. Polymer International, **52**, 1070–1077 (2003).
DOI: 10.1002/pi.1161

[29] Finnigan B., Martin D., Halley P., Truss R., Campbell K.: Morphology and properties of thermoplastic polyurethane composites incorporating hydrophobic layered silicates. Journal of Applied Polymer Science, **97**, 300–309 (2005).
DOI: 10.1002/app.21718

[30] Wang S., Peng Z., Zhang Y., Zhang Y.: Structure and properties of BR nanocomposites reinforced with organoclay. Polymer and Polymer Composites, **13**, 371–384 (2005).

[31] Arroyo M., López-Manchado M. A., Herrero B.: Organo-monmorillonite as substitute of carbon black in natural rubber compounds. Polymer, **44**, 2447–2453 (2003).
DOI: 10.1016/S0032-3861(03)00090-9

[32] Cataldo F.: Preparation and properties of nanostructured rubber composites with montmorillonite. Macromolecular Symposia, **247**, 67–77 (2007).
DOI: 10.1002/masy.200750109

[33] Teh P. L., Mohd Ishak Z. A., Hashim A. S., Karger-Kocsis J., Ishiaku U. S.: On the potential of organoclay with respect to conventional fillers (carbon black, silica) for epoxidized natural rubber compatibilized natural rubber vulcanizates. Journal of Applied Polymer Science, **94**, 2438–2445 (2004).
DOI: 10.1002/app.21188

eXPRESS Polymer Letters Vol.4, No.2 (2010) 71–78
Available online at www.expresspolymlett.com
DOI: 10.3144/expresspolymlett.2010.12

Particle size tuning in silver-polyacrylonitrile nanocomposites

A. Tyurin[1], *G. De Filpo*[2*], *D. Cupelli*[3], *F. P. Nicoletta*[3], *A. Mashin*[1], *G. Chidichimo*[2]

[1]Department of Applied Physics & Microelectronics, Lobachevsky State University, 603022 Nizhni Novgorod, Russia
[2]Department of Chemistry, University of Calabria, 87036 Rende (CS), Italy
[3]Department of Pharmaceutical Sciences, University of Calabria, 87036 Rende (CS), Italy

Received 2 September 2009; accepted in revised form 7 November 2009

Abstract. Silver-polyacrylonitrile (Ag-PAN) nanocomposites were *in situ* synthesized by simultaneous polymerization of acrylonitrile and reduction of silver ions, starting from mixtures of silver nitrate ($AgNO_3$), acrylonitrile (AN), and UV photoinitiator (IN). The films obtained proved to be transparent and were characterized by a homogeneous dispersion of Ag nanoparticles within the PAN matrix without any macroscopic agglomeration. The particle size and number density were found to depend on both precursor salt and UV photoinitiator weight percentages. Optical and electrical properties were investigated as a function of both $AgNO_3$ and IN amounts, too. We found that it is possible to finely tailor the metal nanoparticle size and number density and, consequently, the film optical and electrical response by adjusting the amounts of precursor salt and UV photoinitiator in the initial mixtures.

Keywords: *nanocomposites, nanomaterials, electrical properties, optical properties*

1. Introduction

Noble metal nanoparticles dispersed in insulating matrices have attracted the interest of many researchers from both applied and theoretical points of view [1–8]. In facts, such nanocomposites exhibit specific optical and electrical properties, making them suitable as advanced technological materials to be used as novel sensors, in catalytic applications, for energy storage, etc. [9–11].

Polymers represent suitable matrices for the preparation of metal nanocomposites being generally low cost materials characterized by an easy processing. For practical applications it is important to get nanoparticles uniformly dispersed in polymer matrices, but, due to their high surface reactivity, metal nanoparticles tend to aggregate into larger dimension clusters. Composites made by mechanical mixing of metal nanoparticles and molten polymers generally lead to inhomogeneous particle dispersions. As a consequence, various approaches have been proposed to manufacture metal nanocomposites including ball milling, coevaporation and sputtering of metals and polymers, plasma polymerization, and new synthetic procedures [12–15]. Among these last approaches, it is important to mention the use of different agents in order to increase nanoparticle stability, the simultaneous photoinduced electron transfer and cationic polymerization, the thermal and UV *in situ* polymerizations [16–22]. Recently, UV *in situ* polymerization has gained a lot of attention. In fact, UV photochemically assisted polymerizations are characterized by low temperature conditions and faster polymerization rates, resulting in the formation, during the polymer network growth, of homogeneously dispersed metal nanoparticles without the use of further solvents and reducing agents. The UV photochemically generated radicals, being electron

*Corresponding author, e-mail: defilpo@unical.it

donor species, are able to simultaneously polymerize monomers and reduce the metal salts, which will form metal nanoparticles.

Acrylonitrile is an important polymer used principally in the manufacture of synthetic fibers. Silver is a well known metal characterized by a high electrical conductivity, good optical properties, and interesting oxidative catalysis performance.

In this paper we have investigated the *in situ* synthesis of silver-poliacrylonitrile (Ag-PAN) nanocomposites by a UV photoinduced process. 2,2′dimethoxy-2-phenil acetophenone was used as UV photoinitiator (IN) to generate electron donating radicals. Subsequent oxidation of these radicals to corresponding cations in the presence of silver nitrate ($AgNO_3$) and acrylonitrile (AN) leads to the simultaneous formation of silver (Ag) nanoparticles and polymerization of polyacrylonitrile (PAN). Nanocomposite morphology, electrical and optical properties were found to depend both on $AgNO_3$ and IN amounts in the starting mixtures, allowing a fine tailoring of both size and number density of metal particles and, consequently, the properties of Polymer Dispersed Metal NanoParticles (PDMNPs).

2. Experimental part

Acrylonitrile monomer and silver nitrate were both supplied by Aldrich, Milan, Italy. 2,2′dimethoxy-2-phenyl acetophenone (Aldrich, Milan, Italy) was used as UV photoinitiator. AN/$AgNO_3$/IN mixtures were prepared in vials by mixing the appropriate wt. amounts of components. $AgNO_3$ was varied in the range from 2 to 25 wt%, while IN was varied from 0 to 25 wt%. Then, a small quantity of mixtures was introduced by capillary action into home made cells, whose thickness was set to be 25 μm by glass spheres. Glass substrates had a 120 nm indium tin oxide conductive layer for the successive electric characterization. After filling, cells were exposed at room temperature (20°C) for 10 min to the UV light from a high pressure lamp (HPK 125, Philips, Eindhoven, Nederlands, average power 110 μW/cm^2) in order to generate free radicals in the samples and to cause the simultaneous polymerization of AN in PAN and reduction of Ag^+ ions in metal silver. Film samples were characterized by X-ray using a 1730/10 diffractometer (Philips, Eindhoven, Nederlands) using CuK_α radiation and 0.5° 2θ min^{-1}. FT-IR measurements were carried out by a Fourier Transform Infrared spectrometer (FT-IR Jasco 4200, Jasco Europe, Cremella, Italy) in the spectral range 4000–400 cm^{-1}. The morphology of ultra-thin sections (80 nm) of silver particles in PAN was investigated by a transmission electron microscope (TEM, Zeiss EM 900, Carl Zeiss S.p.A., Milan, Italy). Conductivity measurements were carried in the frequency range from 20 Hz to 1 MHz with a LCR meter (Agilent 4284A, Agilent Technologies Italia S.p.A., Cernusco sul Naviglio, Italy). The applied voltage over the entire frequency range was 1 V, which is the typical voltage used in other similar measurements [23]. The composite conductivity was calculated from geometrical factors. The film absorption spectra were determined by a UV-Vis spectrometer (Jasco 550V, Jasco Europe, Cremella, Italy) in the wavelength range of 300–800 nm.

3. Results and discussion

It is known that the electrical and optical properties of metal nanoparticles-polymer composites strongly depend on particle morphology. In order to understand the main idea followed in this work, we recall the three reactions that can occur during the irradiation of silver nitrate, acrylonitrile and photoinitiator mixtures. Hong *et al.* have shown that silver ions and AN form the following complex when mixed [24]:

$$Ag^+ + 2\ AN \leftrightarrows [Ag(AN)_2]^+$$

If the solution is irradiated by ultraviolet light, the photoinitiator will induce the free radical polymerization of AN monomers, and, simultaneously, Ag^+ is reduced to metallic silver according to the reaction scheme 1 reported in Figure 1.

The presence of photoinitiator allows the further reactions reported in the reaction schemes 2 and 3 of Figure 1.

Reaction scheme 1 describes the simultaneous reduction of silver ions and the cationic polymerization of AN, while reaction scheme 2 shows the UV free radical polymerization of AN. Reaction scheme 3 is equivalent to reaction scheme 1 (in this case the cationic polymerization of AN is mediated by IN), and both are responsible for nanoparticle nucleation (and growth) and AN polymerization. Reaction scheme 2, acting only on polymer growth,

Reaction scheme 1

$[Ag(AN)_2]^+ + NO_3^- \xrightarrow{h\nu} Ag^0 + \frac{1}{2}O_2 + NO_2 + -(AN-)_n-$ (polymer growth and nanoparticle nucleation)

$n\,Ag^0 \longrightarrow (Ag)_n$ (nanoparticle growth)

Reaction scheme 2

$IN + h\nu \longrightarrow IN^*$ (initator activation)

$AN + IN^* \longrightarrow AN^*-IN$ (radical monomer formation)

$(AN)_n + AN^*-IN \longrightarrow (AN)_n - AN^*-IN$ (polymer growth)

Reaction scheme 3

$IN + Ag^+ + h\nu \longrightarrow IN^+ + Ag$ (nanoparticle nucleation and growth)

$AN + IN^+ \longrightarrow AN^+ + IN$

$(AN)_n + AN^+ \longrightarrow (AN)_n - AN^+$ (polymer growth)

Figure 1. Reaction schemes for mixtures of AN, $AgNO_3$ and IN

could allow one to control film morphology by a simple change in photoinitiator loading. As a consequence, we have investigated the morphology, the electrical and optical properties of PDMNP composites as a function of both silver nitrate and photoinitiator wt. percentages.

3.1. Morphology analysis of PDMNPs

Figure 2 shows the typical X-ray diffraction spectra of an Ag/PAN nanocomposite film ([$AgNO_3$] = 15 wt% and [IN] = 10 wt%). The broad peak centered at 2θ = 21° can be associated with the amorphous phase of pure PAN, while the sharp peak at 16° corresponds to the orthorhombic PAN reflection (100) . The other peaks (2θ = 38°, 2θ = 44°, and 2θ = 65°) correspond to the (111), (200) and (220) crystalline planes of face centered cubic silver, which are consistent with standard values and confirm the Ag reduction and growth.

Figure 3 shows the FT-IR spectra of pure AN and Ag/PAN nanocomposite film ([$AgNO_3$] = 15 wt%

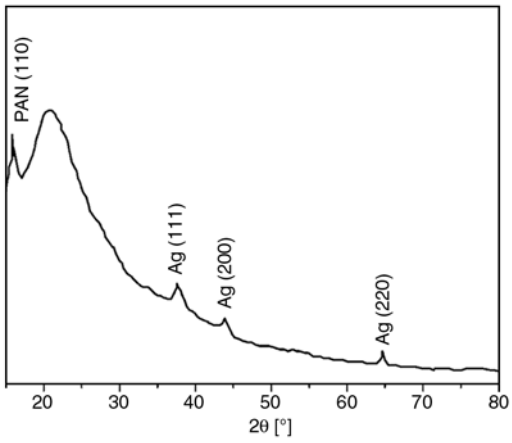

Figure 2. X-ray diffraction spectra of Ag/PAN nanocomposite ([IN] = 10 wt% and [$AgNO_3$] = 15 wt%)

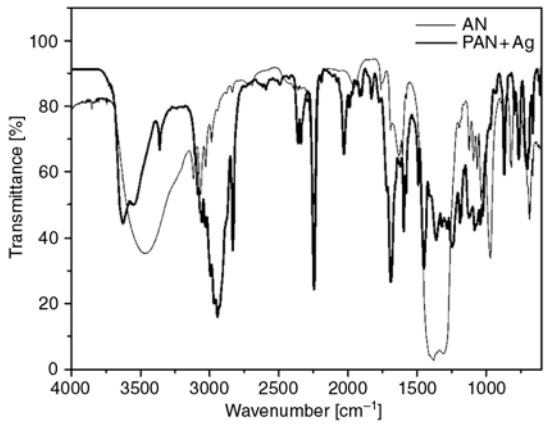

Figure 3. FT-IR spectra of pure AN and Ag/PAN nanocomposite ([IN] = 10 wt% and [$AgNO_3$] = 15 wt%)

and [IN] = 10 wt%). By comparing the absorption bands it is evident the polymerization of AN from the disappeareance of the absorption band at 967 cm^{-1} (C=C bond) and the appeareance of an absorption band in the range 3000–2900 cm^{-1} (aliphatic CH).

TEM pictures allow a quantitative morphology analysis of Ag/PAN nanocomposite films. Let's recall first the behaviour of nanoparticle size, *d*, and number density, *ND*, when the silver nitrate amount is increased at constant photoinitiator loading. As we found (data not shown) in agreement with the pictures reported in references 18 and 22, when the synthesis of Ag/PAN nanocomposites is achieved by a simultaneous polymerization and reduction approach, silver nanoparticles are well dispersed, their size distribution is uniform with spherical shape, and no agglomeration is evident. In addition, the diameter of Ag grains increases, while their number density decreases as silver nitrate wt. concentration increases in the sample compositions at constant photoinitiator amount. On the contrary, if

the [$AgNO_3$] is kept constant and [IN] is increased, we observed large average particle sizes at lower IN wt. concentration and smaller average particle sizes for increasing IN wt. concentration. Figure 4 shows the typical TEM pictures of Ag/PAN nanocomposites as a function of initiator wt. percentage at constant metal precursor percentage ([$AgNO_3$] = 15 wt%). In particular, at lower lower IN wt. concentration ([IN] = 2 wt%) the silver particle size is around 11 nm and decreases to the value of 1–2 nm for larger IN amounts ([IN] = 20 and 25 wt%). The increase of $AgNO_3$ loading to values larger than 25 wt% causes the appereance of some silver aggregates dispersed in the PAN matrices.

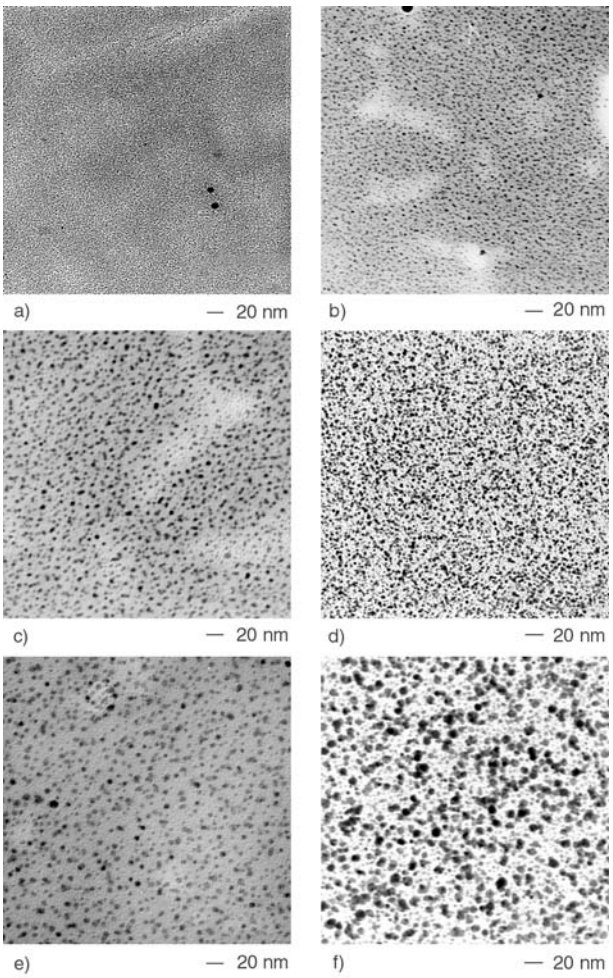

Figure 4. TEM pictures of Ag/PAN nanocomposite films at a constant silver nitrate wt. percentage, ([AgNO3] = 15 wt%): a) [IN] = 25 wt%, b) [IN] = 20 wt%, c) [IN] = 15 wt%, d) [IN] = 10 wt%, e) [IN] = 5 wt%, f) [IN] = 2 wt%. Silver nanoparticles are well dispersed and no agglomeration is evident. Metal nanoparticles possess almost uniform size distribution with spherical shape.

Results are more evident in Figures 5 and 6, where the average size and number density of Ag particles as a function of IN wt. percentage at constant metal precursor percentage ([$AgNO_3$] = 15 wt%) are plotted.

The observed Ag particle sizes are characterized by a very narrow size distribution as PAN plays the role of protective agent against nanoparticle diffusion and agglomeration. As IN concentration increases the particle diameter decreases, but, at the same time, their number density increases. Such results are in agreement with expectations as the increase of inititiator concentration results in a faster polymerization of AN and, consequently, in a faster increase of sample viscosity and decrease of silver diffusion leading to a larger number of small size metal particles. In addition, it is expected that the reaction scheme 2 in Figure 1 should depress the first line of reaction scheme 1 if one increases

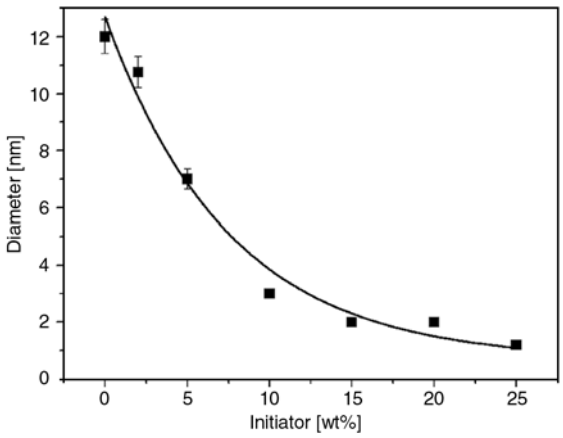

Figure 5. Average size of Ag particles as a function of initiator wt. percentage at constant metal precursor percentage ([$AgNO_3$] = 15 wt%)

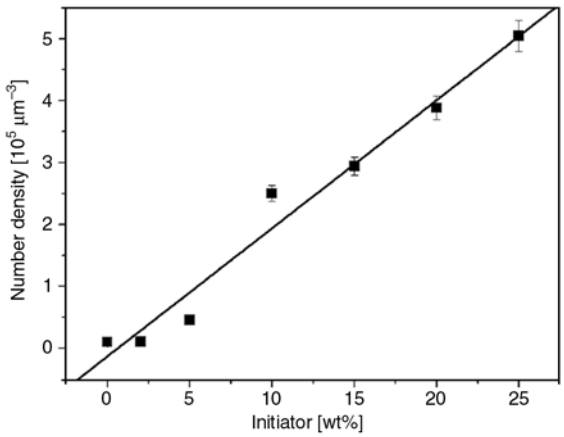

Figure 6. Average number density of Ag particles as a function of initiator wt. percentage at constant metal precursor percentage ([$AgNO_3$] = 15 wt%)

[IN], as the photon number is reduced by the reaction reported in line 3 of scheme 2.

The calculation of metal silver volume fraction (or filling factor, *FF*) in our samples was performed by using the simple Equation (1):

$$FF = \frac{V_{Ag}}{V_{tot}} = \frac{4}{3}\pi R^3 ND \quad (1)$$

where V_{Ag} and V_{tot} are the volumes of Ag nanoparticles and observed sample, respectively. The behaviour of *FF* vs. [IN] is reported in Figure 7 and is in agreement with expectations. So, both metal precursor and photoinitiator concentrations can control particle size and number density. For the sake of completeness, we must stress that temperature can affect particle morphology, acting on the reaction rate constants and translational diffusion coefficients. Work is in progress in order to investigate the influence of temperature on morphology.

The presence of an UV photoinitiator in our mixtures is important. In fact, in the absence of photoinitiator and low wt. percentage of silver nitrate (less than 15 wt%) the polymerization of acrylonitrile does not occur within reasonable irradiation times (1 hour). In addition, films turn coloured for larger percentages of $AgNO_3$ as shown in Figure 8. Unwanted crystallization of un-reacted silver nitrate can occur as the salt solubility in PAN is lower than that in AN, leading to a dramatic increase of light scattering.

The simultaneous in situ AN polymerization and Ag^+ reduction allows the formation of well monodispersed nanoparticles. We must recall that silver nitrate is well dispersed in acrylonitrile at room temperature without the use any other solvent.

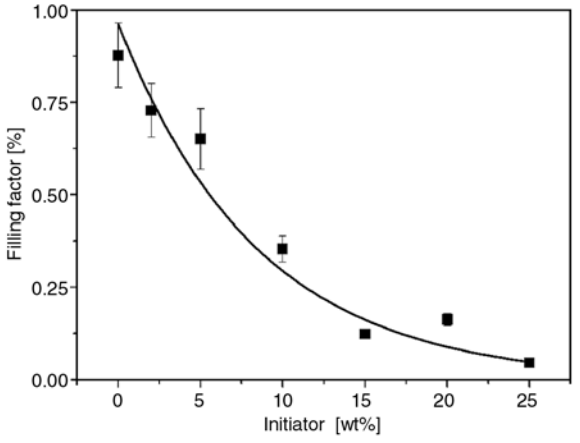

Figure 7. Photoinitiator dependent filling factor behaviour at constant metal precursor percentage ([$AgNO_3$] = 15 wt%)

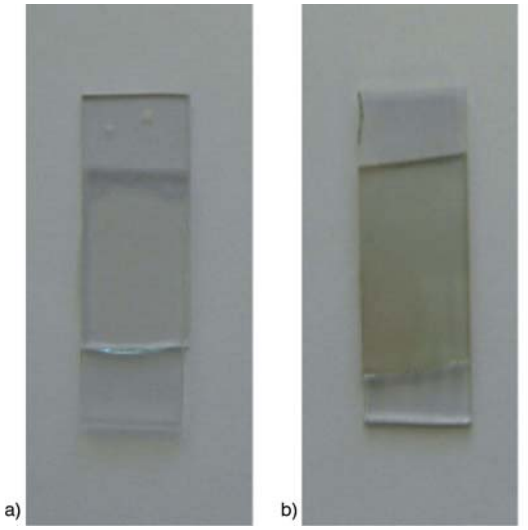

Figure 8. Pictures of samples with: a) [$AgNO_3$] = 20 wt% and b) [$AgNO_3$] = 30 wt%. The initiator amount is 10 wt% in both samples.

3.2. Electrical properties of PDMNPs

The electrical properties of polymer dispersed metal nanoparticles are strongly influenced by the metal filling factor and nanoparticle sizes [6, 7].

The main electric conductivity mechanisms in PDMNPs are:

1. Ion conductivity, due to the ions remaining dispersed in the polymer matrix;
2. Electron conductivity in the metal nanoparticle network;
3. Tunnelling conductivity.

Generally, at high volume fractions of metal nanoparticles a 3D conducting network can develop in the matrix, leading to a sudden increase in the electric conductivity known as percolation. Our samples are characterized by rather low filling factors as shown in Figure 7, always far from percolation threshold. By comparing the conductivities of a sample containing 15 wt% of $AgNO_3$ and 0 wt% of IN in its fluid (un-polymerized, $\sigma = 0.45\ \mu S \cdot cm^{-1}$) and solid (polymerized, $\sigma = 7.2\ \mu S \cdot cm^{-1}$) state, we observed that the conductivity of the fluid solution is almost two order of magnitude lower than the solid one. By taking into account that in the fluid solution:

1. there is no metal particle,
2. the electric conduction is ionic,

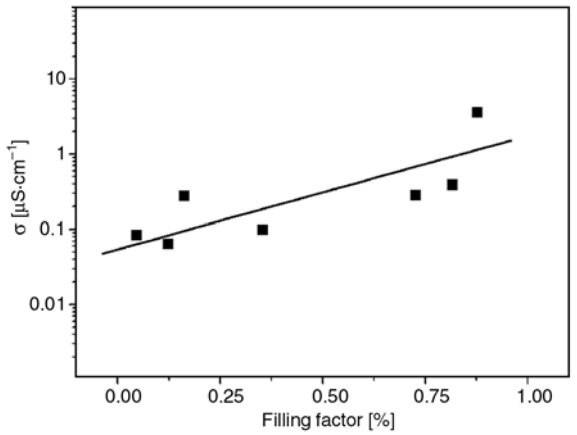

Figure 9. Conductivity behaviour of PDMNPs as a function of frequency for different initiator wt. percentage at constant metal precursor percentage ([$AgNO_3$] = 15 wt%)

3. ion mobility is larger than in the solid matrices

we can state that at low frequencies the conduction in our polymerized samples is due to an electron transport through metal nanoparticles and the ionic conductivity is negligible.

Figure 9 shows the frequency dependent behaviour of film conductivity for different IN contents at a constant silver nitrate percentage ([$AgNO_3$] = 15 wt%). Conductivities monotonically increase as a function of frequency and show larger values for larger IN amounts, i.e. in samples which are characterized by smaller nanoparticles.

If we report the behaviour of electric conductivity as a function of filling factor as previously calculated, we obtain the graph reported in Figure 10, where the conductivity increase for increasing values of filling factor, in agreement with the effective medium theoretical models [3, 6, 25]. Therefore, it is possible to gain the wanted film conductivity by changing both the photoinitiator and metal salt amounts in the starting mixtures.

3.3. Optical properties of PDMNPs

Metal nanocomposites generally exhibit particular optical properties originating from the strong interactions between incident light and metal nanoparticles, which result in collective oscillations of electron clouds at the interface of metal particles and polymer matrix (surface plasmons). The resonance frequency of such oscillations is strongly dependent on the metal, the surrounding polymer medium as well as the nanoparticle size and shape distribution.The light absorption range can vary from UV-Vis region up to infrared wavelengths. The tunability of optical absorption by an adequate tailoring of nanoparticle size and shape makes metal nanocomposites suitable for interesting electrooptical and photovoltaic applications [26, 27].

After UV irradiation of samples with increasing amounts of silver nitrate at constant weight percentage of inititator, we generally obtained transparent films in the range 400–700 nm indicating the absence of aggregates larger than 400 nm. The formation of Ag nanoparticles during the polymerization was visually observed in samples (characterized by larger silver precursor amounts in the starting mixtures) by a chromatic change from colorless to yellow-brown as the amount of silver nitrate increases. The colour change was also confirmed by UV-Vis spectra (data not shown) characterized by an absorption peak around 420 nm, which is due to plasmon resonance of larger silver nanoparticles, as already reported by Zhang and

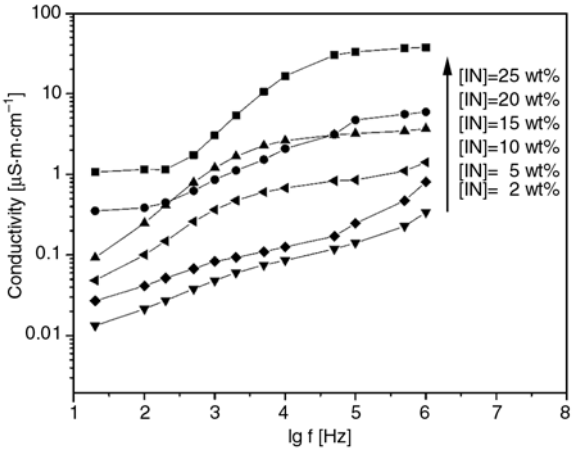

Figure 10. Filling factor dependent conductivity behaviour of PDMNPs

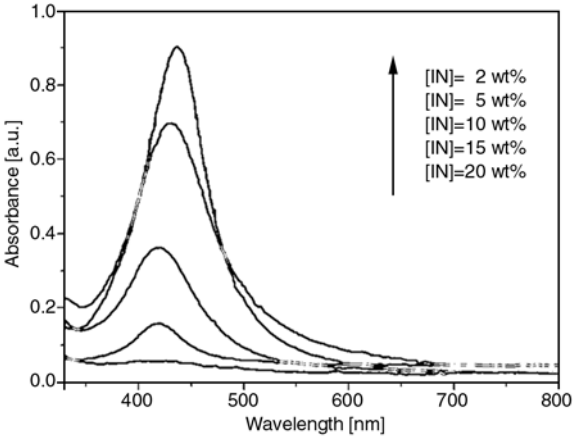

Figure 11. UV-Vis absorption spectra of PDMNPs for different amounts of photoinitiator ([$AgNO_3$] = 15 wt%)

Han [22]. We observed the typical red shift of absorption peak for larger $AgNO_3$ amounts, too.
We observed a similar behaviour when [$AgNO_3$] is kept constant and [IN] is reduced. In particular, the lower the IN concentration, the higher is the absorption peak. The UV-Vis absorption spectra for samples characterized by a silver nitrate amount of 15 wt% and different amount of photoinitiator are shown in Figure 11. In addition to the increase of absorption peak height, a clear red-shift in the absorption peak from 418 to 436 nm is observed as a function of decreasing IN content, indicating the particle size increase (which is consistent with TEM measurements, see above).

4. Conclusions

In this work we have shown that it is possible to finely control the morphology of polymer dispersed metal nanoparticles obtained by in situ polymerization of monomer and simultaneous metal ion reduction. The kinetics of polymerization and reduction reactions can be controlled by either using different amounts of metal precursor salt or changing the loading of photoinitiator in the starting mixtures, leading to different particle size and number density. The tuning of particle size and number density results in a fine tuning of both electrical and optical properties of PDMNP films allowing the manufacture of interesting electrooptical devices.

Acknowledgements

MIUR, the Italian Ministry for University is acknowledged for financial supports (Grant EX 60%, PRIN 2008).

References

[1] Biswas A., Aktas O. C., Schürmann U., Saeed U., Zaporojtechenko V., Faupel F., Strunskus T.: Tunable multiple plasmon resonance wavelengths response from multicomponent polymer-metal nanocomposite systems. Applied Physics Letters, **84**, 2655–2657 (2004).
DOI: 10.1063/1.1697626

[2] Convertino A., Capobianchi A., Valentini A., Cirillo E. N. M.: A new approach to organic solvent detection: High-reflectivity Bragg reflectors based on a gold nanoparticle/teflon-like composite material. Advanced Materials, **15**, 1103–1105 (2003).
DOI: 10.1002/adma.200304777

[3] Ajayan P. M., Schadler L. S., Braun P. V.: Nanocomposite science and technology. Wiley, Weinheim (2003).

[4] Fan F-R. F., Bard A. J.: Chemical, electrochemical, gravimetric, and microscopic studies on antimicrobial silver films. Journal of Physical Chemistry B, **106**, 279– 287 (2002).
DOI: 10.1021/jp012548d

[5] Ouyang J., Chu C-W., Szmanda R., Ma L., Yang Y.: Programmable polymer thin film and non-volatile memory device. Nature Materials, **3**, 918–922 (2004).
DOI: 10.1038/nmat1269

[6] Du H., Chenb H., Gong J., Wang T. G., Sun C., Lee S. W., Wen L. S.: Use of effective medium theory to model the effect of the microstructure on dc conductivity of nano-titanium films. Applied Surface Science, **233**, 99–104 (2004).
DOI: 10.1016/j.apsusc.2004.03.214

[7] Schürmann U., Takele H., Zaporojtechenko V., Faupel F.: Optical and electrical properties of polymer metal nanocomposites prepared by magnetron co-sputtering. Thin Solid Films, **515**, 801–804 (2006).
DOI: 10.1016/j.tsf.2005.12.249

[8] Ederth J., Johnsson P., Niklasson G. A., Hoel A., Hultåker A., Heszler P., Granqvist C. G., van Doorn A. R., Jongerius M. J., Burgard D.: Electrical and optical properties of thin films consisting of tin-doped indium oxide nanoparticles. Physical Review B, **68**, 155410–155420 (2003).
DOI: 10.1103/PhysRevB.68.155410

[9] Shenhar R., Norsten T. B., Rotello V. M.: Polymer-mediated nanoparticle assembly: Structural control and applications. Advanced Materials, **17**, 657–669 (2005).
DOI: 10.1002/adma.200401291

[10] Shiraishi Y., Toshima N.: Oxidation of ethylene catalyzed by colloidal dispersions of poly(sodium acrylate)-protected silver nanoclusters. Colloids Surface A: Physicochemical and Engineering Aspects, **169**, 59–66 (2000).
DOI: 10.1016/S0927-7757(00)00417-9

[11] Maye M. M., Chun S. C., Han L., Rabinovich D., Zhong C. J.: Novel spherical assembly of gold nanoparticles mediated by a tetradentate thioether. Journal of the American Chemical Society, **124**, 4958–4959 (2002).
DOI: 10.1021/ja025724k

[12] Giri A. K.: Magnetic properties of iron-polyethylene nanocomposites prepared by high energy ball milling. Journal of Applied Physics, **81**, 1348–1350 (1997).
DOI: 10.1063/1.363870

[13] Schürmann U., Hartung W. A., Takele H., Zaporojtchenko V., Faupel F.: Controlled syntheses of Ag-polytetrafluoroethylene nanocomposite thin films by co-sputtering from two magnetron sources. Nanotechnology, **16**, 1078–1082 (2005).
DOI: 10.1088/0957-4484/16/8/014

[14] Takele H., Jebril S., Strunskus T., Zaporojtchenko V., Adelung R., Faupel F.: Tuning of electrical and structural properties of metal-polymer nanocomposite films prepared by co-evaporation technique. Applied Physics A: Materials Science and Processing, **92**, 345–450 (2008).
DOI: 10.1007/s00339-008-4524-0

[15] Martinu L., Biederman H.: Monitoring the deposition process of metal-doped polymer films using optical emission spectroscopy. Plasma Chemistry and Plasma Processing, **5**, 81–87 (1985).
DOI: 10.1007/BF00567911

[16] Brust M., Walker M., Bethell D., Schiffrin D., Whyman R.: Synthesis of thiol-derivatised gold nanoparticles in a two-phase liquid-liquid system. Journal of the Chemical Society, Chemical Communications, **1994/7**, 801–802 (1994).
DOI: 10.1039/C39940000801

[17] Liu H., Ge X., Ni Y., Ye Q., Zhang Z.: Synthesis and characterization of polyacrylonitrile-silver nanocomposites by γ-irradiation. Radiation Physics and Chemistry, **61**, 89–91 (2001).
DOI: 10.1016/S0969-806X(00)00383-2

[18] Zhang Z., Zhang L., Wang S., Chen W., Lei Y.: A convenient route to polyacrylonitrile/silver nanoparticle composite by simultaneous polymerization-reduction approach. Polymer, **42**, 8315–8318 (2001).
DOI: 10.1016/S0032-3861(01)00285-3

[19] Gandubert V. J., Lennox R. B.: Assessment of 4-(dimethylamino)pyridine as a capping agent for gold nanoparticles. Langmuir, **21**, 6532–6539 (2005).
DOI: 10.1021/la050195u

[20] Majima T., Sakamoto M., Tachikawa T., Fujitsuka M., Majima T.: Two-color two-laser fabrication of gold nanoparticles in a PVA film. Chemical Physics Letters, **420**, 90–94 (2006).
DOI: 10.1016/j.cplett.2005.12.053

[21] Yagci Y., Sangermano M., Rizza G.: In situ synthesis of gold-cross-linked poly(ethylene glycol) nanocomposites by photoinduced electron transfer and free radical polymerization processes. Chemical Communications, **24**, 2771–2773 (2008).
DOI: 10.1039/b803279c

[22] Zhang Z., Han M.: One-step preparation of size-selected and well-dispersed silver nanocrystals in polyacrylonitrile by simultaneous reduction and polymerization. Journal of Materials Chemistry, **13**, 641–643 (2003).
DOI: 10.1039/b212428a

[23] Dey A., Karan S., De S. K.: Thermal and electric properties of CeO2 nanoparticles dispersed in polyethylene oxide: NH_4ClO_4 complex. Solid State Ionics, **178**, 1963–1968 (2008).
DOI: 10.1016/j.ssi.2007.12.063

[24] Hong S. U., Jin J. H., Wong J., Kang Y. S.: Polymer-salt complexes containing silver ions and their application to facilitated olefin transport membranes. Advanced Materials, **12**, 968–971 (2000).
DOI: 10.1002/1521-4095(200006)12:13<968::AID-ADMA968>3.0.CO;2-W

[25] Heilmann A.: Polymer films with embedded metal nanoparticles. Springer, Berlin, (2003).

[26] Westphalen M., Kreibig U., Rostalski J., Luth H., Meissner D.: Metal cluster enhanced organic solar cells. Solar Energy Materials and Solar Cells, **61**, 97–105 (2000).
DOI: 10.1016/S0927-0248(99)00100-2

[27] Pillai S., Catchpole K. R., Trupke T., Green M. A.: Surface plasmon enhanced silicon solar cells. Journal of Applied Physics, **101**, 093105/1–0931105/8 (2007).
DOI: 10.1063/1.2734885

eXPRESS Polymer Letters Vol.4, No.2 (2010) 79–93
Available online at www.expresspolymlett.com
DOI: 10.3144/expresspolymlett.2010.13

Fire-retardant and fire-barrier poly(vinyl acetate) composites for sealant application

*Z. Al-Hassany, A. Genovese, R. A. Shanks**

CRC for Polymers, School of Applied Sciences, RMIT University, GPO Box 2476V Melbourne 3001, Australia

Received 4 May 2009; accepted in revised form 10 November 2009

Abstract. Fire-retardant ceramifying poly(vinyl acetate) (PVAc) sealants have been prepared. The degradation of PVA was integrated with the action of the fire retardants to reduce flammable gases, produce carbonaceous char and convert the fillers into a self-supporting ceramic barrier. PVA is readily degraded by elimination of acetic acid, yielding a char that provides a transitory phase as the filler particles fuse into a ceramic mass. Acetic acid is eliminated at similar temperature to the release of water from magnesium hydroxide fire-retardant, thereby diluting flammable acetic acid. The residual oxide from the fire-retardant filler and structural filler are fused by a flux, zinc borate. The degradative and ceramifying processes were characterised using thermogravimetry, infrared spectroscopy, scanning electron microscopy and ceramic strength. Thermogravimetry of the composites was compared with additive mass loss curves calculated from the components. Deviations between the experimental and additive curves revealed interactions between the components in the composites. The modulus of the PVAc composites and the strength of their ceramic residues after combustion were determined.

Keywords: *thermal degradation, poly(vinyl acetate), fire-retardant, zinc borate, clay*

1. Introduction

There is considerable interest in the field of fire-retardant polymer based materials as the demand for improved safety in domestic, public and industrial situations is required by fire-safety standards. The most successful fire-retardant compounds for poly(vinyl acetate) (PVAc) materials are those that react chemically with the substrate and act in the condensed phase. Compounds that form part of a composite ideally should exhibit multifunctional ability. Examples of such fire-retardants are magnesium hydroxide ($Mg(OH)_2$) and zinc borate ($2ZnO{\cdot}3B_2O_3{\cdot}3.5H_2O$). Fire retardants change the decomposition path of polymers during heating so as to reduce the concentration of combustible volatiles and promote char formation. The char may be intumescent, offering heat and fire resistance until it reaches a critical temperature above which it burns [1–3].

The use of intumescent char systems is important for building infrastructure protection where emulsion polymers have been applied in coatings, paints and sealants. On heat exposure of these type of materials, activation and formation of an intumescent char occurs that provides an insulating barrier between the fire and the underlying substrate. An intumescent char normally results from a significant volume increase or thickness of a foam-like layer. Fire protection by coatings that proceed via intumescence increase the path for heat transfer and increase the thermal gradient from the charred surface to the substrate polymer [4]. A structure requires stabilisation for a char with structural integrity to be formed, and this is achieved by fusion or by promoting adherence of condensed layer components, such as formation of a ceramic-like phase. Various components are used to provide this function; a silicate mineral providing a struc-

*Corresponding author, e-mail: robert.shanks@rmit.edu.au

tural network, binders such as zinc borate that are capable of forming an amorphous phase on softening and a fluxing capability. Other components can be added to provide fire retardant functions and to participate in structure formation [5–15].

A series of kaolin and talc composites with varying filler content was investigated with particular attention to the formation of a fused char or ceramic. Talc and kaolin were used to enhance the stiffness and strength of the composite and ceramic materials. In addition to the component properties, the mechanical characteristics of these materials are influenced by the interfacial interactions that depend on the interface and the cohesive strengths. Thermal degradation of PVAc gives quantitative yields of acetic acid, produced by an elimination reaction leading to a polyalkene residue [16, 17]. This process gives rise to the formation of an intumescent residue with conjugated C=C bonds with cyclic and aromatic structures [18]. The double bonds produced by the elimination of acetic acid lead to an increase in the rate of adjacent thermal degradation. The degradation of PVAc occurs in two stages: the first stage starts at 350°C, and the second stage at 400°C. Simultaneously, the fire retardants undergo decomposition over similar temperature ranges although their presence enhances the PVAc thermal stability. The PVAc intumescent char maintained the structure while a ceramic-like residue formed. The importance in maintaining a structure throughout the polymer decomposition and ceramic formation was influenced by the filler system and amount that is shown by the scanning electron microscopy (SEM) observations.

The aim was to interpret the action of ceramic barrier forming components on PVAc composites and their interactions according to their thermal decomposition reactions and analytical temperature–structural analyses. The changes in char structure of the pure polymer and the composite with temperature were identified with Fourier transform infrared (FTIR) spectroscopy. An objective was the formation of a fused ceramic char that provides cohesive strength to maintain structural integrity during and after a fire. The effect of mineral type (kaolin or talc) and filler amount on the structure formed was evaluated through thermal stability measurements by thermogravimetry (TGA) and strength of char formed at elevated temperature. Fire retardant sealant composites mechanism of action as fire-retardants in conjunction with char forming components that form a structural ceramic to maintain seal integrity is discussed.

2. Experimental

2.1. Materials

PVAc was obtained from Nuplex Industries Pty Ltd (Australia) as an emulsion of 55% homopolymer in water. The calcined kaolin (K) was obtained from Burgess Pigment Company, Sandersville, GA, USA. The talc (T)(T38A) was obtained from Unimin Ltd, Australia. Magnesium hydroxide (M)(Magnifin 10H) was obtained from Magnesiaprodukte GmbH and Company KG, Germany. Zinc borate (ZB)(Firebrake ZB) was obtained from US Borax.

2.2. Composite preparation

Three sets of composites were prepared with varying polymer weight fraction (0.6, 0.5, 0.4 and 0.3). The filler mixtures have composition: Set A containing kaolin (0.57), $Mg(OH)_2$ (0.24), zinc borate (0.1) and glass frit (0.09), Set B containing mineral (either kaolin or talc) (0.57), $Mg(OH)_2$ (0.34), glass frit (0.09) (without zinc borate), and Set C containing talc (0.57), $Mg(OH)_2$ (0.24), zinc borate (0.1) and glass frit (0.09). The filler mixture was pre-blended in dry form. Using the abbreviations defined in Materials, the code for each composite includes the name PVAc, followed by K or T, and ZB or NZB (for no ZB) with the number after the component designating its weight fraction.

The filler mixture was pre-blended in dry form. The composites were prepared using an IKA-Werke stirrer Eurostar power control-viscosity model P4 with kneading stirrer blade operating at ~290 rpm. The required amount of polymer was weighed and placed into a stainless steel mixing container. The corresponding filler was slowly added into the stirred emulsion for a minimum of 5 min to obtain a uniform mixture. The thick paste mixture was spread into a Teflon based mould (3 mm) and dried at room temperature overnight followed by further drying under vacuum at 60°C for 48 h.

2.3. Thermogravimetry

Thermal degradation studies of the polymer and composites were conducted on a Perkin-Elmer TGA7. The samples were heated in an inert atmosphere of nitrogen with flow rate of 10 ml·min^{-1} over the temperature range of 30 to 850°C at 10°C·min^{-1}. The sample mass was ~10 mg and the changes in mass detected by the microbalance were recorded as a function of temperature.

PVAc was heated from 30°C to preselected temperatures determined from a thermogram (360, 445 and 500°C) at the same heating rate. At the end of the heating treatment, the residue was rapidly cooled to ambient temperature and stored in a desiccator for FTIR analysis.

2.4. Fourier transform infrared analysis

A Perkin-Elmer model 2000 Fourier transform infrared (FTIR) spectrometer was used in diffuse reflectance infrared Fourier transform (DRIFT) mode for the polymer and polymer residues obtained at the various temperatures noted previously. The spectra were obtained at a resolution of 8 cm^{-1} over the range of 4000–400 cm^{-1} with 16 accumulated scans. The scans were obtained under a nitrogen purge.

2.5. Thermomechanometry

Dynamic force (force changing linearly with time) – thermomechanical (df-TM) analysis of the polymer composite and residues were performed in three-point bend mode using a Perkin-Elmer DMA7e. The flexural modulus of the polymer composites was determined. Each polymer composite was placed on the three point bend fixture and a dynamic force scan was applied from 25 to 8000 mN at 150 mN·min^{-1}. The linear region was used for Young's modulus and modulus at 0.2% strain. Measurements were conducted at least in triplicate.

The breaking strength of the chars was measured, after subjecting the composite to, various temperatures in an electric muffle furnace using an Instron model 4465 universal test instrument. A three-point bend configuration was used with a maximum static load of 100 N and crosshead speed of 0.2 mm·min^{-1}. The rectangular specimen length was 30 mm and the width was 13 mm. Ultimate stress was selected when fracture occurred as indicated by a rapid reduction of the load. It was calculated using Equation (1) (for rectangular specimens):

$$S = \frac{3PL}{2bd^2} \tag{1}$$

where S is the maximum stress; P, load; L, span; b, width of the specimen; and d, depth of the specimen.

3. Results and discussion

3.1. Degradation of PVAc

TGA mass and derivative curves for PVAc treated under N_2 at heating rate of 10°C·min^{-1} are shown in Figure 1. The majority of mass loss took place at 354°C due to acetic acid elimination from the polymer side-chains. This was followed by a smaller mass loss from the breakdown of the polymer backbone at the higher temperature of 450°C. These unsaturated sequences re-arrange and decompose to aromatic and aliphatic hydrocarbons as will be confirmed by FTIR. The first stage of degradation was almost exclusively elimination of side groups, and the second stage was due to the thermal degradation of the polyalkene structures produced by the elimination reaction [16, 17]. A complex array of free radical reactions, rearrangements and chain scissions led to the decomposition of the main chain as observed by the second slower mass loss (~6%·min^{-1}) in the mass loss curve. The derivative curve shows the mass loss steps as peaks.

Figure 1 reveals a gradual mass loss below 200°C that is attributed to the presence of tightly bound

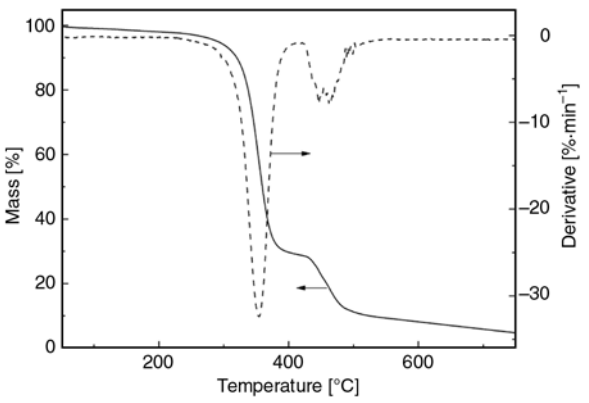

Figure 1. Thermogravimetric mass loss (—) and derivative (- - -) for the decomposition of PVAc under an inert atmosphere with heating rate of 10°C·min^{-1}

water or traces of un-reacted monomer in the emulsion polymer that was not volatilised during the drying stage. The remaining mass loss at 420–480°C is ascribed to the slower pyrolysis of the char that had formed through the main decomposition. A small residual amount (4% for PVAc) still remained at 850°C. The amount of acetic acid content of PVAc was determined theoretically by stoichiometry to be 72%·wt assuming quantitative loss of acetic acid. This means that the complete elimination of all acetate side-groups would lead to a char of ~28% confirming that elimination of acetic acid was the predominant degradation process.

An indication of the degradation stages, temperature ranges and the nature of the reactions in each stage of PVAc were followed by FTIR. The FTIR spectra of PVAc residues are shown in Figure 2, at the temperatures indicated. The characteristic peaks of PVAc are summarised in the literature, and the current PVAc spectrum was compared with reference spectra [4, 16]. PVAc shows asymmetric aliphatic CH_3 and CH_2 bands (ν_a: 3000, 2951 cm^{-1}, respectively) and their symmetric bands (ν_s: 2898, 2849 cm^{-1}, respectively) are present [4, 16, 17]. The aliphatic CH_3 has a band at 1422 and 1375 cm^{-1} corresponding to an asymmetric and a bending vibration. The ester carbonyl (C=O) of the functional group symmetric band appeared at 1753 cm^{-1} and the C–O–C asymmetric and symmetric vibrations appeared at 1271 and 1115 cm^{-1}, respectively [16].

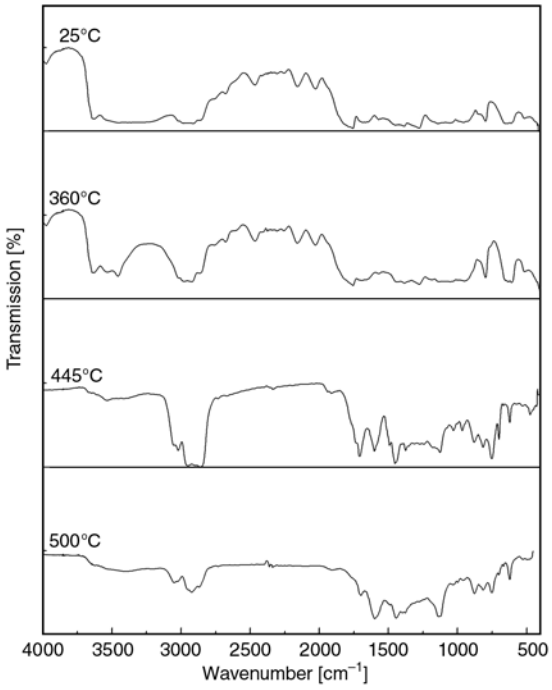

Figure 2. FTIR spectra of PVAc film from the emulsion at various stages of decomposition, obtained under an inert atmosphere; temperatures are indicated on the graph

The FTIR spectra of PVAc residues obtained at 360°C show peaks at 1753 cm^{-1} indicating that ester groups are still present, and the elimination of acetic acid at the end of the first stage is not fully complete. This effect can be due to the chain reaction of acetic acid elimination leaving some isolated ester groups between two double bonds in the polymeric structure of the residue; the 2921 and 1691 cm^{-1} bands characteristic of the internal unsaturation are fully developed. Simultaneously, there are signs of aromatisation bands that appeared at 1570, 797 and 633 cm^{-1}, and the 1382 band moves to 1453 cm^{-1}. At 445°C the FTIR spectra of PVAc residues obtained were the same, as there was an increase in the degree of aromatisation in the residue and a decrease in the absorption of conjugated double bonds (942 cm^{-1}) and increased absorptions at 2921 and 1437 cm^{-1}. The presence of 760 cm^{-1} is attributed to the aromatic C–H bending. A new C=O band appeared at 1706 cm^{-1} at 500°C. Hydroxyl and carbonyl groups are evident in the spectra obtained at high temperatures. This may arise from aromatisation of the aliphatic structures, as observed in the spectra of PVAc heated at 500°C, which revealed a complete loss of aliphatic hydrocarbon groups (2921 cm^{-1}) and a partial loss of carbonyl species. A high content of aromatic rings is fully developed as seen from the C–H vibration of substituted polycondensed aromatic ring (870, 820, 760 and 700 cm^{-1}).

3.2. Degradation of PVAc composites

The thermal decomposition of filled PVAc composites containing kaolin or talc were investigated by incorporation of increasing amount of a particulate filler from 0.4 to 0.7 wt fraction, although we refer to composites in regard to polymer content as detailed in Table 1. The thermogravimetric decomposition and corresponding derivative curves for the kaolin series (Set A) are displayed in Figure 3. Figure 3a shows the degradation of PVAcK0.6, containing 0.6 wt fraction kaolin. The curve shows several stages in the decomposition profile with the onsets of each stage at 276, 344, 450 and 573°C. The derivative curve shows the stages more clearly

Table 1. Thermogravimetry of PVAc and filled kaolin and talc composites series

Composition	Mineral	Composite ratio PVAc : Filler	T_{onset} [°C]	Derivative peak [°C]	Mass remaining at 850°C [%]	Rate of polymer degradation [%·min^{-1}]
PVAc	–	100:0	347 488	354 (1) 450 (2)	4	–5.53
PVAcK0.6	Kaolin	60:40	276 344 450 573	278 (1) 389 (2) 487 (3) 643 (4)	36	–1.32 –12.72 –14.05 –3.27
PVAcK0.5	Kaolin	50:50	275 322 439	286 (1) 349 (2) 472 (3)	51	–0.79 –12.01 –2.45
PVAcK0.4	Kaolin	40:60	323 446	342 (1) 474 (2)	59	–15.11 –3.01
PVAcK0.3	Kaolin	30:70	332 444	354 (1) 479 (2)	70	–9.31 –1.75
PVAcT0.6	Talc	60:40	284 350 460	278 (1) 375 (2) 389 (3) 492 (4)	40	–1.32 –12.62 –14.05 –3.27
PVAcT0.5	Talc	50:50	273 345 463	276 (1) 357 (2) 382 (3) 487 (4)	48	–1.01 –9.77 –13.85 –2.65
PVAcT0.4	Talc	40:60	255 341 390 462	269 (1) 356 (2) 413 (3) 490 (4)	55	–1.05 –10.04 –8.04 –1.81
PVAcT0.3	Talc	30:70	268 301 390)	258 (1) 320 (2) 352 (3) 445 (4)	68	–0.56 –11.87 –8.62 –1.54

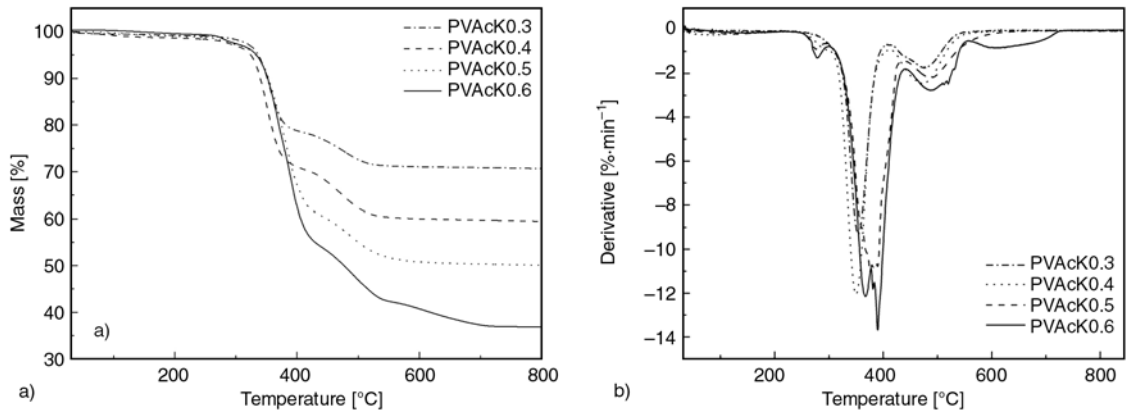

Figure 3. a) Thermogravimetric mass loss and b) derivative curves of fire retardant kaolin composite series under an inert atmosphere (Set A)

by the presence of the peaks as the mass loss rate changes. As previously observed, PVAc exhibited a small mass loss at temperature below 200°C. In this range the fillers themselves lose negligible mass. A small mass loss at higher temperature was observed at 278°C as indicated by the small peak in the curve. The peak is attributed to the formation of water arising from $Mg(OH)_2$ and the early stages of dehydration of zinc borate. Both these fire retarding fillers begin to decompose at similar temperatures (>250°C). The maximum rate of mass loss occurs at 407°C (~0.8%·min^{-1}) for $Mg(OH)_2$ while zinc borate has two overlapping mass losses at 378 and 411°C (~0.7%·min^{-1}) (Figure 4). Meanwhile, in the same temperature region, the deacetylation of PVAc occurs followed by structural disintegration

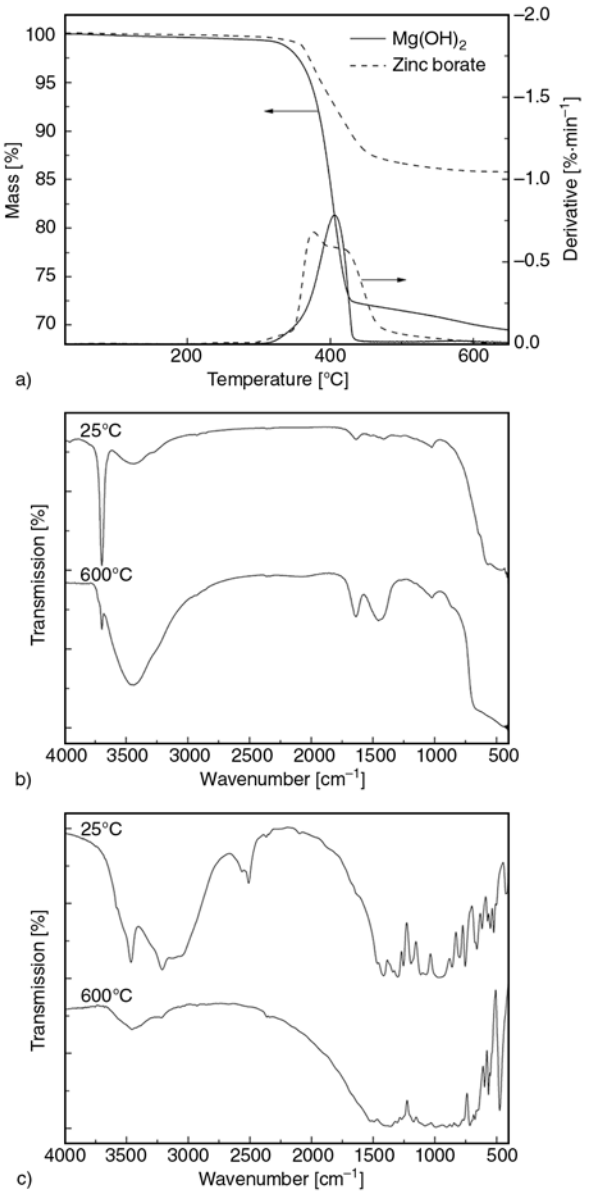

Figure 4. a) Thermogravimetry mass loss and derivative curves for fire retardants, $Mg(OH)_2$ (—) and zinc borate (- - -) under an inert atmosphere, b) FTIR of $Mg(OH)_2$ at 25°C and after degradation at 600°C, c) FTIR of zinc borate at 25°C and after degradation at 600°C

of the polyolefin species, formation of aromatic species, isomerisation and formation of volatile compounds. The main decomposition temperature region encompassing these mass losses of various volatiles has resulted in a shift towards higher temperature. The degradation of PVAcK0.5 (Figure 3b) is similar to the degradation of PVAcK0.6 composite although it showed three stages of degradation, as the decomposition of fillers retards the polymer decomposition. These two composites decomposed at higher temperature compared with the original PVAc. This was due to the presence of fire retardant $Mg(OH)_2$ and zinc borate in the PVAc composites which caused the deacetylation reaction to shift to higher temperature. The endothermic release of water from both fire retardants absorb heat while water formed and vaporised, cooling the substrate, particularly since $Mg(OH)_2$ has a relatively high endothermic enthalpy of 1450 $J \cdot g^{-1}$ [19]. The water loss results in a decrease in the onset of the decomposition as listed in Table 1. Additionally, the shift in main polymer decomposition may also be due to the volatiles being absorbed on the filler surfaces, hence reducing mass loss until higher temperature is reached. This has been suggested to occur with $Mg(OH)_2$ as it forms a high surface area inorganic MgO after decomposition [19]. The total amount of water eliminated on thermal dehydration of the $Mg(OH)_2$ corresponded to 30.8%·wt and is consistent with theoretical value.

FTIR of $Mg(OH)_2$ at ambient temperature and after degradation at 600°C is shown in Figure 4b. At ambient temperature the spectrum reveals the absorption OH bands that appeared at 3698 cm^{-1}. The elimination of water and the formation of MgO is eventually seen in the spectrum of the $Mg(OH)_2$ heated at 600°C with a broad band developed in the range of 3698 and 2750 cm^{-1}, and appearance of new bands of 1650 and 1450 cm^{-1}.

Studies which illustrated the effectiveness of $Mg(OH)_2$ as a flame retardant in polymers have concluded that $Mg(OH)_2$ is effective at reducing smoke emissions from burning polymers [20]. In addition to the endothermic decomposition, the fire retardant slows the rate of thermal degradation of the polymer by dilution of the fuel supply with water vapour present in the gaseous phase. These factors, and its high heat capacity, reduce the thermal energy available to degrade the polymer [21]. The MgO provides an increased insulation barrier for the polymer from the heat source through char formation [22].

The high filler content composites PVAcK0.4 and PVAcK0.3 (Figure 3c, 3d respectively) show two main stages of degradation with onset at 322 ± 10°C and the maximum rate of mass loss at 349°C. This indicates that the fire retardants enhance the thermal stability, as the material degrades more slowly at 439°C with a maximum mass loss at 472 ± 5°C. A 7 to 10% residue is formed at 500°C that is stable

to 800°C. The decomposition for high filler content, starts at comparatively lower temperature, but the material is more stable over a higher temperature range, i.e. up to 500°C, for reasons explained earlier. Whereas high polymer content (PVAcK0.6 and PVAcK0.5), degradation starts at higher temperature and the material is stable at 800°C. Decomposition products continue to degrade by random chain scission to form the final product that contains polyalkene residue, MgO and boron oxide with a lower molar mass.

According to Sivalingam and Madras [23], the PVAc is mildly affected by the metal oxide in this case (MgO). The degradation of PVAc starts with the release of acetic acid and this can react with the metal oxide (MgO) to form metal acetate. Therefore MgO may have induced the decrease in the decomposition temperature from the catalytic basic oxide surfaces. From 300–400°C, the degradation of the polymer composites was high due to anticipated degradation of $Mg(OH)_2$. In the 400–530°C temperature range the degradation of polymer composites was lower than the expected. This may be due to the reaction of the additives with the products of degradation of PVAc.

The action of zinc borate comes into account primarily for its fluxing and purpose of binding the inorganic fillers in the composite. Zinc borate is able to undergo dehydration, ~11%·wt of water in the temperature range of 290–450°C, although the endothermic process is less effective than $Mg(OH)_2$. A small proportion of zinc borate, in particular $2ZnO{\cdot}3B_2O_3{\cdot}3H_2O$, acts as a synergistic agent in polyolefins as has been cited in literature [7, 24] and hence this is extended in PVAc-based formulations. The dehydration can be described by Equation (2) that has an amorphous structure with boric oxide beneficial for the purpose of improving the char properties:

$$2ZnO{\cdot}3B_2O_3{\cdot}3H_2O \rightarrow 2ZnO{\cdot}3B_2O_3 + 3H_2O \qquad (2)$$

FTIR of zinc borate at ambient temperature and after degradation at 600°C is shown in Figure 4c. At ambient temperature zinc borate spectrum reveals absorption bands that appeared at 3490, 3250 and 2500 cm^{-1} respectively. These bands have disappeared after the calcination of zinc borate at 600°C due to the elimination of water and the formation of the new amorphous zinc borate which is eventually seen in the spectrum with a broad band that developed in the range of ~3700 and 2700 cm^{-1}.

Figure 5a and 5b show the kaolin-$Mg(OH)_2$ and talc-$Mg(OH)_2$ filled PVAc with no zinc borate for the high and low polymer content. It can be observed that both the mineral-$Mg(OH)_2$ composites show several degradation stages. The first stage is indicated by a small peak due to the formation of water arising from the beginning of $Mg(OH)_2$ decomposition. The second stage shows that acetic acid elimination from PVAc started to occur, both overlapping with volatile formation simultaneously formed. The third stage is attributed to the structural degradation of the polyalkene backbone in the PVAc.

The TG curves of the PVAc composites revealed an interaction between zinc borate and $Mg(OH)_2$ that took place during $Mg(OH)_2$ decomposition. Zinc borate degrades well above 380°C (Figure 4a). The heat treatment of $Mg(OH)_2$ and zinc borate in the polymer leads to the formation of boric oxide; this behaviour has been shown to occur with different zinc borates [25, 26]. Boric oxide is said to form an

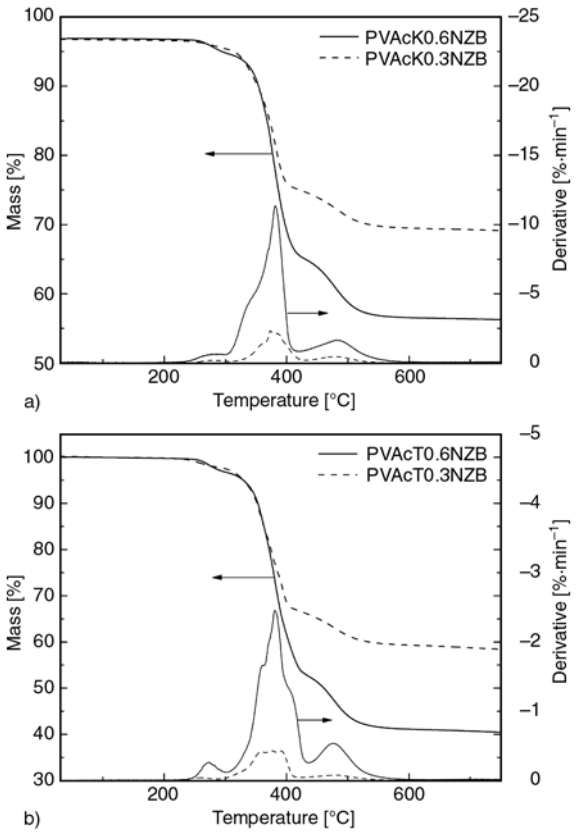

Figure 5. Thermogravimetric mass loss and derivative curves of fire retardant a) kaolin-$Mg(OH)_2$ and b) talc-$Mg(OH)_2$ composite series with no zinc borate (NZB) under an inert atmosphere (Set B)

amorphous glassy layer as a low temperature-fluxing component. This enabled it to function by binding filler particles and inhibiting oxygen mass transfer to the polymer fuel system and retarding further oxidation of the char.

Composites containing $Mg(OH)_2$ as fire retardant component with no zinc borate (NZB) (Set B) (Figure 5) were prepared for comparison with the zinc borate composite systems. Several decomposition stages still occurred due to water released from $Mg(OH)_2$, the elimination of acetic acid and decomposition of polyalkene residue. The polymer decomposition rate for PVAcK0.6 was –12.72 and –2.12%·min^{-1} with and without zinc borate, respectively, indicating that the presence of zinc borate was important in the composites as it acts as a synergistic agent when it is introduced with $Mg(OH)_2$. The mechanism of action of $Mg(OH)_2$ to form a protective MgO-ceramic and zinc borate reinforces its efficiency by acting as a binder (formation of B_2O_3–ZnO glass). This MgO-ceramic residue combined with the degraded polymeric material leads to a protective surface layer during decomposition.

The onset of each stage was at 264, 358 and 455°C for PVAcK0.6NZB, 260, 354 and 459°C for PVAcT0.6NZB, 269, 327, 381 and 484°C for PVAcK0.3NZB, and 259, 357, 375, 394 and 479°C for PVAcT0.3NZB. This suggested that excluding zinc borate decreased the onset temperature in comparison with PVAcK0.6, PVAcT0.6, PVAcK0.3 and PVAcT0.3 that contain zinc borate. Table 2 lists the stages showing that without zinc borate present in the composite the degradation stages start at lower temperature. Consequently this indicated that having $Mg(OH)_2$ by itself in the composites lead to an early decomposition for all of the four composites because of the release of water from $Mg(OH)_2$ effectively cooling the substrate through the endothermic reactions that act in relation to fire resistance. Eliminating zinc borate leads to the disappearance of the amorphous phase, since zinc borate effect is due to the softening and retaining/trapping volatiles.

The substitution of kaolin by talc (Set C) leads to significant changes in the thermal stability, where the mass loss onset occurred at lower temperatures and improved thermal stability of the polymer composite decomposition. The deacetylation of the PVAc was shifted toward higher temperatures. The platelet structure of talc (2:1 layer structure, octahedral sheet sandwiched by two tetrahedral sheets) is compared with the structure of kaolin (1:1 layer structure, tetrahedral and octahedral sheets). Talc, having a smaller particle size and better wettability by polymers, enabled better dispersion and hence barrier properties to be formed [18]. The TG mass loss and derivative profiles of PVAcT0.6, PVAcT0.5 PVAcT0.4 and PVAcT0.3 shown in Figure 6 revealed four stages of degradation, as emphasised by the derivative curves.

The first small peak at ~270°C is attributed to the formation of water arising from $Mg(OH)_2$ and zinc

Table 2. Thermogravimetry of filled kaolin and talc composites with no zinc borate (NZB)

Composition	Mineral	Composite ratio PVAc : Filler	T_{onset} [°C]	Derivative peak [°C]	Mass remaining at 850°C [%]	Rate of polymer degradation [%·min^{-1}]
PVAcK0.6NZB	Kaolin	60:40	264 (1) 358 (2) 455 (3)	276 (1) 374 (2) 382 (3) 479 (4)	39	–0.19 –2.32 –2.12 –0.46
PVAcK0.3NZB	Kaolin	30:70	251 (1) 353 (2) 450 (3)	269 (1) 327 (2) 381 (3) 484 (4)	68	–0.59 –3.60 –11.32 –1.63
PVAcT0.6NZB	Talc	60:40	260 (1) 354 (2) 459 (3)	272 (1) 359 (2) 380 (3) 408 (4) 476 (5)	40	–1.44 –9.29 –13.73 –6.87 –2.99
PVAcT0.3NZB	Talc	30:70	249 (1) 344 (2) 451 (3)	259 (1) 357 (2) 375 (3) 394 (4) 479 (5)	68	–0.71 –8.42 –8.62 –9.14 –1.46

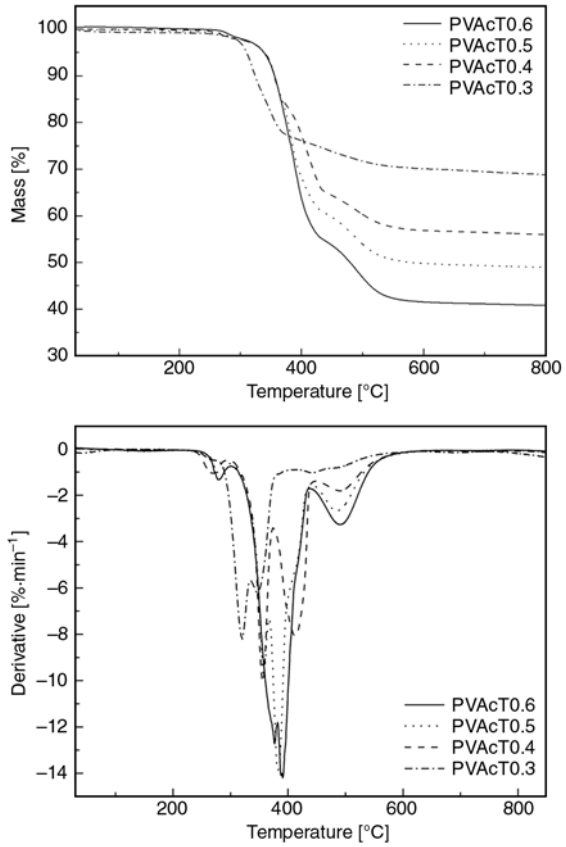

Figure 6. a) Thermogravimetric mass loss and b) derivative mass loss curves of fire retardant talc composite series under an inert atmosphere (Set C)

borate. The PVAcT0.4 and PVAcT0.3 (Figure 6c and 6d) show that this first peak is shifted to high temperature with the increased filler content, therefore a higher mass loss was observed than for PVAcT0.5 and PVAcT0.6 (Figure 6a and 6b) where the maximum mass loss occurred at ~350°C. The derivative curves for all talc composites show two overlapping peaks (350 and 390°C) due to the water loss from $Mg(OH)_2$ and zinc borate in the same temperature region where the deacetylation of PVAc occurred. This was followed by a small mass loss due to the polymer backbone at ~460°C. The third peak that occurred at 390°C was more pronounced for the composites with high filler content, perhaps because the filler absorbed some degradation products that decomposed at higher temperature and were retarded by the filler. Table 1 showed that the rate of mass loss of the polymer component in the talc series decreased with increased filler content.

TG curves shown in Figure 6 indicate that talc has both a strong catalytic effect on deacetylation reaction (first mass loss) and a charring effect [18]. The talc seemed to promote the formation of a polymer-filler char that was comparatively more thermally stable. The derivative peak showed a small shift to higher temperatures (from 347°C for pure PVAc to 350°C for PVAcT0.6). PVAcT0.3 degradation started at lower temperature as shown in Figure 6 since it consisted of the highest talc content. According to Durin-Frances *et al.* [27], where they investigated the synergism of the additives, they focused on the binary and ternary composites, and found greater synergism between talc and zinc borate than between zinc borate and magnesium hydroxide, because talc tended to increase the thermal conductivity of the polymer that was caused by the lamellar particles of talc. The kaolin itself was calcined with <1% mass loss present since organic matter and water would have been removed in the treatment, therefore the calcination process (dehydroxylation) was affected by the catalytic activity of kaolin compared with talc.

Theoretical curves were constructed from the individual component in their relative proportion to observe the influence of the fillers on the decomposition of the polymer. Figure 7 illustrates the enhanced thermal stability of the filled PVAc composites with the experimental and theoretical mass loss curves for the kaolin system. The effect on the PVAc degradation of adding the filler, in comparison with the calculated weight loss curves for respective amounts of each individual component, assumed that they were not influenced by each other. The measured mass loss indicated otherwise, with composites containing a high relative proportion of $Mg(OH)_2$ and zinc borate filler (PVAcK0.3 (a and a′) and PVAcK0.4 (b and b′)) exhibiting

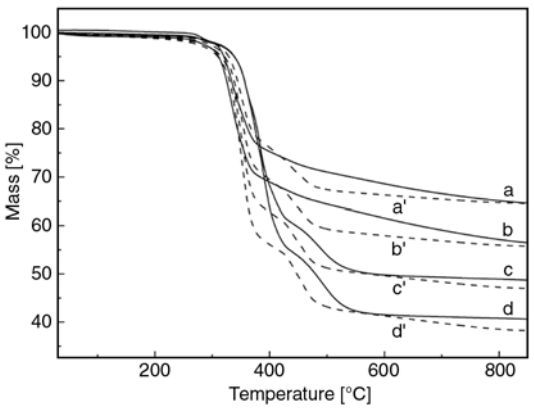

Figure 7. Thermogravimetric mass loss of fire retardant kaolin composite a) PVAcK0.3, b) PVAcK0.4, c) PVAcK0.5 and d) PVAcK0.6, measured and (a', b', c' and d') theoretically calculated

decomposition at similar lower temperatures for the first mass loss stage. As temperature increased to about 400°C, the mass loss rate measured was more gradual than that calculated.

Composites containing a lower amount of filler (PVAcK0.5 and PVAcK0.6) showed a higher temperature mass loss compared with the theoretical curve, indicating that a degree of mutual interactions existed between the phases present. The stages of decomposition for the acetic acid formation and pyrolysis of the polyalkene was more pronounced as the behaviour of the polymer degradation was the dominant process. These results show that although $Mg(OH)_2$ and zinc borate filler decreased the initial thermal stability of the composite, the rate of degradation of PVAc can be reduced through the various mechanisms described above.

3.3. FTIR analysis of PVAc kaolin composites series

The FTIR spectra of PVAcK0.6 degraded under nitrogen in the TGA furnace at increasing heat treatment temperatures (25, 325, 377, 427, 447 and 500°C) throughout the decomposition are shown in Figure 8. This composition was selected as it provides a high temperature residue with a low decrease in the onset temperature of degradation. The FTIR spectrum of the original composite at ambient temperature showed typical absorption bands that were due to the polymer and fillers. FTIR peaks were observed for $Mg(OH)_2$, while other peaks were due to zinc borate and kaolin (refer Figure 3b). The $Mg(OH)_2$ peaks are at 3696, 2923, 2363, 1638 and 1423 cm^{-1} respectively. The asymmetric aliphatic CH_3 and CH_2 bands from PVAc (ν_a: 3000, 2951 cm^{-1}, respectively) were shifted to 3015 and 2934 cm^{-1} respectively due to overlap of kaolin and $Mg(OH)_2$ bands. The aliphatic CH_3 has bands at 1422 and 1375 cm^{-1} corresponding to asymmetric and symmetric bending vibrations that were shifted to 1435 and 1379 cm^{-1} respectively due to the presence of kaolin and zinc borate [28, 29]. The ester carbonyl (C=O) of the functional group symmetric band that appeared at 1753 cm^{-1} was shifted to 1733 cm^{-1} due to $Mg(OH)_2$ and kaolin and the C–O–C asymmetric and symmetric vibrations that appeared at 1271 and 1115 cm^{-1} were shifted to 1261 and 1107 cm^{-1} respectively [30].

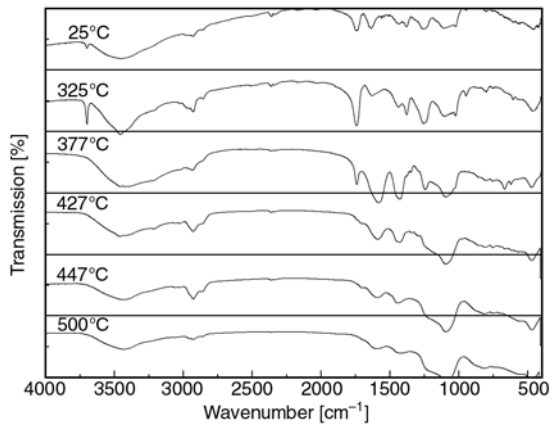

Figure 8. FTIR spectra of PVAcK0.6 residue degraded under an inert atmosphere at the various decomposition temperatures indicated on the graph

At 325°C, the spectrum shows the 3698, 3455 and 2925 cm^{-1} bands that characterise the presence of $Mg(OH)_2$, kaolin and zinc borate, a large band appeared at 1740 and 1630 cm^{-1} due to overlapping of kaolin and PVAc residue [31]. At 377°C the spectrum shows a broad band at 3415 cm^{-1} that demonstrates that the bands at 3698 and 3455 cm^{-1} were developed due to dehydration of zinc borate and the presence of MgO and aromatics (bands overlapping in the frequency range). Simultaneously, there are signs of aromatisation bands exhibited by the polymer that are detected at 1581, 801 and 621 cm^{-1}. Heat treatment at temperatures of 427, 476 and 500°C showed a similar spectrum to that at the previous temperature of 377°C. The spectrum shows the residue of the polymer and the fillers after the second stage of degradation that demonstrates that the bands are overlapped, and the main peaks present are 3430, 2926 (symmetric aliphatic CH_3 and CH_2 bands), 2360 (CH_3), 1592 (aromatic ring), 1417 (CH_2 of the vinyl group), 1093 (CH_2 of the vinyl group) and 812 cm^{-1} (aromatic ring) respectively. Peaks were observed for the formation of MgO at 3500, 1700 and 1500 cm^{-1}.

3.4. Mechanical properties

The flexural properties of the PVAc composites were measured to observe changes with filler content. The modulus at 0.2% strain and Young's modulus are listed in Table 3. The flexural modulus for the composites was increased from 27 to 370 MPa for the kaolin mineral based systems and from 7 to 470 MPa for the talc mineral, as expected for

Table 3. Modulus and residue strength of PVAc filled kaolin (Set A) and filled talc composites series (Set C)

Formulations	Modulus at 0.2% strain [MPa]	Young's modulus [MPa]	Residue strength [MPa]	
			400°C	1050°C
PVAcK0.6	27	106	0.12	1.68
PVAcK0.5	179	1090	0.36	2.95
PVAcK0.4	249	1660	0.58	6.67
PVAcK0.3	370	1980	1.01	16.90
PVAcT0.6	7	3	0.07	0.15
PVAcT0.5	19	30	0.81	0.36
PVAcT0.4	180	277	0.98	1.33
PVAcT0.3	470	708	1.49	5.12

increasing filler content. With low filler content, the composite displayed higher flexibility and this was reflected in the change in Young's modulus with higher filler content resulting in higher modulus of the composite. This is a typical trend for composites with the incorporation of rigid inorganic filler content [32].

Compositions PVAcK0.4 and PVAcK0.3 from the kaolin series, (modulus 249 and 370 MPa respectively) and PVAcT0.4 and PVAcT0.3 from the talc series (modulus 180 and 470 MPa respectively) that contained less polymer reveal higher Young's modulus indicating that these compositions were hard or stiff, whereas PVAcK0.6, PVAcK0.5 (modulus 27 and 179 MPa respectively), PVAcT0.6 and PVAcT0.5 (modulus 7 and 19 MPa respectively) with high polymer content exhibited lower Young's modulus. These attributes had a consequence on the resulting residual strength after the heat treatments. An initial difference between the modulus of the kaolin and talc series was observed, with the kaolin series generally higher than the modulus of the talc series. This was due to the different particle structure and interaction between PVAc and talc [33, 34] than between kaolin and PVAc.

After burning the composites at 400 and 1050°C, the phases underwent structural transformations. At 400°C the fire retardants had changed forms, with zinc borate contributing to formation of a flux that acted by binding of the other fillers present in the system, while a residual oxide was retained in the condensed phase from $Mg(OH)_2$. The strength of the PVAc composites after burning was caused by an increase in a ceramic-like residue for both kaolin and talc composites that increased with increasing filler content, however the cohesion of the residue was relatively weak. The residue strength increased with increasing temperature as higher temperature changes in the condensed phase involved with the filler systems were activated. At 400°C the residue strength of the kaolin composites (0.12, 0.36, 0.58, and 1.01 respectively) was lower than that at 1050°C (1.68, 2.95, 6.67 and 16.9 with increasing filler content). A similar trend was observed for the talc composites as listed in Table 3. At 400°C the strength was low (0.07, 0.81, 0.98 and 1.49 respectively) but at 1050°C the strength was increased (0.15, 0.36, 1.33 and 5.12 respectively). The talc residues were stronger than those obtained with kaolin.

The increase in the strength for kaolin filled PVAc composites was mainly due to shrinkage of the material after burning that led to improved fusion and increased polymer-filler interaction. Stronger interaction enabled more stress to be transferred from the polymer to the fillers during loading. In addition, studies revealed that the specific surface area was one of the more important characteristics of the filler, determining the amount of the surface contact between the polymer and the filler [22, 35]. Fillers with high surface area contribute to more surface contact between the filler and the polymer, increasing the mechanical properties of the composites. Fillers with fine or small particles have higher surface area than fillers with larger particle size. However the finer the particles, the greater was their tendency to agglomerate and this can cause an adverse effect on the mechanical properties as shown in the SEM (Figure 9). Figure 9a and 9b illustrate the SEM of PVAcK0.6 composite pyrolysed at 400°C. Large voids are observed between the particles due to the degradation of the polymer and fusion was observed to form a ceramic-like structure that is shown in Figure 9b (higher magnification of Figure 9a). Figure 9a reveals the continuous sheet structure of kaolin that produced thin particles, which are often found in nature as overlapping sheets. These sheets are bound via hydrogen bonding of the octahedral-layer hydroxyl face of one flake to the tetrahedral-layer oxygen face of an adjacent sheet.

At higher temperature (1050°C) Figure 9c and 9d show better fusion and reveal a higher stacking density of the fillers with a smaller distance between the particles. The talc composite PVAcT0.6 pyrolysed at 400°C is shown in Figure 9e and 9f. Many microvoids are present, compared with the kaolin

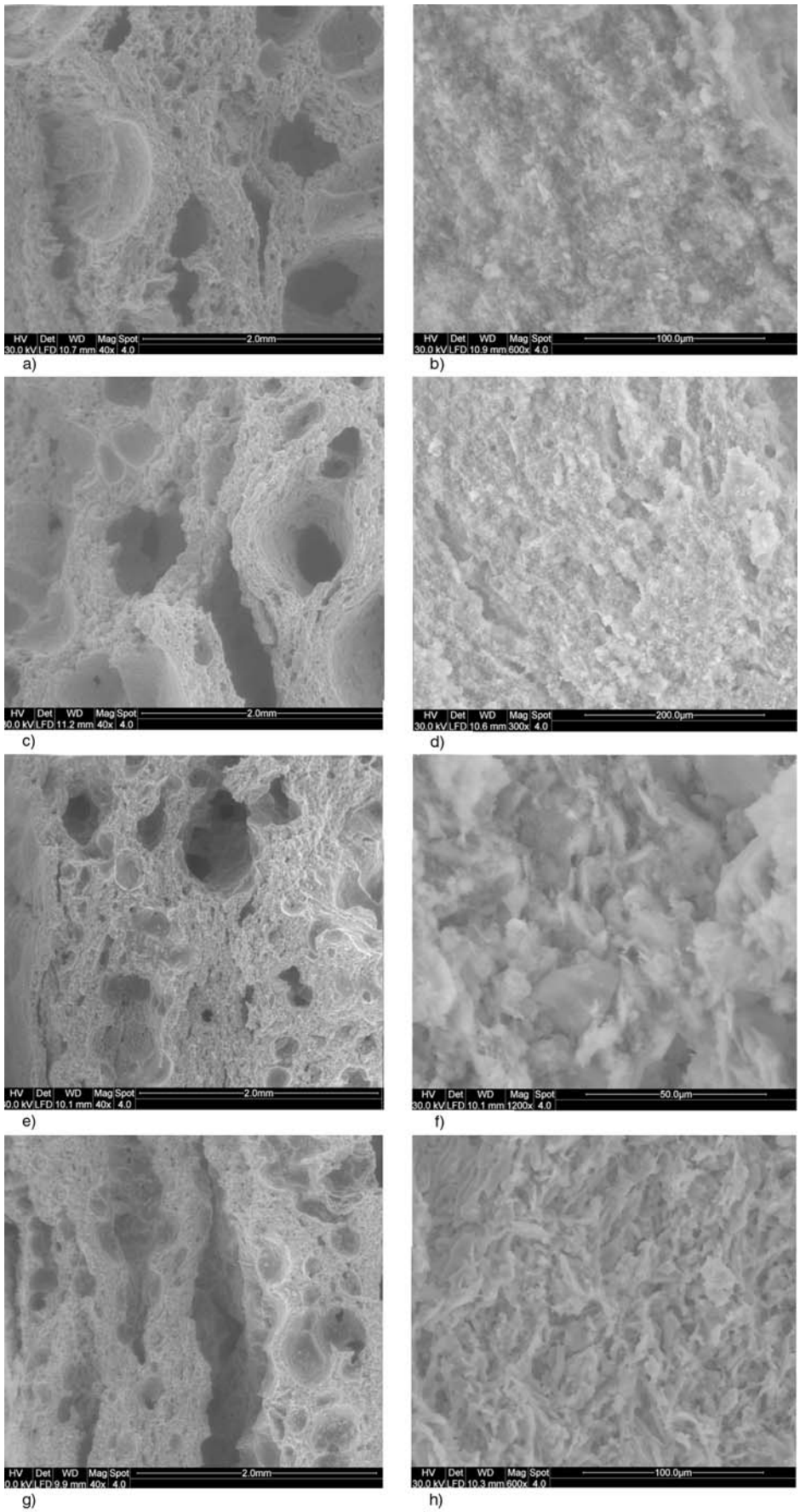

Figure 9. SEM observation of PVAcK0.6 furnaced at 400°C (a and b), at 1050°C (c and d), and PVAcT0.6 burned at 400°C (e and f) and at 1050°C (g and h)

composite, due to the platy nature of talc. As mentioned, talc can be better wetted by polymer. The good interaction between polymer and talc enabled improved distribution of polymer, therefore leading to many more microvoids being formed as polymer was volatilised. Figure 9g and 9h show the PVAcT0.6 furnaced at 1050°C revealing comparatively better fusion however more cracks were present than at 400°C. Figure 9h shows the large particle size of talc, therefore the strength of this material was less than the material that contained kaolin. Formation of a ceramic residue after degradation and volatilisation of the polymer has found application in fire barrier sealant composites that prevents fire spread though gaps in building components [36].

4. Conclusions

Poly(vinyl acetate) composites produced with kaolin or talc as structural fillers, and with fire retardant magnesium hydroxide and zinc borate flux, formed a ceramic char after thermal degradation. The ceramic char had similar shape and size to the original composite and had sufficient strength to provide a barrier to spread of fire. Poly(vinyl acetate) readily decomposes with release of acetic acid, however it forms a polyalkene residue that further degrades with formation of aromatic structures. Magnesium hydroxide eliminated water over the same temperature range as acetic acid was formed, thus diluting the flammable acetic acid. Individual degradation steps became less pronounced as the filler content increased due to restricted emission of volatiles through the tortuous filler path. The organic polyalkene char maintained integrity of the inorganic components over the temperature range where the zinc borate flux formed a ceramic with the talc or kaolin, and magnesium oxide formed. Talc was chosen for its platelet particles that strengthened the ceramic, though the smaller kaolin particles provided a stronger ceramic at similar concentration. Talc provided higher thermal stability to the composites due to its platelet structure forming a better barrier to volatiles.

Acknowledgements

Zynab Al-Hassany acknowledges the award of a scholarship from the Co-operative Research Centre for Polymers.

References

[1] Camino G., Maffezzoli A., Braglia M., De Lazzaro M., Zammarano M.: Effect of hydroxides and hydroxycarbonate structure on fire retardant effectiveness and mechanical properties in ethylene-vinyl acetate copolymer. Polymer Degradation and Stability, **74**, 457–464 (2001).
DOI: 10.1016/S0141-3910(01)00167-7

[2] Marosi G. J.: Fire retardancy of polymers: Challenges and new concepts. Express Polymer Letters, **1**, 545 (2007).
DOI: 10.3144/expresspolymlett.2007.77

[3] Costa L., Avataneo M., Bracco P., Brunella V.: Char formation in polyvinyl polymers I. Polyvinyl acetate. Polymer Degradation and Stability, **77**, 503–510 (2002).
DOI: 10.1016/S0141-3910(02)00108-8

[4] Fu M., Qu B.: Synergistic flame retardant mechanism of fumed silica in ethylene-vinyl acetate/magnesium hydroxide blends. Polymer Degradation Stability, **85**, 633–639 (2004).
DOI: 10.1016/j.polymdegradstab.2004.03.002

[5] Touré B., Lopez Cuesta J-M., Longerey M., Crespy A.: Incorporation of natural flame retardant fillers in an ethylene-propylene copolymer, in combination with a halogen-antimony system. Polymer Degradation and Stability, **54**, 345–352 (1996).
DOI: 10.1016/S0141-3910(96)00061-4

[6] Dvir H., Gottlieb M., Daren S., Tartakovsky E.: Optimization of a flame-retarded polypropylene composite. Composites Science and Technology, **63**, 1865–1875 (2003).
DOI: 10.1016/S0266-3538(03)00170-2

[7] Gibert J. P., Lopez Cuesta J-M., Bergeret A., Crespy A.: Study of the degradation of fire-retarded PP/PE copolymers using DTA/TGA coupled with FTIR. Polymer Degradation and Stability, **67**, 437–447 (2000).
DOI: 10.1016/S0141-3910(99)00142-1

[8] Varma I. K., Sadhir R. K.: Thermal degradation of poly(vinyl acetate) in solution. Angewandte Makromolekulare Chemie, **46**, 11–21 (1975).
DOI: 10.1002/apmc.1975.050460102

[9] Zhang Z., Zhang J., Wang Y.: Modeling study on the combustion of intumescent fire-retardant polypropylene. Express Polymer Letters, **1**, 157–165 (2007).
DOI: 10.3144/expresspolymlett.2007.25

[10] Marosi G., Márton A., Anna P., Bertalan G., Marosfői B., Szép A.: Ceramic precursor in flame retardant systems. Polymer Degradation and Stability, **77**, 259–265 (2002).
DOI: 10.1016/S0141-3910(02)00057-5

[11] Shen K. K.: Zinc borate as a flame retardant in halogen-free wire and cable systems. Plastics Compounding, **11**, 26–34 (1988).

[12] Marosi G., Anna P., Bertalan G., Szabó S., Ravadits I., Papp J.: Role of interface modification in flame-retarded multiphase polyolefin systems. in 'Fire and polymers' (eds.: Nelson G., Wilkie C.) ACS Symposium Series, Washington, 161–171 (2001).

[13] Keszei S., Matkó S., Bertalan G., Anna P., Marosi G., Tóth A.: Progress in interface modifications: From compatibilization to adaptive and smart interphases. European Polymer Journal, **41**, 697–705 (2005).
DOI: 10.1016/j.eurpolymj.2004.10.039

[14] Marosfői B. B., Marosi G. J., Szép A., Anna P., Keszei S., Nagy B. J., Martvonova H., Sajó I. E.: Complex activity of clay and CNT particles in flame retarded EVA copolymer. Polymers for Advanced Technologies, **17**, 255–262 (2006).
DOI: 10.1002/pat.691

[15] Szép A., Szabó A., Tóth N., Anna P., Marosi G.: Role of montmorillonite in flame retardancy of ethylene vinyl acetate copolymer. Polymer Degradation and Stability, **91**, 593–599 (2006).
DOI: 10.1016/j.polymdegradstab.2005.02.026

[16] McNeill I. C., Ahmed S., Memetea L.: Thermal degradation of vinyl acetate-methacrylic acid copolymer and homopolymers. I. An FTIR spectroscopic investigation of structural changes in the degrading material. Polymer Degradation Stability, **47**, 423–433 (1995).
DOI: 10.1016/0141-3910(95)00001-1

[17] Holland B. J., Hay J. N.: The thermal degradation of poly(vinyl acetate) measured by thermal analysis-Fourier transform infrared spectroscopy. Polymer, **43**, 2207–2211 (2002).
DOI: 10.1016/S0032-3861(02)00038-1

[18] Clerc L., Ferry L., Leroy E., Lopez-Cuesta J-M.: Influence of talc physical properties on the fire retarding behaviour of (ethylene-vinyl acetate copolymer/magnesium hydroxide/talc) composites. Polymer Degradation and Stability, **88**, 504–511 (2005).
DOI: 10.1016/j.polymdegradstab.2004.12.010

[19] Yu J. C., Xu A., Zhang L., Song R., Wu L.: Synthesis and characterization of porous magnesium hydroxide and oxide nanoplates. Journal of Physical Chemistry B, **108**, 64–70 (2004).
DOI: 10.1021/jp035340w

[20] Braun U., Schartel B.: Flame retardant mechanisms of red phosphorus and magnesium hydroxide in high impact polystyrene. Macromolecular Chemistry and Physics, **205**, 2185–2196 (2004).
DOI: 10.1002/macp.200400255

[21] Huang H., Tian M., Liu L., He Z., Chen Z., Zhang L.: Effects of silicon additive as synergists of $Mg(OH)_2$ on the flammability of ethylene vinyl acetate copolymer. Journal of Applied Polymer Science, **99**, 3203–3209 (2006).
DOI: 10.1002/app.22494

[22] Montezin F., Lopez Cuesta J-M., Crespy A., Georlette P.: Flame retardant and mechanical properties of a copolymer PP/PE containing brominated compounds/antimony trioxide blends and magnesium hydroxide or talc. Fire and Materials, **21**, 245–252 (1997).
DOI: 10.1002/(SICI)1099-1018(199711/12)21:6<245::AID-FAM616>3.0.CO;2-F

[23] Sivalingam G., Madras G.: Thermal degradation of ternary blends of poly(ε-caprolactone)/poly(vinyl acetate)/poly(vinyl chloride). Journal of Applied Polymer Science, **93**, 1378–1383 (2004).
DOI: 10.1002/app.20587

[24] Shen K. K.: Zinc borates: 30 years of successful development as multifunctional fire retardants. in 'Fire and polymers' (eds.: Nelson G. L. and Wilkie C. A.) American Chemical Society, Washington, **18**, 228–239 (2001).
DOI: 10.1021/bk-2001-0797.ch018

[25] Carpentier F., Bourbigot S., Le Bras M., Delobel R., Foulon M.: Charring of fire retarded ethylene-vinyl acetate copolymer-magnesium hydroxide/zinc borate formulations. Polymer Degradation and Stability, **69**, 83–92 (2000).
DOI: 10.1016/S0141-3910(00)00044-6

[26] Genovese A., Shanks R. A.: Structural and thermal interpretation of the synergy and interactions between the fire retardants magnesium hydroxide and zinc borate. Polymer Degradation and Stability, **92**, 2–13 (2007).
DOI: 10.1016/j.polymdegradstab.2006.10.006

[27] Durin-Frances A., Ferry L., Cuesta J. M. L., Crespy A.: Magnesium hydroxide/zinc borate/talc compositions as flame-retardants in EVA copolymer. Polymer International, **49**, 1101–1105 (2000).
DOI: 10.1002/1097-0126(200010)49:10<1101::AID-PI523>3.0.CO;2-5

[28] Karthikeyan B., Mohan S., Baesso M. L.: Spectroscopic and glass transition studies on Nd^{3+}-doped sodium zinc borate glasses. Physica B: Condensed Matter, **337**, 249–254 (2003).
DOI: 10.1016/S0921-4526(03)00411-3

[29] Chang J. B., Yan P. X., Yang Q.: Formation of borate zinc (ZnB_4O_7) nanotubes. Journal of Crystal Growth, **286**, 184–187 (2006).
DOI: 10.1016/j.jcrysgro.2005.10.004

[30] Mel'gunov M. S., Fenelonov V. B., Mel'gunova E. A., Bedilo A. F., Klabunde K. J.: Textural changes during topochemical decomposition of nanocrystalline $Mg(OH)_2$ to MgO. Journal of Physical Chemistry B, **107**, 2427–2434 (2003).
DOI: 10.1021/jp021474i

[31] Bourbigot S., Carpentier F., Le Bras M.: Thermal degradation and combustion mechanism of FR EVA. ACS Polymeric Materials: Science and Engineering. Fall Meeting, Washington USA, Vol **83**, 68–69 (2000).

[32] García-Martinez J. M., Laguna O., Areso S., Collar E. P.: A dynamic-mechanical study of the role of succinyl-fluorescein grafted atactic polypropylene as interfacial modifier in polypropylene/talc composites. Effect of grafting degree. European Polymer Journal, **38**, 1583–1589 (2002).
DOI: 10.1016/S0014-3057(02)00051-4

[33] Chiem L. T., Huynh L., Ralston J., Beattie D. A.: An in situ ATR-FTIR study of polyacrylamide adsorption at the talc surface. Journal of Colloid and Interface Science, **297**, 54–61 (2006).
DOI: 10.1016/j.jcis.2005.10.037

[34] Malandrini H., Clauss F., Partyka S., Douillardt J. M.: Interactions between talc particles and water and organic solvents. Journal of Colloid and Interface Science, **194**, 183–193 (1997).
DOI: 10.1006/jcis.1997.5103

[35] Sain M., Park S. H., Suhara F., Law S.: Flame retardant and mechanical properties of natural fibre-PP composites containing magnesium hydroxide. Polymer Degradation and Stability, **83**, 363–367 (2004).
DOI: 10.1016/S0141-3910(03)00280-5

[36] Alexander G., Cheng Y-B., Burford R. P., Shanks R. A., Mansouri J., Barber K. W., Rodrigo P. D. D., Preston C. M. L.: Ceramifying composition for fire protection. World Patent, WO 2005/095545 (2005).

eXPRESS Polymer Letters Vol.4, No.2 (2010) 94–100
Available online at www.expresspolymlett.com
DOI: 10.3144/expresspolymlett.2010.14

Ethylene-hexene copolymer derived from [t-butylfluorenylsilyl-amido] dimethyl titanium complex

E. Chaichana[1], *S. Khaubunsongserm*[2], *P. Praserthdam*[1], *B. Jongsomjit*[1*]

[1]Center of Excellence on Catalysis and Catalytic Reaction Engineering, Department of Chemical Engineering, Faculty of Engineering, Chulalongkorn University, Bangkok 10330, Thailand
[2]PTT Public Company Limited, PTT Research and Technology Institute, Wangnoi, Ayuthaya 13170, Thailand

Received 15 September 2009; accepted in revised form 16 November 2009

Abstract. The copolymers of ethylene and 1-hexene were prepared with half-metallocene titanium complex ([t-BuNSiMe$_2$Flu]TiMe$_2$) and modified methylaluminoxane (MMAO). The initial concentrations of 1-hexene were varied to investigate how the different amounts of comonomer affect on the catalytic activity of copolymerization system and microstructure of the copolymers. It has been found that this catalytic system was not active for hexene polymerization, however, it can be active when ethylene was introduced to perform ethylene-hexene copolymerization. As comonomer, 1-hexene provides positive comonomer effect on the system although very high concentration of 1-hexene was introduced. However, the microstructures of the obtained copolymers, which were examined by ^{13}C-NMR need to be improved because with highly alternating sequence distribution of comonomer causing them losing some essential specific thermal properties.

Keywords: *polymer synthesis, molecular engineering, metallocene, copolymer, LLDPE*

1. Introduction

It is generally presumed that crystallinity of polymer plays an important role in determining the polymer properties, such as mechanical and thermal properties [1, 2]. We have known that, in synthesis of linear low-density polyethylene (LLDPE) by copolymerization of ethylene with α-olefins, the crystallinity depends mainly on the amount of α-olefin (comonomer) content in copolymer [3]. So, if the comonomer content can be controlled, properties of copolymer can be also altered. Appropriate crystallinity or comonomer content is varied depending on the application of polymer. The high comonomer content of copolymer has been commercially produced, named plastomers [1]. The advantages of plastomers are low density, high elongation, and low haze in film form. In order to obtain the plastomer derived from the metallocene catalysts, the open structure of metallocene catalyst is crucial. Half-metallocenes and/or constrained geometry catalysts (CGCs) are subset of general metallocene catalyst , which pose the open structure because they have just one cyclopentadienyl ring (or their family, such as, indenyl or fluorenyl rings) bonded with the group IV transition metal leaving the opposite side of that ring large enough space for comonomer incorporation with less hindrance [4]. Therefore, plastomers or LLDPE with high comonomer content can be obtained with this type of catalyst.

As mentioned, comonomer contents are sensitive to many factors, such as the structure of catalyst, type of catalyst activators and the initial concentration of comonomer in the system. When considering the initial concentration, it has been found that the initial comonomer concentration not only affects

*Corresponding author, e-mail: bunjerd.j@chula.ac.th

directly on the comonomer contents, but it also affects on the catalytic activity of system [5, 6]. Therefore, in this present study the effect of the initial comonomer concentration in ethylene-1-hexene copolymerization with half-metallocene is investigated to determine both the catalytic performance and the specification of the obtained copolymers.

2. Experimental

2.1. Materials

All operations were manipulated under an argon atmosphere using glove box and/or standard Schlenk techniques. The [t-BuNSiMe$_2$Flu]TiMe$_2$ (Ti-complex) was synthesized according to the procedure described by Hagihara *et al*. [7]. Ethylene (polymerization grade) was obtained from the National Petrochemical Co. Ltd., Thailand. 1-Hexene (≥ 97%) was purchased from Aldrich Chemical Company, Thailand and further purified by distilling over CaH_2 for 6 h. Modified methyl aluminoxane, MMAO [(Me–Al–O–)$_m$-(i–Bu–Al–O–)$_n$] having 1.86 M in toluene, was donated by Tosoh Akzo, Japan. Toluene (commercial grade) was donated by the Exxon Chemical, Thailand Co. Ltd. It was dried over dehydrated $CaCl_2$ and distilled over sodium/benzophenone.

2.2. Polymerization procedure

Ethylene/1-hexene copolymerization reaction was carried out in a 100 ml semibatch stainless steel autoclave reactor equipped with a magnetic stirrer. At first, the desired amounts of MMAO and the toluene were introduced into the reactor. The titanium complex in toluene (10 μmol·ml^{-1}) was put into the reactor to make the $[Al]_{MMAO}/[Ti]_{cat} = 400$. Then, the reactor was immersed in liquid nitrogen. 1-hexene was added into the frozen reactor (to stop or prevent possible polymerization of 1-hexene). The reactor was heated up to the polymerization temperature at 343 K. The polymerization was started by feeding ethylene (0.018 moles) into the reactor. The ethylene pressure and reactor temperature were kept constant during the polymerization (pressure in reactor = 349 kPa (50 psi)). Due to the fixed ethylene consumption (at 0.018 moles), the polymerization time was defined as the time that all ethylene gas was totally consumed (the equivalent pressure drop of 42 kPa (6 psi) was observed). The polymerization time was recorded to calculate the activity. The reaction was terminated by adding acidic methanol and the material was stirred for 30 min. After filtration, the copolymer obtained was washed with methanol and dried at room temperature.

2.3. ^{13}C-NMR spectroscopy

^{13}C-NMR spectroscopy was used to determine the α-olefin incorporation and copolymer microstructure. Chemical shifts were referenced internally to the $CDCl_3$ and calculated according to the method described by Randall [8]. Each sample solution was prepared by dissolving 50 mg of copolymer in 1,2,4-trichlorobenzene and $CDCl_3$. ^{13}C-NMR spectra were taken at 333 K using a BRUKER AVANCE II 400 operating at 100 MHz with an acquisition time of 1.5 s and a delay time of 4 s.

2.4. Differential scanning calorimetry

The melting temperature of ethylene/1-octene copolymer products was determined with a Perkin-Elmer diamond DSC. The analyses were performed at the heating rate of 20°C/min in the temperature range of 50–150°C. The heating cycle was run twice. In the first scan, samples were heated, and then cooled to room temperature. In the second scan, samples were reheated at the same rate, but only the results of the second scan were reported because the first scan was influenced by the mechanical and thermal history of samples.

3. Results and discussion

3.1. Reactivity of (co)monomer to catalyst

The catalytic activities based on polymer product are shown in Table 1. It can be seen that there is no catalytic activity for system conducted with only 1-hexene as monomer (**entry 1**). The opposite occurred on **entry 2** for the system that used only ethylene as monomer. It suggests that this half-metallocene catalyst ([t-BuNSiMe$_2$Flu]TiMe$_2$) is active for ethylene polymerization, but not for 1-hexene polymerization. This result agreed with the finding of Intaragamjon *et al*. [9], who reported that this catalyst cannot proceed 1-hexene polymerization under the specified condition. It has been known that ethylene is the most reactive olefin

Table 1. Activities of system with various monomer concentrations

Entry	Ethylene[a] [mol/l]	1-Hexene [mol/l]	Time [s]	Weight [g]	Activity[b] (kg polymer/mol Ti .h)
1	0.0	0.6	475	–	–
2	0.6	0.0	475	0.2468	187
3	0.6	0.3	500	1.0596	763
4	0.6	0.6	248	1.4030	2037
5	0.6	1.2	326	1.9241	2125

[a]Ethylene addition into the system
[b]Copolymerization condition: Ti = 10 μmol, Al/Ti = 400, temperature = 343 K, 349 kPa (50 psi) of ethylene pressure was applied

[10], so it can react with itself for polymerization in the absence of any comonomer. Although 1-hexene was not reactive in its homopolymerization, it can be reacted in the system of copolymerization with ethylene (**entry 3–5**). Thus, this should be clarified in this finding that why 1-hexene was not active unless ethylene was introduced together in the system, even with the small amount of ethylene as seen for **entry 5**.

The mechanism of polymerization by metallocene catalyst system is reviewed here to explain the result. There are three main steps for completing the copolymerization (excluding chain transfer step), as shown in Figure 1 [10]. The first step is the 'activation' of metallocene catalyst typically achieving via contact with an appropriate cocatalyst species (MMAO in this case). The second is the 'initiation' of the polymerization occurring as a result of the displacement of the anion and coordination of the monomer in the primary complex. In our study, this step seems to be a problem for obtaining the 1-hexene polymerization, since the ion-pairs still stay in their coordinated tightly. Therefore, only the strong reactive monomer like ethylene is able to insert in this coordination, and consequently displace the anion and make coordination with catalyst active site. This step can generate an available coordination site on the metal center, which provides high enough space for a large molecule, such as 1-hexene to coordinate with it in the next step. As the result, the final step that is the 'propagation' step will be the open competition between ethylene monomer and 1-hexene comonemer for insertion into the growing chain of polymer.

As describe above, for this catalytic system, if ethylene was not introduced into the system first, 1-hexene would not be reactive for this half-metallocene catalyst even open structure. However, in many cases, 1-hexene can perform polymerization by itself with some metallocenes such as iPr(Cp)(Flu)$ZrCl_2$ and En(Ind)$_2ZrCl_2$ [11] indicating that reactivities of α-olefin also depend on the catalyst structure [12].

3.2. Effect of the amount of 1-hexene on catalytic activity

In **entry 3–5**, introducing of 1-hexene into copolymerization enhanced catalytic activity higher than

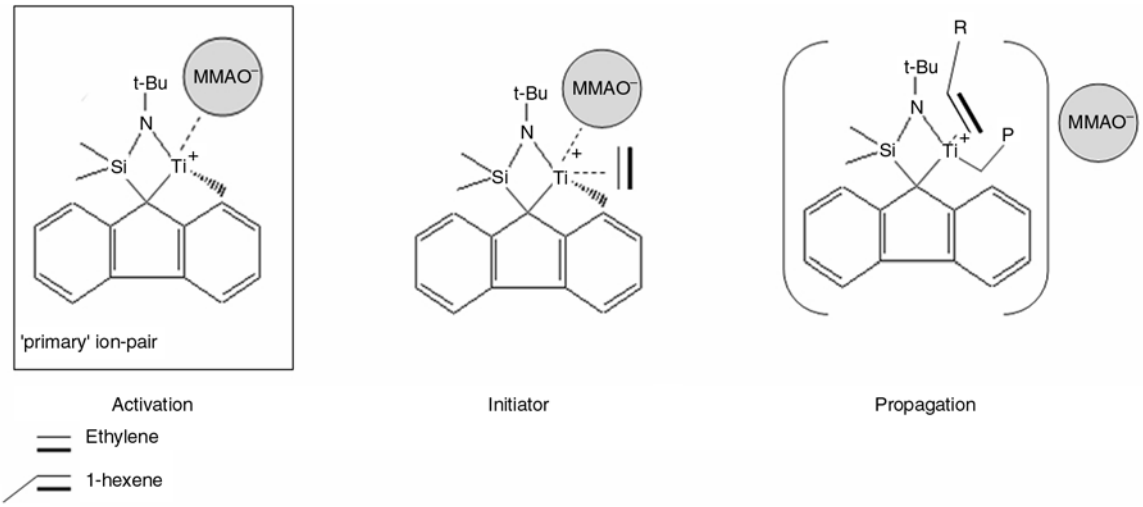

Figure 1. Schematic representation of copolymerization mechanism

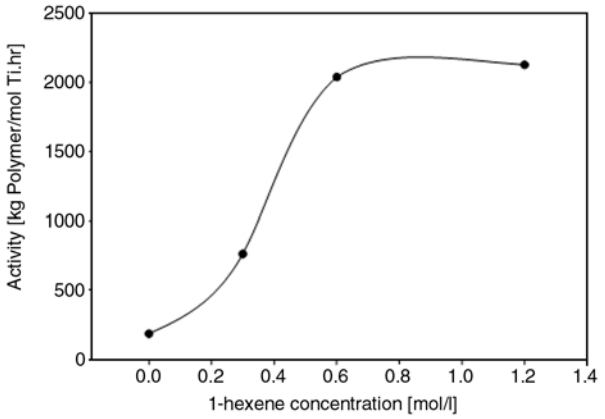

Figure 2. Activity profile with various 1-hexene concentrations

that of system without 1-hexene (**entry 2**). When the amounts of 1-hexene were increased, the catalytic activities were also increased. They increased pronouncedly when the amount of 1-hexene was raised from 0.3 to 0.6 mol/l. However, they gradually increased when the amount of 1-hexene was raised two times again from 0.6 to 1.2 mol/l. A comparison of activities is also shown in Figure 2. It can be explained that the first range of increasing is because of comonomer effect in copolymerization behavior [13]. The chain structure of 1-hexene can increase the gap between the cationic active species and counter anion more separately in propagation step (Figure 1). Then, the propagation rate of polymerization can be raised leading to enhancing the activity of copolymerization. However, at 1.2 mol/l of 1-hexene concentration (**entry 5**), the anticipated activity can not be attained. This is because high excess of 1-hexene obstructed active sites of catalyst from reacting with ethylene monomer, and consequently reduce rate of ethylene insertion into the chain of growing polymer. The explanation can be supported by polymerization time of **entry 5**, which was longer than that of **entry 4**. The longer polymerization time suggests that, in **entry 5**, the rate of ethylene consumption for polymerization was slower than that of **entry 4**. Although the rate of ethylene consumption in **entry 4** was faster, activity or productivity of **entry 5** was higher. This is because initial concentration of 1-hexene of **entry 5** was higher then it can produce more product than **entry 4** did resulting in high catalytic activity for the system.

3.3. Effect of the amount of 1-hexene on microstructure of copolymers

As seen in Table 2, the comonomer incorporations apparently increased with increasing the amount of 1-hexene in copolymerization. In this copolymerization process, which fixed the amount of ethylene addition and kept ethylene pressure constant during copolymerization, the incorporation of 1-hexene can be increased by two primary reasons. One is that enhancing the reactivity of 1-hexene or two, diminishing the reactivity of ethylene. It can be seen from Table 2 that reactivities of ethylene decreased dramatically with increasing the concentration of 1-hexene in the system while reactivities of 1-hexene just slightly increased. So, it can be concluded that the initial concentrations of 1-hexene in the system have more effect on the reactivity of ethylene than itself. The increase of 1-hexene reactivity enables it to still incorporate continuously into the growing chain even at high concentration. The open structure of half-metallocene catalyst is one of the important factors that retains high reactivity of 1-hexene and encourages high comonomer incorporation. As compared with the works done by our group previously with normal metallocene, it has been found that with the same initial comonomer concentration in copolymerization, the obtained copolymer from those studies exhibited much lower comonomer incorporation than in this study [14, 15].

On account of the fact that the uniform comonomer incorporation is the key feature for producing low-density plastomer, which exhibited plastic and elas-

Table 2. Comonomer incorporation and the reactivity ratios

Entry	Ethylene [mol/l]	1-Hexene [mol/l]	Incorporation[a]		Reactivity[b]		
			E [mol%]	H [mol%]	r_E	r_H	$r_E r_H$
3	0.6	0.3	68.4	31.6	1.121	0.658	0.737
4	0.6	0.6	43.7	56.3	0.797	0.738	0.588
5	0.6	1.2	23.0	77.0	0.621	0.784	0.487

[a]Examined by ^{13}C-NMR by Randall method [8]

[b]Relative comonomer reactivities (r_E for ethylene and r_H for 1-hexene) calculated by r_E = 2[EE]/[EC]X, r_H = 2X[CC]/[EC], [EE] = [EEE] + 0.5[CEE], [CC] = [CCC] + 0.5[ECC], [EC] = [CEC] + 0.5[CEE] + [ECE] + 0.5[ECC]

Table 3. Triad distribution of copolymer obtained from ^{13}C-NMR

Entry	Ethylene [mol/l]	1-Hexene [mol/l]	EEE	EEH	HEH	EHE	EHH	HHH
3	0.6	0.3	0.345	0.292	0.048	0.172	0.144	0.000
4	0.6	0.6	0.091	0.270	0.076	0.185	0.339	0.039
5	0.6	1.2	0.015	0.130	0.085	0.154	0.424	0.192

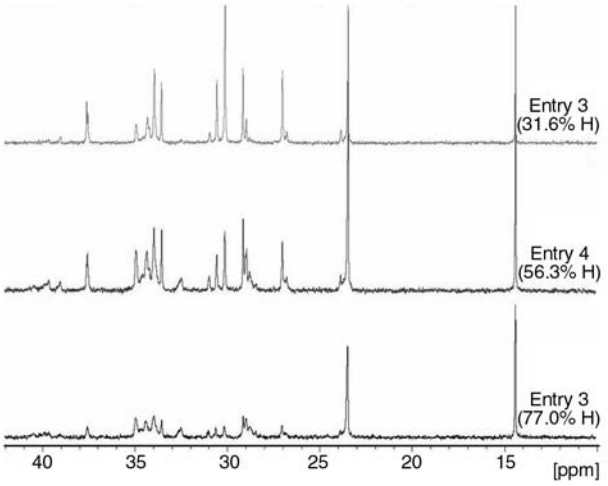

Figure 3. ^{13}C-NMR spectra of copolymers

tomeric behavior [16], the distribution of comonomer in the copolymers needs to be concerned in order to obtain plastomers with desired specification. The triad distribution for all copolymers obtained from ^{13}C-NMR is shown in Table 3. Triad block of comonomer (HHH) was detected in samples having 1-hexene incorporation above 31.6% (**entry 4, 5**). It was also noticed from Figure 3, which showed ^{13}C-NMR spectrum of the copolymers that the peaks between 39.5 and 42 ppm (proportional to the HHH triad) occurred obviously in the copolymer from **entry 4** and **5**. Nevertheless, the number of HHH triad was not converted directly from the area under these peaks. There are other peaks, which are more pronounced in the calculation. Therefore, the larger area of these peaks of **entry 4** than **entry 5** did not mean that **entry 4** had more HHH triad than **entry 5**.

The presence of HHH triad can imply that the good distribution of comonomer throughout the copolymer chain was interrupted at high incorporation of comonomer. Although the copolymers with high 1-hexene incorporation contain the block of comonomer, they are still not the block copolymer. It can be observed from the product of reactivity ratio ($r_E r_H$), which is one of the parameters that can identify types of copolymer. A value $r_E r_H > 1$ indicates a block copolymer structure and $r_E r_H < 1$ reveals an alternating copolymer structure. Therefore, all the obtained copolymers are alternating copolymers having the $r_E r_H$ value being lower than 1. Once the alternating copolymers were obtained, it means the comonomers in their chain are distributed moderately well along the backbone, then shortening the average backbone sequence length for crystallization and therefore low crystallinity, including low density, would be gained. Thus, with these properties, the obtained copolymers are in closing proximately to be low-density plastomer. However, these copolymers might not meet all properties required for the use in plastic industry because they probably lost completely the thermal properties.

As a result of the fact that disadvantages of alternating copolymer, which have been found by Hung *et al*. [17] that the polymer with a highly alternating sequence distribution did not exhibit any melting behavior. Based on the result, when the incorporations of comonomers increased, the obtained polymer tended to exhibit more highly alternating copolymer structure ($r_E r_H < 1$). Therefore, they might lose the melting behavior at high level of 1-hexene incorporation. To prove that, melting temperatures of the obtained polymers were investigated by differential scanning calorimetry (DSC). From the investigation, it was found that only the sample from **entry 2**, which is the polyethylene sample, has the melting temperature (130°C) and the remaining samples cannot be found the melting temperatures. Thus, the losses of thermal properties existed in all obtained copolymers even the one that had low comonomer content (**entry 3**, 31.6%).

Copolymers were formed the gel-like structure as seen in Figure 4 when the 1-hexene was introduced into the system, especially at the high level of incorporation. With this structure, it is obviously shown the character of amorphous material. Therefore, it accords with the results from ^{13}C-NMR and DSC that the obtained copolymers should not have the melting temperature.

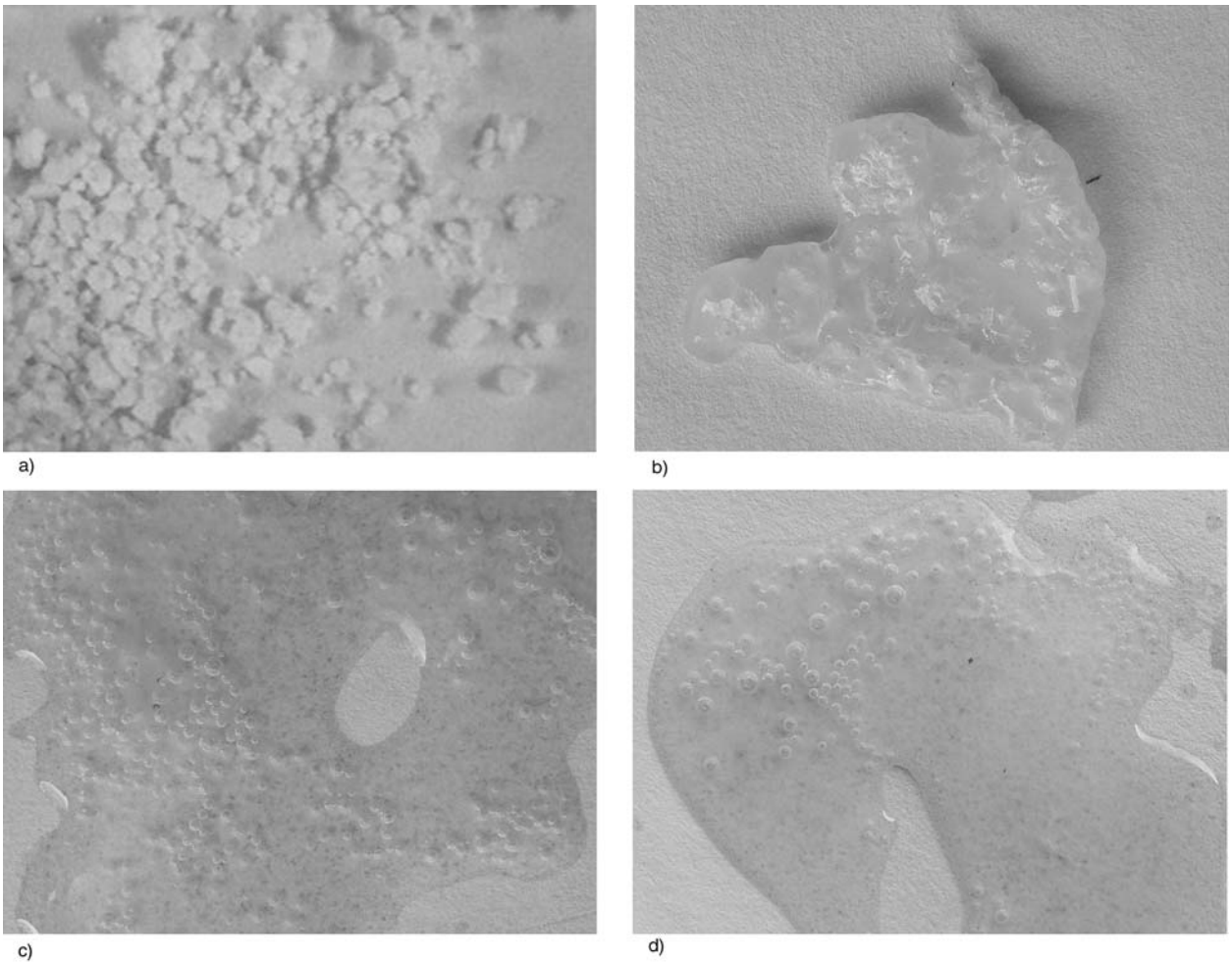

Figure 4. Digital photograph of copolymer with various 1-hexene contents a) 0%, b) 31.6%, c) 56.3% and d) 77.0%

4. Conclusions

It was found that the positive comonomer effect occurred even though a very high concentration of 1-hexene that was introduced into the system. However, the microstructures of the obtained copolymer examined by ^{13}C-NMR need to be improved because the highly alternating sequence distributions of copolymer cause the loss of essential specific thermal properties.

Acknowledgements

We thank the Thailand Research Fund (TRF), the Commission of Higher Education (CHE) of Thailand and PTT Research and Technology Institute for the financial support of this project.

References

[1] Speed C. S., Trudell B. C., Mehta A. K., Stehling F. C.: Structure/property relationships in EXPOL™ polymers. in 'Society of plastics engineers polyolefins, VII International conference, Houston, Texas' 45–66 (1991).

[2] Jongsomjit B., Chaichana E., Praserthdam P.: LLDPE/nano-silica composites synthesized via in situ polymerization of ethylene/1-hexene with MAO/metallocene catalyst. Journal of Material Science, **40**, 2043–2045 (2005).
DOI: 10.1007/s10853-005-1229-z

[3] Hong H., Zhang Z., Chung T. C. M., Lee R. W.: Synthesis of new 1-decene-based LLDPE resins and comparison with the corresponding 1-octene- and 1-hexene-based LLDPE resins. Journal of Polymer Science Part A: Polymer Chemistry, **45**, 639–649 (2007).
DOI: 10.1002/pola.21825

[4] Kaminsky W., Tran P-D., Weingarten U.: New materials by polymerisation of olefins and styrene with metallocene catalysts. Macromolecular Symposia, **193**, 1–11 (2003).
DOI: 10.1002/masy.200390053

[5] van Grieken R., Carrero A., Suarez I., Paredes B.: Effect of 1-hexene comonomer on polyethylene particle growth and kinetic profiles. Macromolecular Symposia, **259**, 243–252 (2007).
DOI: 10.1002/masy.200751329

[6] Galland G. B., Seferin M., Mauler R. S., Dos Santos J. H. Z.: Linear low-density polyethylene synthesis promoted by homogeneous and supported catalysts. Polymer International, **48**, 660–664 (1999).
DOI: 10.1002/(SICI)1097-0126(199908)48:8<660::AID-PI212>3.0.CO;2-L

[7] Hagihara H., Shiono T., Ikeda T.: Living polymerization of propene and 1-hexene with the [*t*-BuNSiMe$_2$Flu]TiMe$_2$/B(C$_6$F$_5$)$_3$ catalyst. Macromolecules, **31**, 3184–3188 (1998).
DOI: 10.1021/ma971697k

[8] Randall J. C.: A review of high resolution liquid 13carbon nuclear magnetic resonance characterizations of ethylene-based polymers. Polymer Reviews, **29**, 201–317 (1989).
DOI: 10.1080/07366578908055172

[9] Intaragamjon N., Shiono T., Jongsomjit B., Praserthdam P.: Elucidation of solvent effects on the catalytic behaviors for [*t*-BuNSiMe$_2$Flu]TiMe$_2$ complex during ethylene/1-hexene copolymerization. Catalysis Communications, **7**, 721–727 (2006).
DOI: 10.1016/j.catcom.2006.02.022

[10] Severn J. R., Chadwick J. C.: Tailor-made polymers: Via immobilization of alpha-olefin polymerization catalysts. Wiley-VCH, Weinheim (2008).

[11] Kawahara N., Saito J., Matsuo S., Kaneko H., Matsugi T., Toda Y., Kashiwa N.: Study on unsaturated structures of polyhexene, poly(4-methylpentene) and poly(3-methylpentene) prepared with metallocene catalysts. Polymer, **48**, 425–428 (2007).
DOI: 10.1016/j.polymer.2006.11.001

[12] Krenstel B. A., Kissin Y. V., Kleiner V. J., Stotskaya L. L.: Polymer and copolymer of higher α-olefins. Hanser Publishers, Munich (1997).

[13] Forlini F., Fan Z-Q., Tritto I., Locatelli P., Sacchi M. C.: Metallocene-catalyzed propene/1-hexene copolymerization: Influence of amount and bulkiness of cocatalyst and of solvent polarity. Macromolecular Chemistry and Physics, **198**, 2397–2408 (1997).
DOI: 10.1002/macp.1997.021980804

[14] Jongsomjit B., Ngamposri S., Praserthdam P.: Application of silica/titania mixed oxide supported zirconocene catalyst for synthesis of linear low-density polyethylene. Industrial and Engineering Chemistry Research, **44**, 9059–9063 (2005).
DOI: 10.1021/ie050806d

[15] Bunchongturakarn S., Jongsomjit B., Praserthdam P.: Impact of bimodal pore MCM-41-supported zirconocene/dMMAO catalyst on copolymerization of ethylene/1-octene. Catalysis Communications, **9**, 789–795 (2008).
DOI: 10.1016/j.catcom.2007.09.001

[16] Yu T. C.: Metallocene plastomer modification of polypropylenes. Polymer Engineering and Science, **41**, 656–671 (2001).
DOI: 10.1002/pen.10761

[17] Hung J., Cole A. P., Waymouth R. M.: Control of sequence distribution of ethylene copolymers: Influence of comonomer sequence on the melting behavior of ethylene copolymers. Macromolecules, **36**, 2454–2463 (2003).
DOI: 10.1021/ma021779v

eXPRESS Polymer Letters Vol.4, No.2 (2010) 101–114
Available online at www.expresspolymlett.com
DOI: 10.3144/expresspolymlett.2010.15

The effect of molecular mass on the polymorphism and crystalline structure of isotactic polypropylene

Zs. Horváth[1], *I. E. Sajó*[2], *K. Stoll*[3], *A. Menyhárd*[1,4], *J. Varga*[1]

[1]Budapest University of Technology and Economics, Department of Physical Chemistry and Materials Science, P. O. Box 91, H-1521 Budapest, Hungary
[2]Hungarian Academy of Sciences, Chemical Research Centre, Institute of Nanochemistry and Catalysis, P. O. Box 17, H-1525 Budapest, Hungary
[3]CIBA Inc, Schwarzwaldallee 215, CH-4002 Basel, Switzerland
[4]Hungarian Academy of Sciences, Chemical Research Centre, Institute of Materials and Environmental Chemistry, P. O. Box 17, H-1525 Budapest, Hungary

Received 5 May 2009; accepted in revised form 5 December 2009

Abstract. This study is devoted to the investigation of the effect of molecular mass on the α-, β- and γ-crystallization tendency of isotactic polypropylene (iPP). The crystalline structure was studied by wide angle X-ray scattering (WAXS) and by polarised light microscopy (PLM). The melting and crystallization characteristics were determined by differential scanning calorimetry (DSC). The results indicate clearly that iPP with low molecular mass crystallizes essentially in α-modification. However, it crystallizes in β-form in the presence of a highly efficient and selective β-nucleating agent. The α- and β-modifications form in wide molecular mass range. The decreasing molecular mass results in increased structural instability in both α- and β-modifications and consequently enhanced inclination to recrystallization during heating. The formation of γ-modification could not be observed, although some literature sources report that γ-form develops in iPP with low molecular mass.

Keywords: *thermal properties, isotactic polypropylene, low molecular mass, crystallization tendency, polymorphism*

1. Introduction

Semicrystalline isotactic polypropylene (iPP) is a commodity polymer produced and applied in large quantity nowadays. Semicrystalline iPP is a polymorphic material, with several crystalline modifications including the monoclinic (α), the trigonal (β), and the orthorhombic (γ) forms [1–4]. iPP crystallizes essentially into α-modification under traditional processing conditions. The α-form is the thermodynamically stable form according to the literature [1, 3, 4]. The modification of the crystalline structure of iPP by introduction of nucleating agents is one of the keys of its wide scale application fields.

The β-form of iPP (β-iPP) can be prepared by adding β-nucleating agents in the industrial practice [4]. Several efficient and selective β-nucleating agents are known in the literature [4–13]. However, more or less α-iPP is always formed in their presence [5, 7–10]. The pure β-form of iPP was prepared by Varga *et al*. [11] by the introduction of Ca-salt of suberic or pimelic acids. Recently, Zhang *et al*. [12, 13] used pimelic acid supported nano-sized $CaCO_3$ as β-nucleating agent. β-iPP has several advantageous properties compared to the traditional α-form, like higher impact resistance, ductility and better weldability [4, 14, 15]. The high impact resistance of β-form resulted in increased

*Corresponding author, e-mail: amenyhard@mail.bme.hu

industrial interest in the past decades and simultaneously the number of available β-nucleating agents increased as well.

The early studies revealed that iPP with low molecular mass (M_w < 6000 g/mol) results in the formation of samples rich in γ-iPP [16–18]. The effect of molecular mass on the crystalline morphology in non-nucleated and β-nucleated peroxide degraded iPP has been studied by Wang *et al*. [19]. However, they carried out studies only in a narrow molecular mass range, where no significant changes were observed. Moreover, the effect of βα-recrystallization was not eliminated during their DSC studies in the case of β-nucleated samples. Recently, Chvatalova *et al*. [20] reported a detailed study about the effect of molecular mass on the β-crystallization ability of iPP. They performed their study using commercial iPP grades with different molecular masses and applied a commercial β-nucleating agent.

It was also observed that during the crystallization of degraded iPP samples with enhanced content of γ-form were formed. Vychopnova *et al*. [21] have investigated the effect of photo-degradation on the crystallization tendency of β-nucleated iPP. They found that the crystallization tendency in the β- and α-forms decreases with increasing doses of irradiation, but they have not studied the polymorphic composition by WAXS technique. Therefore, they could not obtain any information about the formation of γ-form. Campbell *et al*. [22] observed that γ-phase forms in high molecular mass iPP at high pressure over 2000 bars as well. The influence of stereo- and regio-defects was observed during the early studies. Therefore, considerable amount of γ-iPP forms during the crystallization of ethylene/propylene random copolymers of propylene (RCPP) [23]. The results of a recent study by Krache *et al*. [24] supports the earlier result that the formation of γ-form is promoted by the stereo- and regio-defects in β-nucleated iPP as well. Juhász *et al*. [25, 26] studied the γ-crystallization tendency of β-nucleated and non-nucleated propylene/1-pentene copolymers and they found that the amount of γ-form increases with increasing of 1-pentene content. Moreover, the γ-crystallization tendency of 1-pentene copolymers was even higher than that of samples containing ethylene or butylene comonomer units. The structural features of γ-iPP was studied by Lotz and his co-workers [2]. They found that γ-modification forms within the α-phase on the lateral surface of α-iPP crystallites (α-γ lamellar branching).

The crystallization tendency and polymorphic composition of low molecular mass iPP and its β-nucleated forms are reported in this study. Our goal was to explore the effect of changing the molecular mass in broad range on the crystallization tendency and the polymorphic composition of iPP.

2. Experimental part

2.1. Materials and sample preparation

A commercial iPP homopolymer with low molecular mass (Licowax PP 230) produced by Clariant and its β-nucleated form was used in the first series of our study. Licowax PP 230 (LICO) is often applied as lubricant and processing aid for high molecular mass iPP grades. The melt viscosity of LICO is very low (η = 1700 mPas at 170°C) indicating low molecular mass.

In order to characterise the effect of molecular mass in broad range on the crystallization behaviour of iPP, peroxide degraded samples were produced from TIPPLEN H-804 neat iPP homopolymer powder (MFR = 0.2 g/10 min at 230°C, 2.16 kg of load) supplied by TVK according to the method of controlled rheology (CR) [19, 27, 28]. During CR processing different amounts of dicumyl-peroxide (Trigonox 101) were introduced into the iPP using a Henschel FM/A10 fluid mixer at 700 min^{-1} of rotating speed for 5 min. The samples were processed in a Brabender DSK 42/7 type compounder driven by a Brabender Plasti-Corder PLE 3000 unit. The temperature zones of the compounder were set to 190, 200, 220, 220°C respectively. After the CR processing the MFR of the samples were measured by CEAST Modul 7027 type equipment at 230°C with load of 2.16 kg. The complete decomposition of dicumyl-peroxyde was controlled by repeated measurements of MFR at 230°C. If the secondly measured MFR value was identical with the first one, we assume that all peroxide was reacted. All samples produced by CR-processing and their designations are included in Table 1. The non-degraded reference material with high molecular mass is H-804, which is designated as CR-0 in the followings.

The molecular mass and its distribution were characterized by gel permeation chromatography

Table 1. The designation of studied non-nucleated and β-nucleated samples processed by controlled rheology

Designation of samples	Trigonox 101 [ppm]	MFR [g/10 min]	Polydispersity
CR-0 β-CR-0	0	0.20	1.83
CR-200 β-CR-200	200	2.64	3.08
CR-300 β-CR-300	300	4.26	2.14
CR-500 β-CR-500	500	11.98	1.99
CR-800 β-CR-800	800	21.14	2.28
CR-1000 β-CR-1000	1000	22.67	2.16
CR-1200 β-CR-1200	1200	35.31	2.16
CR-1600 β-CR-1600	1600	89.08	2.37

(GPC) as well. GPC measurements were carried out using a PL-GPC 210 (Polymer Laboratories Ltd.) equipment according to ISO 16014 standard procedure. The samples were dissolved in 1,2,4-trichloro-benzene (TCB) (1 mg/ml) at 160°C for 2 hours and stabilized by 2,6-di-tert-butyl-4-methylphenol (BHT) (100 mg/l).

1000 ppm of Irganox 1010 as stabilizer and 500 ppm of Ca-stearate as acid scavenger were added to samples processed by CR technology, in order to avoid the further degradation. The calcium salt of suberic acid (Ca-sub), which is a highly efficient and selective β-nucleating agent, was added in 1000 ppm to all β-nucleated blends [11]. The homogenisation of the other additives – like stabilizers, acid scavenger and β-nucleating agent in the case of β-nucleated samples – after CR processing was carried out using a Brabender W50-EH internal mixer at 220°C for 5 min.

Square shaped plaques (40×40 mm) with 1 mm of thickness were produced using a Fontijne hydraulic compression-moulding machine at 2.5 MPa of pressure. The polymer was melted at 220°C for 2 min and cooled down to room temperature slowly or rapidly under constant 2.5 MPa of pressure. In the case of slow cooling the heating of the compression moulding machine was switched off and the mould was cooled spontaneously down to room temperature with a cooling rate of 100°C/h approximately. The rapid cooling means that the mould was cooled by cold water, which results in a cooling rate of 100°C/min approximately.

2.2. Experimental techniques and methods

The structure was investigated by polarised light microscopy (PLM) and by wide angle X-ray scattering (WAXS) techniques. The PLM experiments were carried out using a Zeiss Axioscope microscope equipped by a Leica DFC 320 digital camera. In order to determine of the optical characteristics of the samples studied, a λ-plate was located diagonally between the crossed polarisers. The temperature of the samples was regulated by a Mettler FP 82 HT hot stage. The samples were crystallized under isothermal conditions after the elimination of thermal and mechanical prehistory by holding the samples at T = 220°C for 5 min. The samples were cooled to the crystallization temperature (T_c) at a cooling rate of 5°C/min. X-ray scattering patterns were recorded using a Philips PW 1830/PW type equipment with CuK_α radiation at 40 kV and 35 mA and X Pert PRO MPD type equipment with CuK_α radiation at 40 kV and 30 mA. The k value introduced by Turner Jones *et al*. [29] for characterisation of the β-content was calculated on the basis of the WAXS patterns.

The melting and crystallization characteristics of the samples were studied by calorimetric (DSC) method. The thermal and mechanical prehistory was erased by holding the samples for 5 min at 220°C. Subsequently, the sample was cooled down to room temperature at a cooling rate of 10°C/min and the crystallization curves were recorded. The melting curves were obtained during heating from room temperature to 220°C with a heating rate of 10°C/min. During heating of the β-nucleated samples cooled down to room temperature, βα-recrystallization occurs that results in pronounced peak multiplication [30]. In order to eliminate the disturbing effect of βα-recrystallization, the end temperature of recooling (T_R) was set to T_R = 100°C in the subsequent series of the experiment (second run). According to the melting memory effect of β-iPP discussed in detail in the literature [3, 4, 30], βα-recrystallization does not appear during heating of the samples started from the critical temperature of T_R^* = 100°C. The β-content (β_c) can be estimated exactly from the melting curve of samples registered after limited recooling step [3–5]. The structural stability of the crystals are formed in LICO and β-LICO samples was characterized by melting curves recorded after cooling with different cooling rates (2, 5, 10, 20°C/min). The influence of the heat-

ing rate on the recrystallization was studied in a series of experiments using heating rates of 10, 20, 40, 50 and 60°C/min.

3. Results and discussion

3.1. The crystalline structure of low molecular mass iPP

WAXS patterns of the sample LICO and its β-nucleated form are given in Figure 1. The non-nucleated LICO sample crystallizes essentially in the α-form. The characteristic diffraction peaks corresponding to the α-modification at 2θ of 14° (α_1(110)), 16.5° (α_2(040)) and 18.3° (α_3(130)) respectively can be clearly seen in curve 1 of Figure 1 [17]. Predominantly β-iPP forms in the presence of the highly efficient β-nucleating agent used. The intensive diffraction peak at 2θ = 16° refers to the β-modification (β_1(300)). However, a minor amount of α-iPP is still present in the β-LICO sample (Figure 1 curve 2). The *k*-value of β-LICO sample is 0.81. In contrary to the literature sources, which have reported that γ-modification forms in low molecular mass iPP grades [18], γ-iPP could not be detected by WAXS technique in the samples studied.

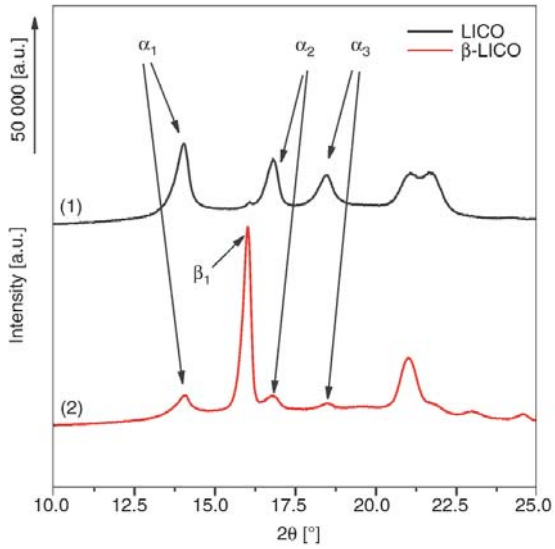

Figure 1. WAXS patterns of non-nucleated and β-nucleated LICO samples

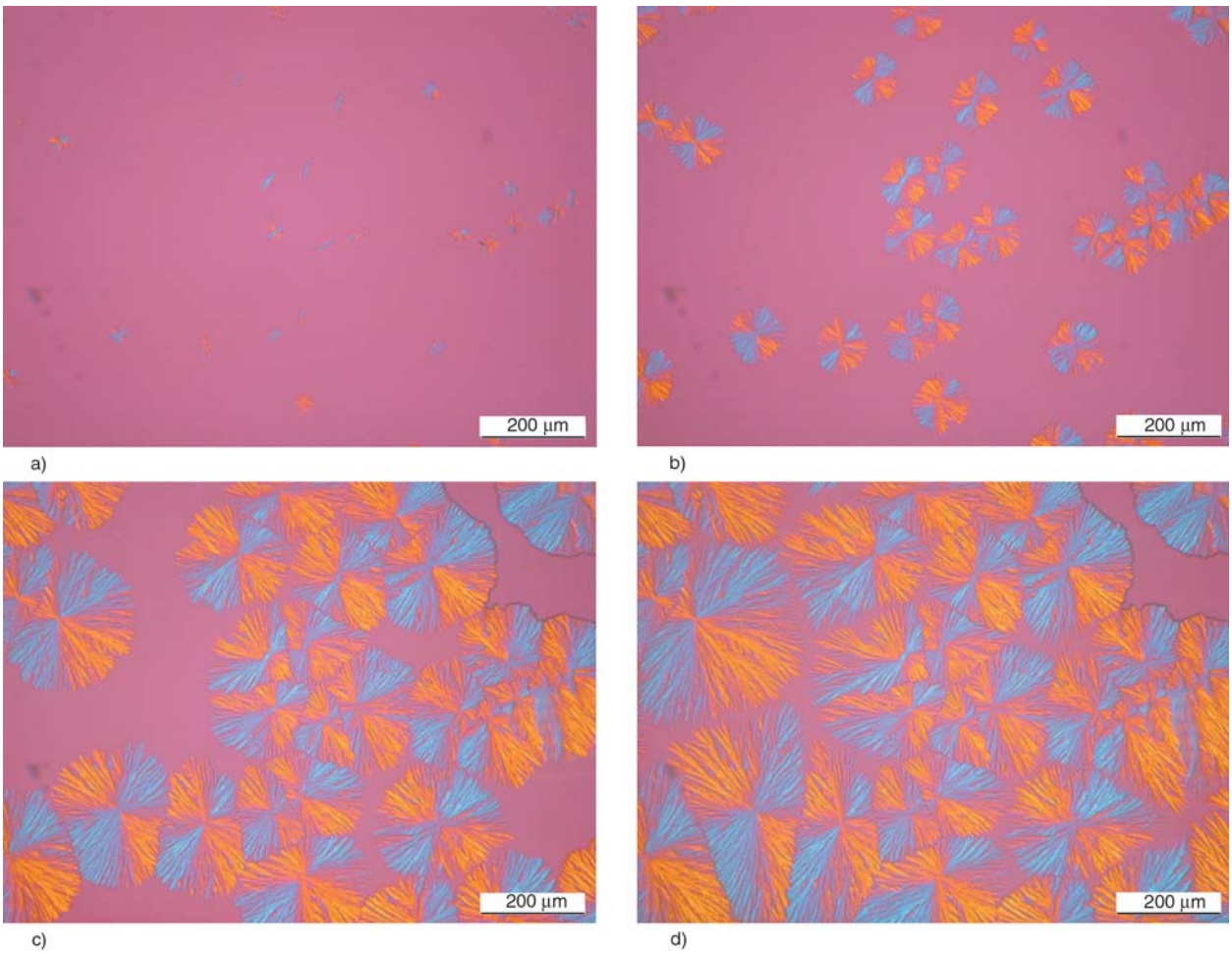

Figure 2. Supermolecular structure formed during isothermal crystallization of non-nucleated LICO sample at T_c = 130°C a) t_c = 5 min, b) t_c = 15 min, c) t_c = 45 min, d) t_c = 90 min

The supermolecular structure of LICO sample formed at 130°C is demonstrated in Figure 2. The micrographs illustrate the formation of large spherulites with positive birefringence. The lamellar branching can be observed even in PLM micrographs, indicating a more opened spherulitic structure of the low molecular mass product. In order to observe individual crystalline entities on the optical level, the β-nucleated samples were crystallized at T_c = 130°C (Figure 3). The size of the spherulites is much smaller than that in the non-nucleated sample, because of the presence of an efficient nucleating agent. The rod-like crystals with strong negative birefringence are formed in the early stage of crystallization (Figure 3b). These entities transform into β-spherulites during the latter stage of crystallization (Figure 3d). According to the former studies [4, 31] the rod like crystals are β-hexagonites viewed from their edge. They are the precursors of the β-spherulites.

3.2. Melting and crystallization of iPP with low molecular mass

The crystallization and melting curves of LICO and β-LICO samples and those of the CR-0 and β-CR-0 as a reference material are shown in Figure 4a and 4b. The peak temperature of crystallization of β-LICO (T_{cp} = 110.3°C) is higher than that of non-nucleated LICO samples (T_{cp} = 105.6°C), indicating the presence of an efficient nucleating agent. In spite of the formation of two different polymorphic phases, one peak appears in the crystallization curves of β-nucleated samples [4, 5]. Accordingly, the α- and the β-modifications crystallize simultaneously. On the other hand, T_{cp} of LICO and β-LICO is lower than that of non-nucleated and β-nucleated reference material (CR-0 and β-CR-0) with high molecular weight (T_{cp} = 111.8 and 119.1°C respectively).

The melting curves of low molecular mass samples are complex. The multiplied melting peaks indicate

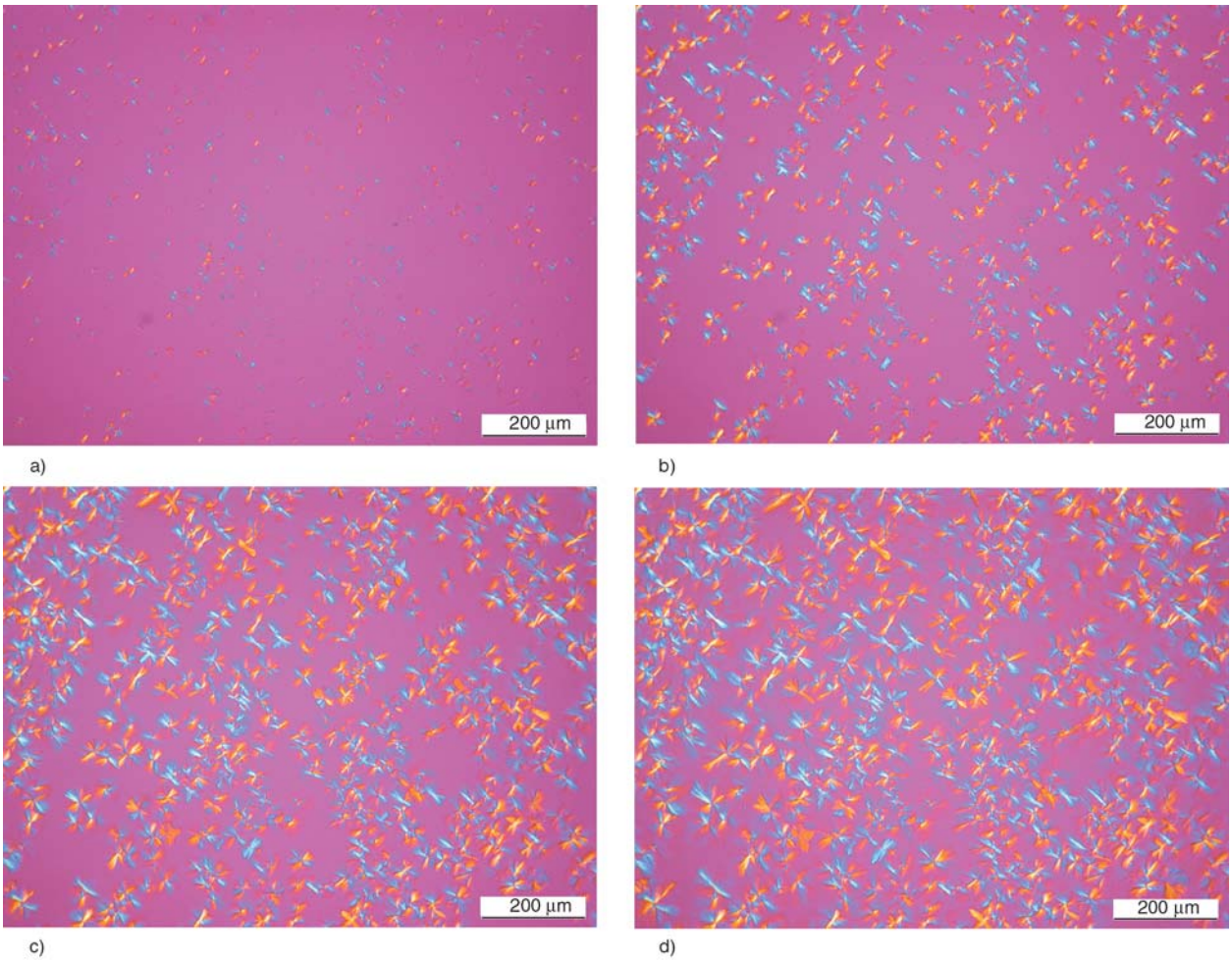

Figure 3. Supermolecular structure formed during isothermal crystallization of β-nucleated LICO sample at T_c = 130°C a) t_c = 1 min, b) t_c = 3 min, c) t_c = 6 min, d) t_c = 12 min

several processes taking places in the samples during heating. The doubled melting of LICO in temperature range 145–155°C corresponds to the melting of the α-modification (Figure 4b curve 1). The pronounced double melting peak of the non-recooled β-LICO sample at 135 and 140°C relates to melting of the β-modification (Figure 4b, curve 2). Moreover, a small melting peak of the α-modification is discernible on the melting curve of the latter. According to the melting memory effect of β-iPP [30], β-LICO sample cooled below T_R^* recrystallizes in to the α-form during the partial melting of unstable β-phase (βα-recrystallization) resulting in multiplied melting curves (Figure 4b, curve 3) and in the appearance of a large α-melting peak. The temperature range of the melting of the β-LICO is lower than that of α-LICO (Figure 4b), because of the lower thermodynamical stability of the β-form. Since the melting temperature of high molecular mass α- and β-form is at about 166 and 155°C respectively, the lower molecular mass results in a decreased melting temperature for both modifications. The lower melting temperature of low molecular mass material is connected with a higher density of the chain ends incorporated in the crystal lattice, which leads to the formation of crystal defects, consequently less perfect structure with lower structural stability. The melting peak duplication of the α- and β-modification (Figure 4b) can be explained by structural instability as well. The peak duplication resulted in the superposition of the endothermic perfection process (recrystallization) on the exothermic partial melting of the unstable crystal structure. Accordingly, the lower peak temperature (α and β) corresponds to the temperature, where the rate of the melting and recrystallization are identical [3, 4]. Consequently, the peaks at lower temperatures are not real, but apparent melting peak temperatures. The higher peak temperature (α′ and β′) indicates the melting of crystalline fraction formed during the recrystallization within the same phase (αα′- and ββ′-recrystallization) throughout heating.

The structural stability depends on the thermal condition of the crystallization. The lower the crystallization temperature is, the higher is the structural instability. In a series of experiment, samples of low molecular mass iPP with different structural stabilities were prepared under non-isothermal crystallization at different cooling rates. The crystallization curves of LICO and β-LICO recorded at different cooling rates are presented in Figure 5.

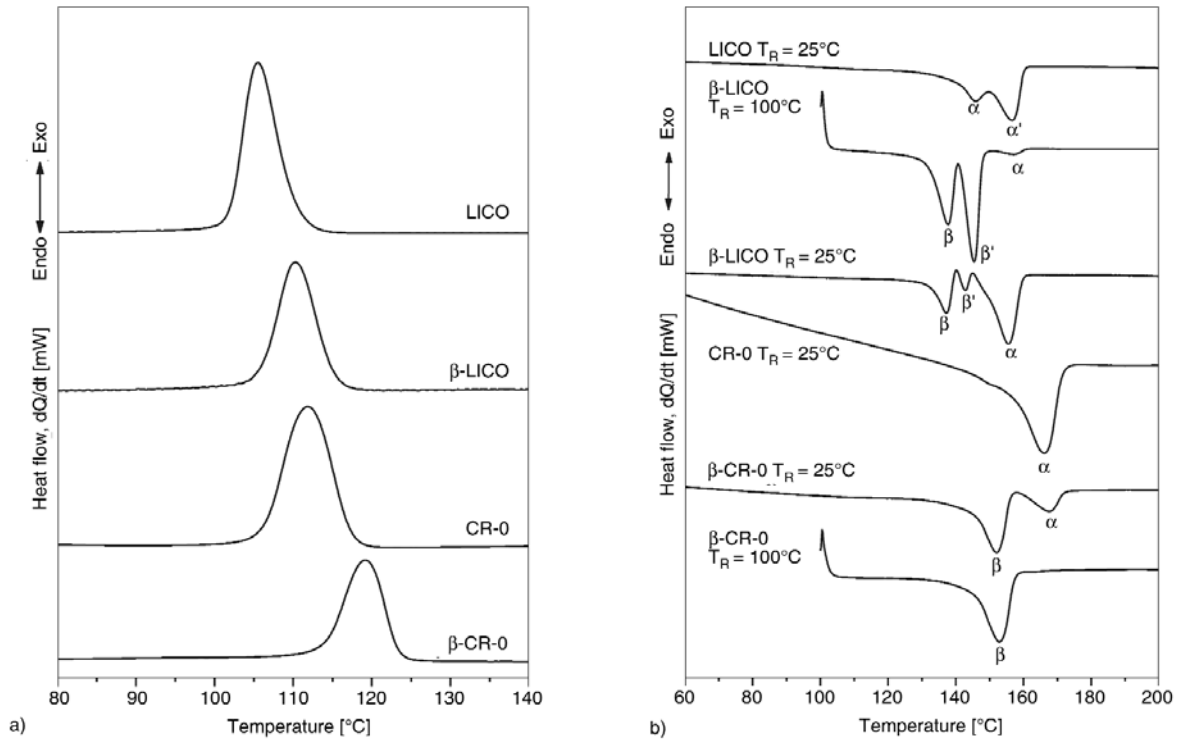

Figure 4. a) Crystallization curves of non-nucleated and β-nucleated LICO and CR-0 samples (T_R = 25°C) and b) melting curves of non-nucleated and β-nucleated LICO and CR-0 samples recorded after limited (T_R = 100°C) and non-limited recooling (T_R = 25°C). Note: the different thermal history of the samples is indicated in the melting curves.

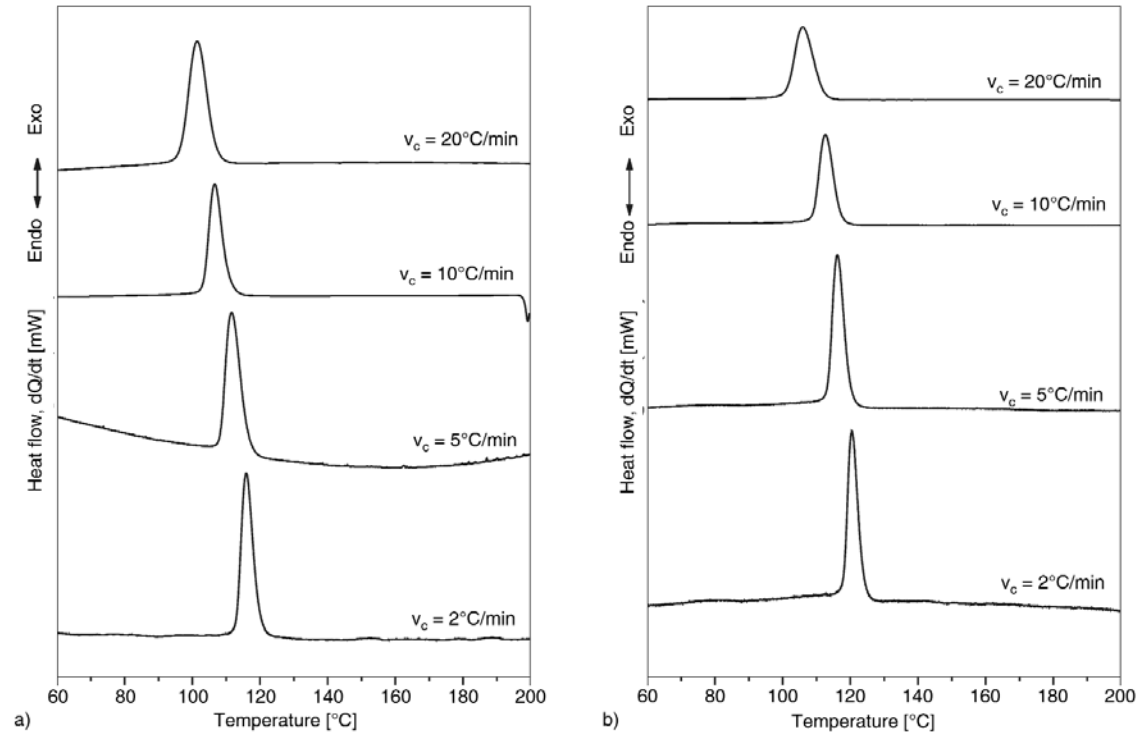

Figure 5. Crystallization curves of LICO (a) and β-LICO (b) sample registered at different cooling rate

The faster the cooling rate is, the lower is the peak temperature of crystallization and consequently the structural stability of the samples, although the β-nucleated LICO crystallizes always at higher temperature than the non-nucleated samples. The melting curves registered after cooling with different rates are given in Figure 6. It is unambiguous that the recrystallized part (intensity of peaks α′and β′) increases with increasing the cooling rate, confirming the higher structural instability. Simultane-

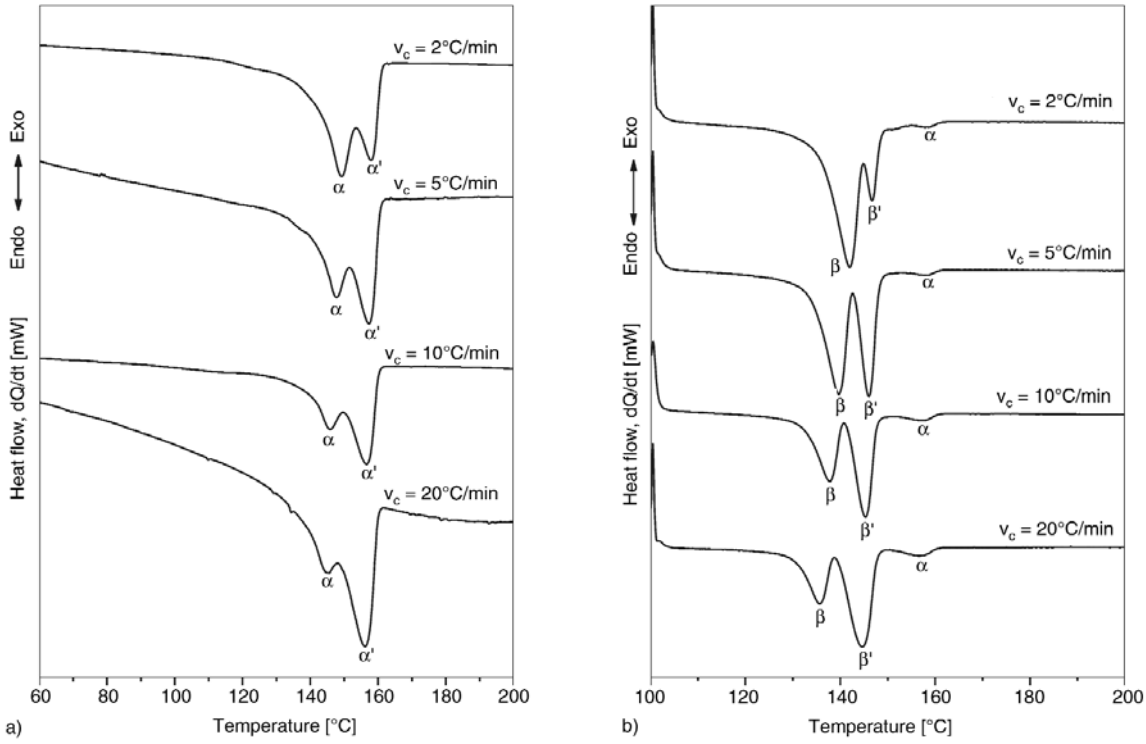

Figure 6. a) Melting curves of LICO crystallized at different cooling rate (T_R = 25°C), b) melting curves of β-LICO samples crystallized at different cooling rate (T_R^* = 100°C)

ously, the apparent melting peak (α and β) at lower temperature decreases, which confirms that the recrystallization starts at lower temperature in both modifications with increasing structural instability. Since the recrystallization is a time dependent process, the increase of the heating rate gradually surpasses the recrystallization during heating and consequently the peak duplication becomes less pronounced. This statement is proved by the melting curves presented in Figure 7a and 7b, where the influence of the heating rate on the melting profile of LICO and β-LICO is shown. It is well seen that the peak duplication at the highest heating rates (above 50°C/min) is almost disappears, i.e. the recrystallization is negligible. The melting peak temperature recorded with heating rate of 50°C/min (T_{mp} = 152.7°C) can be accepted as T_{mp} of crystalline fraction formed originally, because the disturbing effect of the αα′-recrystallization was practically eliminated. It worth mentioning that the inclination to the crystallisation can be approximately characterized by the apparent undercoolability, i.e. by the difference of melting and crystallization peak temperature ($\Delta T = T_{mp} - T_{cp}$). Based on the calorimetric data the undercoolability of non-nucleated and β-nucleated LICO and CR samples is summarized in Table 2. The ΔT value for non-nucleated samples is little lower than of 50°C. ΔT decreases monotonously with decreasing molecular mass. The lower undercoolability (the higher inclination for crystallization) of LICO is a consequence of higher chain mobility and lower melt viscosity. The β-nucleated samples have significantly lower ΔT, because of the presence of a highly efficient nucleating agent, but ΔT decreases with decreasing molecular mass similarly to the non-nucleated samples. The results obtained by the variation of the cooling and heating rates confirmed that the explanation of the multiplication of the melting peaks is correct.

The polymorphic composition can be calculated from the melting curve registered after limited recooling ($T_R = T_R^* = 100$°C). The β-content (β_c) estimated from the melting curve recorded after limited recooling is 97%. The β_c of the β-CR-0 is higher ($\beta_c > 99\%$) than that of β-LICO, signifying

Table 2. The crystallization (T_{cp},) melting peak temperatures (T_{mp}) and the undercoolability (ΔT) of non-nucleated and β-nucleated CR and LICO samples crystallized using 10°C/min of cooling and melted with 50°C/min of heating rate

Sample name	β-nucleated			Non-nucleated		
	T_{cp}	T_{mp}	ΔT	T_{cp}	T_{mp}	ΔT
CR-0	119.5	154.3	34.9	113.3	162.7	49.4
CR-200	120.0	154.3	34.4	114.1	162.7	48.5
CR-300	119.3	152.7	33.4	111.6	162.7	51.0
CR-500	120.3	152.7	32.4	114.8	162.7	47.9
CR-800	120.5	152.7	32.2	113.1	162.7	49.5
CR-1000	120.1	152.7	32.5	112.1	161.8	49.7
CR-1200	120.5	153.5	33.0	113.1	161.8	48.7
CR-1600	120.0	152.7	32.7	115.1	162.7	47.5
Licowax	110.3	142.7	32.4	105.5	152.7	47.2

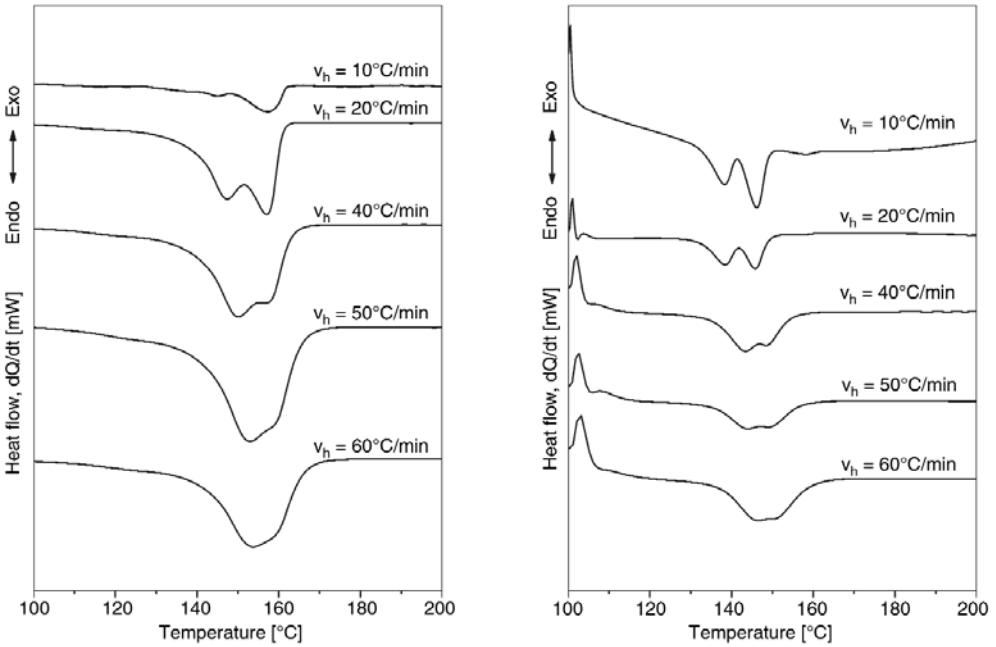

Figure 7. Melting curves of non-nucleated (a) and β-nucleated (b) LICO samples recorded with different heating rates

the reduced β-crystallization tendency of low molecular mass iPP.

3.3. Crystalline structure of peroxide-degraded samples

In order to determine the influence on the molecular mass on the structural stability and the inclination for recrystallization, iPP samples with different molecular masses and MFR were prepared by controlled degradation process (CR) in the presence of dicumyl-peroxide. The molecular mass and MFR range achieved by CR processing as a function of peroxide content are shown in Figure 8. The molecular mass of the samples is changing as a result of chain scission, which can influence the polydispersity and the regularity of the chain as well (Table 1). The WAXS patterns of non-nucleated CR samples registered on compression molded plaques are shown in Figure 9. The diffraction peaks indicate that the samples – except CR-0 – crystallize in α-modification in the whole MFR range. In the case of CR-0, a small peak at 2θ = 16° appears that corresponds to traces of β-iPP. Its formation is probably induced by mechanical load on the melt during compression moulding [32]. It should be noted that the diffraction peak of β-iPP is more pronounced in the CR-0 processed with slow cooling rate (Figure 9b). The diffraction patterns of β-nucleated CR samples are given in Figure 10. All samples crystallized in β-form independently of their MFR and

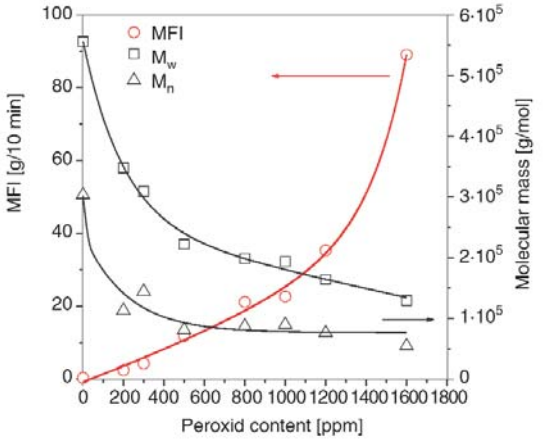

Figure 8. Dependence of the MFR and molecular weight (M_n and M_w) values of the CR samples on peroxide content

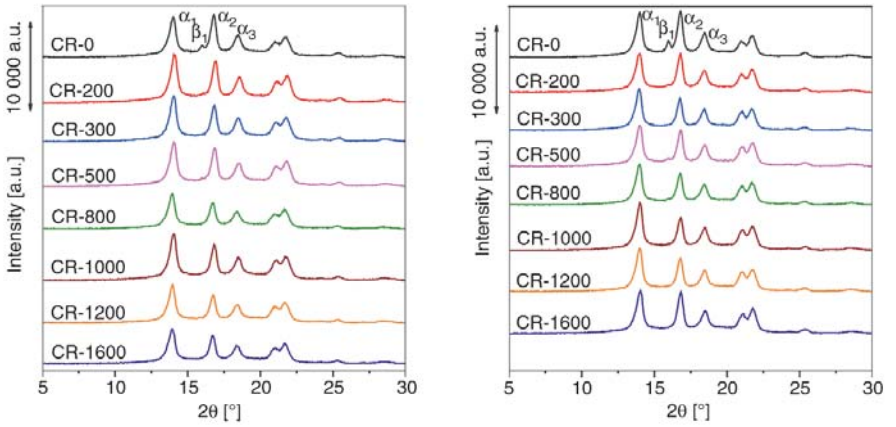

Figure 9. WAXS patterns of CR samples with different MFR processed by rapid (a) and slow (b) cooling

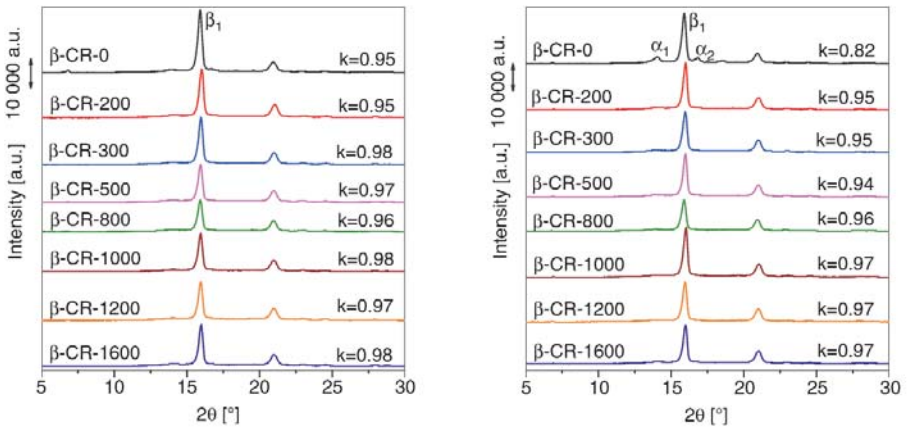

Figure 10. WAXS patterns of β-CR samples with different MFR processed by rapid (a) and slow (b) cooling

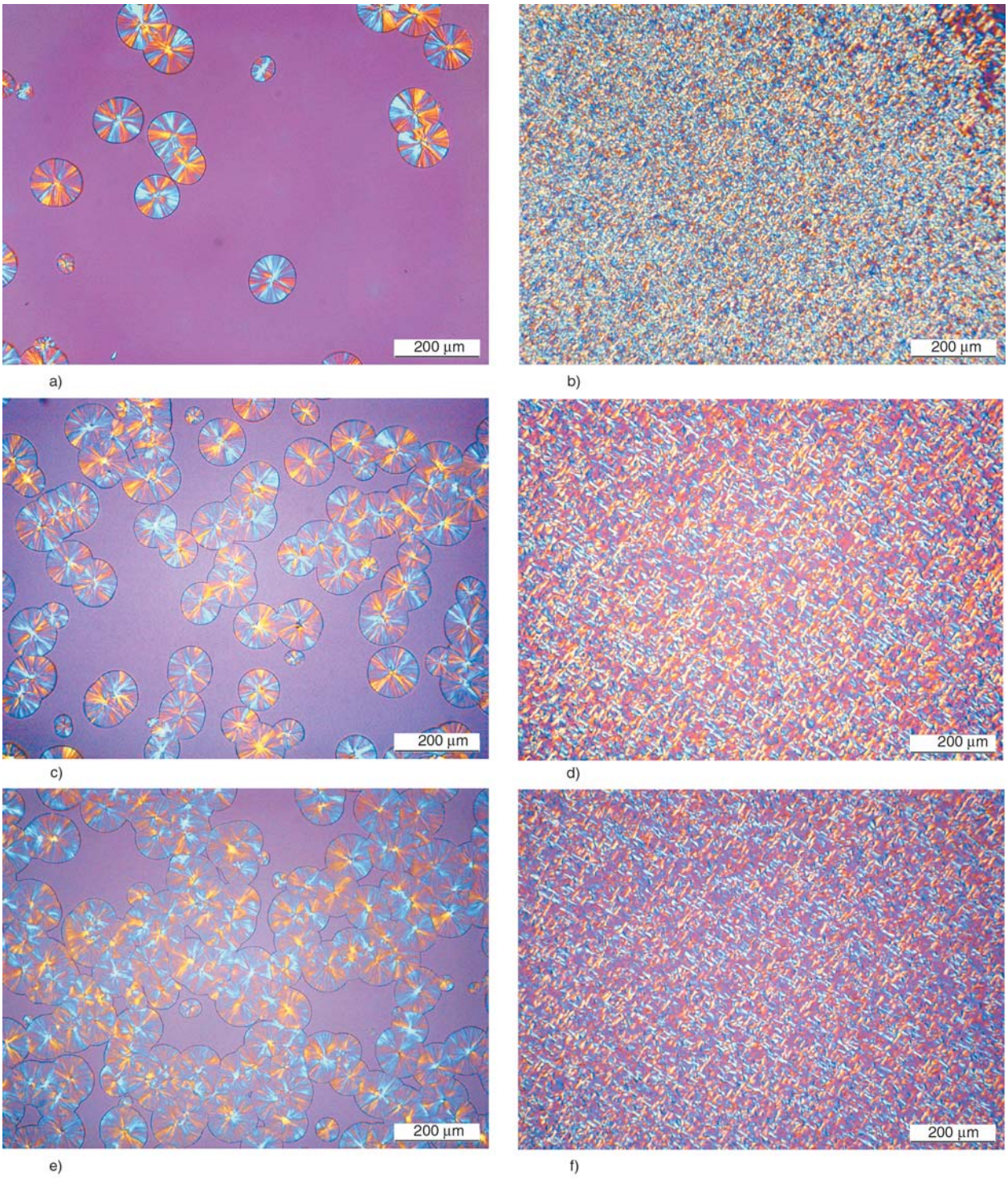

Figure 11. Supermolecular structure formed during isothermal crystallization of peroxide degraded samples at T_c = 130°C a) non-nucleated CR-0, t_c = 10 min; b) β-nucleated CR-0, t_c = 1 min; c) non-nucleated CR-800, t_c = 10 min; d) β-nucleated CR-800, t_c = 1.5 min; e) non-nucleated CR-1600, t_c = 10 min; f) β-nucleated CR-1600, t_c = 3 min

of the cooling rate applied during compression moulding. The *k* values are above 0.94 except the compression moulded plaque β-CR-0 produced with slow cooling. This can be explained by the formation of α-self nuclei in the high molecular weight sample above the upper critical temperature (140°C) of the formation of the β-iPP [3, 4].We have to emphasize that no formation of γ-form could be detected in the samples studied. The results ascertain that neither the decreasing molecular mass, nor the degradation of iPP result in the formation of γ-form. Based on our recent results, it

can be concluded that the stereo- and regio-defects might play dominant role in forming of γ-modification instead of low molecular mass. We suppose that iPP produced using recent superactive catalyst systems, which provide highly stereoregular structure (isotacticity is usually higher than 98%), is not inclined to the formation of γ-form. The formation of γ-iPP observed in the pioneering works on this topic [18] might be explained by the lower stereoregularity of the earlier iPP grades.

The supermolecular structure of peroxide degraded samples is demonstrated in Figure 11. Large spherulites are formed (Figure 11a) during the crystallization of the non-degraded reference material (CR-0) at T_c = 130°C. All non-nucleated samples crystallize essentially in α-modification. Figure 11a, 11c and 11e demonstrate the crystalline structure formed after 10 min of crystallization of CR-0, CR-800 and CR-1600 samples respectively. The number of spherulites formed increases with increasing peroxide content, representing the increased molecular mobility of the peroxide degraded samples. The larger the mobility of the chains is the higher is the rate of formation of the nuclei. The presence of the β-nucleating agent promotes the formation of microspherulitic structure, which consists of β-iPP exclusively. Moreover, the crystallization of β-nucleated samples is much faster than that of the non-nucleated ones.

3.4. Melting and crystallization characteristics of peroxide-degraded samples

The melting curves of non-nucleated CR samples registered after limited recooling are shown in Figure 12. The quantitative thermal characteristics obtained from evaluation of the crystallization and melting curves of non-nucleated CR samples are collected in Table 3. The non-nucleated CR samples with lager MFR possess higher peak temperature (Table 2) of crystallization (T_{cp}). These results hint at the increased chain mobility as the consequence of the decreased melt viscosity and lower entanglement density. The melting peak temperature shifts toward to lower temperatures with decreasing molecular mass. Moreover, peak duplication signifying the decreased structural stability appears above peroxide content of 800 ppm (CR-800–CR-1600). The enthalpy of fusion (ΔH_m) increases with increasing MFR. We have to point out that this apparent increase can be caused by the more and more pronounced αα′-recrystallization with decreasing molecular mass. The more pronounced the recrystallization is, the higher is the ΔH_m values.

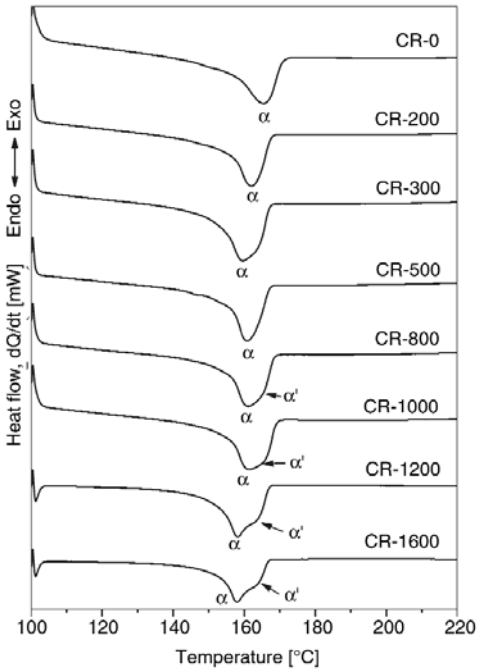

Figure 12. Melting curves of CR samples crystallized at cooling rate of 10°C/min (T_R = 100°C)

Table 3. Thermal characteristics of non-nucleated CR samples determined on the basis of the melting and crystallization curves (T_R = 25°C)

Samples	ΔH_c [J/g]	T_{mp} [°C]	ΔH_m [J/g]
CR-0	86.0	166.0	80.0
CR-200	88.0	162.7	83.4
CR-300	88.1	159.7	83.2
CR-500	90.3	161.7	85.8
CR-800	90.0	161.4	87.2
CR-1000	89.5	(α) 161.5 (α') 166.3	88.1
CR-1200	90.8	(α) 158.4 (α') 164.7	89.6
CR-1600	88.8	(α) 158.2 (α') 164.6	87.3

T_{mp} – peak temperature of melting of α-modification, where α and α' are the temperatures of the doubled melting peaks

The melting curves of the non-recooled, β-nucleated CR samples are given in Figure 13. The quantitative thermal characteristics obtained from the evaluation of crystallization and melting curves of β-nucleated CR samples are collected in Table 4. The peak temperatures of crystallization of β-nucleated samples are higher than those of the non-nucleated ones and located in the vicinity of 120°C.

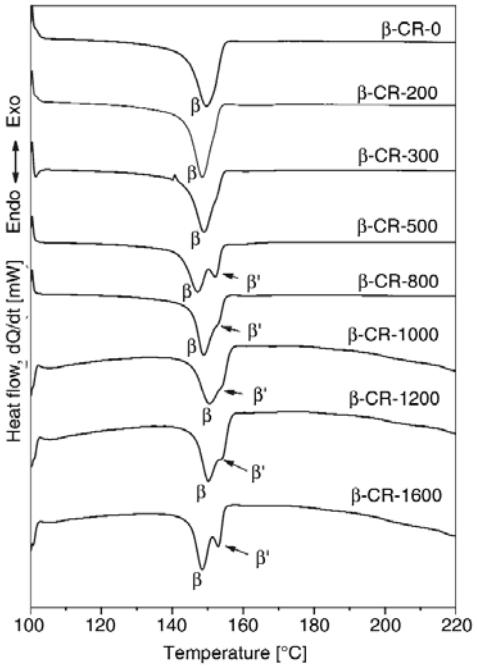

Figure 13. Melting curves β-nucleated CR crystallized at a cooling rate of 10°C (T_R = 100°C)

T_{cp} values increase slightly with increasing MFR (Table 4). The melting peaks are located in the temperature range of 145–155°C, which is characteristic of the β-iPP with high molecular mass. Furthermore, melting shifts toward lower temperatures with decreasing of molecular mass, similarly to the non-nucleated CR samples. The duplication of melting peak becomes visible at higher molecular mass range compared with non-nucleated samples. The pronounced peak duplication, which is caused by the ββ′-recrystallization of the unstable crystalline structure, can be clearly seen in β-CR-500–β-CR-1600 samples (Figure 13). This observation ascertains that the structural stability of β-form is smaller than that of α-form, in spite of the fact that the β-nucleated samples are crystallized at higher temperature range (Table 3 and 4). The β_c values are higher than 98% in most of β-nucleated CR samples.

The melting curves of β-nucleated samples cooled to room temperature are shown in Figure 14. The melting profiles reflect that βα-recrystallization takes place during heating according to former observations [3, 4, 30]. It seems that increasing number of crystal defects caused by the chain ends included in the crystal lattice with decreasing of molecular mass promote the βα-recrystallization as well. Therefore, the βα-recrystallization overlaps with and suppresses the ββ′-recrystallization. The melting peak duplication hinting at the ββ′-recrystallization within the β-form appears only in the case of β-CR-1600 sample as an indistinct shoulder on the melting cure.

We have to call the attention to the fact once again that βα-recrystallization superimposed on the partial melting of the β-phase during heating of the samples cooled down to room temperature influences the melting profile considerably. Therefore, melting peak temperatures and enthalpy of fusion determined from the melting curves recorded during heating from room temperature are apparent values. Consequently, the melting curves of recooled samples do not provide exact information about β_c. Indeed, the β_c values determined from melting curves of samples heated from room temperature are much lower than those obtained from

Table 4. Thermal characteristics of β-nucleated CR samples determined on the basis of the melting and crystallization curves

Samples	Heating after limited recooling (T_R = 100°C)			Cooling to room temperature and subsequent heating (T_R = 25°C)		
	T_{mp} [°C]	ΔH_m [J/g]	β_c [%]	ΔH_c [J/g]	ΔH_m [J/g]	β_c [%]
β-CR-0	149.7	82.2	98.8	85.4	95.1	78.7
β-CR-200	148.5	81.5	98.5	85.7	94.0	79.0
β-CR-300	149.0	86.2	98.3	81.2	88.5	76.8
β-CR-500	(β) 147.2 (β') 152.2	86.0	96.8	82.5	85.8	73.1
β-CR-800	(β) 148.9 (β') 153.0	88.7	98.2	84.6	87.3	77.9
β-CR-1000	(β) 150.5 (β') 154.2	86.8	99.4	79.2	61.4	77.1
β-CR-1200	(β) 149.9 (β') 153.7	88.5	99.2	79.1	62.8	75.6
β-CR-1600	(β) 148.5 (β') 153.0	85.8	99.2	78.2	64.2	70.9

T_{mp} – peak temperature of melting of α-modification, where β and β' are the temperatures of the multiplied melting peaks

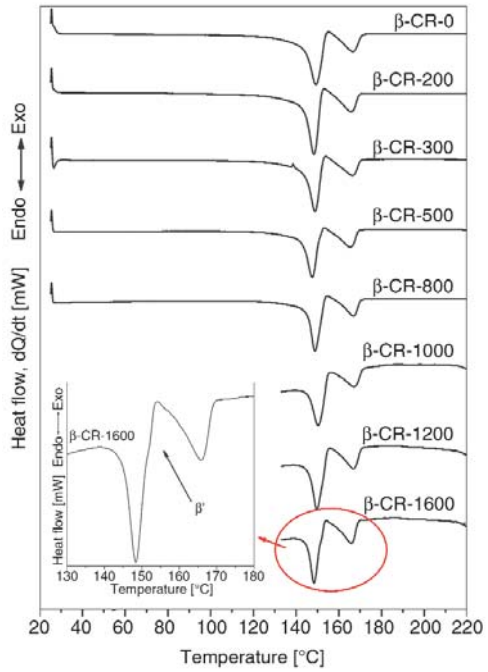

Figure 14. Melting curves of β-nucleated CR samples crystallized at cooling rate of 10°C/min (T_R = 25°C)

non-recooled melting curves recorded during heating from 100°C (Table 4).

4. Conclusions

The objective of this work was to investigate the effect of molecular mass on the crystallization tendency of the polymorphic modifications of iPP in wide range. The results prove that iPP crystallizes essentially in α-form and the β-modification can be prepared by application of a highly active and selective β-nucleating agent in wide molecular mass range studied. The effect of molecular mass was studied on peroxide-degraded samples and a commercial iPP product with low molecular mass. Our results revealed that the decrease of molecular mass leads to increased structural instability of both α- and β-modification, which is manifested in decreasing of the melting temperature and in the enhanced inclination to the recrystallization during heating. The structural instability can be explained by the incorporation of the chain ends into the crystal lattices. The shorter the chains are the larger is the density of the incorporated chain ends and consequently the structural instability. The perfection process of unstable crystalline structure leads to pronounced αα′- and ββ′-peak duplication. In contrary to literature sources, which have reported that γ-modification forms in degraded samples and in low molecular mass iPP grades [18], γ-iPP could not detected in the samples studied. The recently used catalysts systems seem to provide highly stereoregular structure, which is not liable to crystallize in γ-form.

References

[1] Slichter W. P., Mandell E. R.: Spherulitic crystallization in polypropylene. Journal of Applied Physics, **30**, 1479–1484 (1959). DOI: 10.1063/1.1734985

[2] Lotz B., Wittmann J. J., Lovinger A. J.: Structure and morphology of poly(propylenes): A molecular analysis. Polymer, **37**, 4979–4992 (1996). DOI: 10.1016/0032-3861(96)00370-9

[3] Varga J.: Crystallization, melting and supermolecular structure of isotactic polypropylene. in 'Polypropylene: Structure, blends and composites' (ed.: Karger-Kocsis J.) Chapmann and Hall, London, Vol 1, 56–115 (1995).

[4] Varga J.: β-modification of isotactic polypropylene: Preparation, structure, processing, properties, and application. Journal of Macromolecular Science Part B: Physics, **41**, 1121–1171 (2002). DOI: 10.1081/MB-120013089

[5] Menyhárd A., Varga J., Molnár G.: Comparison of different β-nucleators for isotactic polypropylene, characterisation by DSC and temperature-modulated DSC (TMDSC) measurements. Journal of Thermal Analysis and Calorimetry, **83**, 625–630 (2006). DOI: 10.1007/s10973-005-7498-6

[6] Varga J., Menyhárd A.: Effect of solubility and nucleating duality of *N,N′*-dicyclohexyl-2,6-naphthalenedicarboxamide on the supermolecular structure of isotactic polypropylene. Macromolecules, **40**, 2422–2431 (2007). DOI: 10.1021/ma062815j

[7] Leugering H. J.: Einfluss der Kristallstuktur und Überstuktur auf einige Eigeschaften von Polypropylen. Die Makromolekulare Chemie, **109**, 204–216 (1967). DOI: 10.1002/macp.1967.021090118

[8] Shi G-Y., Zhang X-D., Qiu Z-X.: Crystallization kinetics of β-phase poly(propylene). Makromolekulare Chemie-Macromolecular Chemistry and Physics, **193**, 583–591 (1992). DOI: 10.1002/macp.1992.021930303

[9] Ikeda N., Kobayashi T., Killough L.: Novel β-nucleator for polypropylene. in 'Polypropylene '96. World Congress', Zürich, Switzerland, 1–10 (1996).

[10] Xiao W. C., Wu P. Y., Feng J. C., Yao R. Y.: Influence of a novel β-nucleating agent on the structure, morphology, and nonisothermal crystallization behavior of isotactic polypropylene. Journal of Applied Polymer Science, **111**, 1076–1085 (2009). DOI: 10.1002/app.29139

[11] Varga J., Mudra I., Ehrenstein G. W.: Highly active thermally stable β-nucleating agents for isotactic polypropylene. Journal of Applied Polymer Science, **74**, 2357–2368 (1999).
DOI: 10.1002/(SICI)1097-4628(19991205)74:10<2357::AID-APP3>3.0.CO;2-2

[12] Zhang Z., Wang C., Yang Z., Chen C., Mai K.: Crystallization behavior and melting characteristics of PP nucleated by a novel supported β-nucleating agent. Polymer, **49**, 5137–5145 (2008).
DOI: 10.1016/j.polymer.2008.09.009

[13] Zhang Z., Tao Y., Yang Z., Mai K.: Preparation and characteristics of nano-$CaCO_3$ supported β-nucleating agent of polypropylene. European Polymer Journal, **44**, 1955–1961 (2008).
DOI: 10.1016/j.eurpolymj.2008.04.022

[14] Varga J., Ehrenstein G. W., Schlarb A. K.: Vibration welding of alpha and β isotactic polypropylenes: Mechanical properties and structure. Express Polymer Letters, **2**, 148–156 (2008).
DOI: 10.3144/expresspolymlett.2008.20

[15] Grein C., Gahleitner M.: On the influence of nucleation on the toughness of iPP/EPR blends with different rubber molecular architectures. Express Polymer Letters, **2**, 392–397 (2008).
DOI: 10.3144/expresspolymlett.2008.47

[16] Addink Miss E. J., Beintema J.: Polymorphism of crystalline polypropylene. Polymer, **2**, 185–193 (1961).
DOI: 10.1016/0032-3861(61)90021-0

[17] Phillips P. J., Mezghani K.: Polypropylene, isotactic (polymorphism). in 'The polymeric materials encyclopedy' (ed.: Salamon J. C.) CRC Press, Boca Raton, Vol 9, 6637–6649 (1996).

[18] Morrow D. R., Newman B. A.: Crystallization of low-molecular-weight polypropylene fractions. Journal of Applied Physics, **39**, 4944–4950 (1968).
DOI: 10.1063/1.1655891

[19] Wang S-W., Yang W., Xu Y-J., Xie B-H., Yang M-B., Peng X-F.: Crystalline morphology of β-nucleated controlled-rheology polypropylene. Polymer Testing, **27**, 638–644 (2008).
DOI: 10.1016/j.polymertesting.2008.04.004

[20] Chvatalova L., Navratilova J., Cermak R., Raab M., Obadal M.: Joint effects of molecular structure and processing history on specific nucleation of isotactic polypropylene. Macromolecules, **42**, 7413–7417 (2009).
DOI: 10.1021/ma9005878

[21] Výchopnová J., Cermák R., Obadal M., Verney V., Commereuc S.: Effect of β-nucleation on crystallization of photodegraded polypropylene. Journal of Thermal Analysis and Calorimetry, **95**, 215–220 (2009).
DOI: 10.1007/s10973-008-8892-7

[22] Campbell R. A., Phillips P. J., Lin J. S.: The gamma phase of high-molecular-weight polypropylene: 1. Morphological aspects. Polymer, **34**, 4809–4816 (1993).
DOI: 10.1016/0032-3861(93)90002-R

[23] Brückner S., Meille S. V., Petraccone V., Pirozzi B.: Polymorphism in isotactic polypropylene. Progress in Polymer Science, **16**, 361–404 (1991).
DOI: 10.1016/0079-6700(91)90023-E

[24] Krache R., Benavente R., López-Majada J. M., Pereña J. M., Cerrada M. L., Pérez E.: Competition between α, β, and γ polymorphs in β-nucleated metallocenic isotactic polypropylene. Macromolecules, **40**, 6871–6878 (2007).
DOI: 10.1021/ma0710636

[25] Juhász P., Belina K.: Crystallization and morphology of propylene/pentene random copolymers. Journal of Reinforced Plastics and Composites, **20**, 2–11 (2001).
DOI: 10.1106/A7N4-7YFW-YG88-NDP8

[26] Juhász P., Varga J., Belina K., Belina G.: Efficiency of β-nucleating agents in propylene/alpha-olefin copolymers. Journal of Macromolecular Science Part B: Physics, **41**, 1173–1189 (2002).
DOI: 10.1081/MB-120013090

[27] Sheng B-R., Li B., Xie B-H., Yang W., Feng J-M., Yang M-B.: Influences of molecular weight and crystalline structure on fracture behavior of controlled-rheology-polypropylene prepared by reactive extrusion. Polymer Degradation and Stability, **93**, 225–232 (2008).
DOI: 10.1016/j.polymdegradstab.2007.09.011

[28] Azizi H., Ghasemi I., Karrabi Q.: Controlled-peroxide degradation of polypropylene: Rheological properties and prediction of MWD from rheological data. Polymer Testing, **27**, 548–554 (2008).
DOI: 10.1016/j.polymertesting.2008.02.004

[29] Turner J. A., Aizlewood J. M., Beckett D. R.: Crystalline forms of isotactic polypropylene. Macromolecular Chemistry, **75**, 134–158 (1964).
DOI: 10.1002/macp.1964.020750113

[30] Varga J.: Melting memory effect of the β-modification of polypropylene. Journal of Thermal Analysis, **31**, 165–172 (1986).

[31] Varga J., Ehrenstein G. W.: High-temperature hedritic crystallization of the β-modification of isotactic polypropylene. Colloid and Polymer Science, **275**, 511–519 (1997).
DOI: 10.1007/s003960050113

[32] Varga J., Karger-Kocsis J.: Rules of supermolecular structure formation in sheared isotactic polypropylene melts. Journal of Polymer Science Part B: Polymer Physics, **34**, 657–670 (1996).
DOI: 10.1002/(SICI)1099-0488(199603)34:4<657::AID-POLB6>3.0.CO;2-N

eXPRESS Polymer Letters Vol.4, No.2 (2010) 115–129
Available online at www.expresspolymlett.com
DOI: 10.3144/expresspolymlett.2010.16

Linear low-density polyethylene/silica micro- and nanocomposites: dynamic rheological measurements and modelling

A. Dorigato[*], *A. Pegoretti, A. Penati*

Department of Materials Engineering and Industrial Technologies, University of Trento, 38123 Trento, Italy

Received 13 October 2009; accepted in revised form 12 December 2009

Abstract. Linear low-density polyethylene (LLDPE) based composites were prepared by melt compounding with 1, 2, 3 and 4 vol% of various kinds of amorphous silicon dioxide (SiO_2) micro- and nanoparticles. Dynamic rheological tests in parallel plate configuration were conducted in order to detect the role of the filler morphology on the rheological behaviour of the resulting micro- and nanocomposites. A strong dependence of the rheological parameters from the filler surface area was highlighted, with a remarkable enhancement of the storage shear modulus (G') and of the viscosity (η) in fumed silica nanocomposites and in precipitated silica microcomposites, while glass microbeads only marginally affected the rheological properties of the LLDPE matrix. This result was explained considering the formation of a network structure arising from particle-particle interactions due to hydrogen bonding between silanol groups. A detailed analysis of the solid like behaviour for the filled samples at low frequencies was conducted by fitting viscosity data with a new model, based on a modification of the original De Kee-Turcotte expression performed in order to reach a better modelling of the high-frequency region.

Keywords: *nanocomposites, polyethylene, silica, modelling, rheology*

1. Introduction

One of the most important consequences of the incorporation of nanofillers in molten polymers is the significant change in their viscoelastic properties [1]. The reduction of the filler size down to nanometric scale can produce substantial differences in the rheology and dynamic of filled polymer in comparison to micron sized particles [2–7]. In fact, polymer composites reinforced with submicron fillers generally show significant enhancements in the viscoelastic properties compared to microcomposites at similar filler contents, associated to the appearance of a secondary plateau for the dynamic storage modulus (G') in the low frequency regime [3, 6–10]. These effects can be explained considering that the extremely large surface area provided by nanoparticles can intensify the effect of particle-particle and/or polymer-particle thermodynamic interactions [4, 5, 11–14]. When filler-filler interactions dominate, it is believed that the rheological response of the material is influenced by the destruction and reconstruction of a filler network and/or agglomerates during mechanical loading [8, 9, 15, 16]. On the other hand, when polymer-filler interaction is the driving factor, the viscoelasticity of the melt is controlled by the dynamics of the stick-slip motion of the polymer chains around the filler surface [17–22]. During the past few years, the linear viscoelastic behaviour in the molten state of polymer nanocomposites filled with organically modified clays has been widely investigated [23–31], and the subject

[*]Corresponding author, e-mail: andrea.dorigato@ing.unitn.it

has been reviewed by Krishnamoorti and Yurekli [26]. Studying the rheological response of polystyrene/clay nanocomposites, Zhao *et al*. [30] found that the level of dispersion was markedly correlated with the rheological response. Gupta *et al*. [25] prepared a series of ethylene-vinyl acetate/clay nanocomposites, finding a marked shear thinning behaviour with respect to the unfilled sample at filler loadings higher than 2.5 wt%. Wu *et al*. [29] prepared polylactide/clay nanocomposites by melt mixing, revealing the formation of a solid-like behaviour for clay loadings higher than 4 wt%, taken as the percolation threshold for the formation of a physical network. With the term percolation threshold, the authors intended a critical concentration above which the distance between clay nanoplatelets was sufficiently low to allow the formation of a space filling network constituted by physical interactions between clay lamellae in steady state conditions. This physical network could be destroyed by the oscillatory large amplitude shear deformation and could be eventually reorganized under quiescent annealing condition. Similar results can be also found in some papers dealing with the rheological behaviour of polymer/carbon nanotubes (CNT) nanocomposites [32–37]. Ganß *et al*. [33] found a systematic increase in melt viscosity for polypropylene/multiwalled CNT nanocomposites. Abdel-Goad and Pötschke [32] found that the dynamic moduli and the viscosity of polycarbonate/multiwalled CNT composites increased with increasing the CNT content, with a transition from a liquid like to a solid like behaviour at concentrations of only 0.5 wt%. In this case the transition was related to the formation of a combined network between the nanotubes and the polymer chains. Similar conclusions were reported by Song [37] in a paper on the rheological properties of poly(ethylene oxide)/carbon nanotubes composites. Furthermore, Prashantha *et al*. [35, 36] prepared multi-wall carbon nanotubes (MWNTs) filled polypropylene (PP) nanocomposites, utilizing polypropylene grafted maleic anhydride (PP-g-MA), demonstrating that PP-g-MA promotes the dispersion of MWNTs in PP matrix and the interfacial strength, thus greatly improving the rheological percolation threshold and the mechanical properties of the resulting nanocomposites.

Quite surprisingly, very little information are available on the viscoelastic behaviour of silica filled polymer nanocomposites in the molten state [38]. Fumed silica nanoparticles exist in a wide range of size (specific area ranging from 50 to 400 m^2/g) and with a variety of surface treatments from hydrophilic to hydrophobic. Due to their fractal structure and their high specific area, fumed silica is subjected to self-aggregation and can consequently form a network of connected or interacting particles in the molten polymer. Consequently, the most important application of fumed silica is the improvement of the rheological properties of paints [38] and for reinforcing elastomers [39]. Bartholome *et al*. [40] prepared polystyrene/grafted silica nanocomposites, finding significant enhancements of storage shear modulus in the low frequency regime, especially when unmodified silica was utilized. It was also evidenced that the grafted polymer chains on the silica particles surface created a steric repulsion between the filler particles, preventing the formation of a silica network within the polymer matrix, with a consequent decrease of the rheological properties with respect to the untreated silica filled systems. By a 'freeze-drying' technique, Zhang and Archer [10] prepared poly(ethylene oxide) (PEO) based nanocomposites containing isotropic silica nanospheres, in order to study the effects of polymer-particle and particle-particle interactions on viscoelastic properties of the resulting materials. Even in this case, viscoelastic parameters indicated a transition to a solid-like response at low oscillation frequencies for particle volume fractions as low as 2%, dramatically lower than the theoretical percolation threshold (30%). In order to explain their observations the authors proposed a mechanism in which nanosized silica particles, surrounded by an immobilized shell of PEO, were bridged by much larger polymer molecules. Cassagnau [38] concluded that the solid-like behaviour displayed by polymer-silica nanocomposites is influenced by the silica surface treatment and by the molecular weight of the matrix, and is mainly promoted by particle-particle interaction in fumed silica nanocomposites, while the particle-polymer interaction is the dominant one in colloidal silica nanocomposites. The critical filler concentration beyond which interparticle interactions begin to play an important role on the rheological proper-

ties, called percolation threshold (Φ_c), was computed in some papers. Cassagnau [41] studied the viscoelastic properties of nanosilica-filled ethylene vinyl acetate copolymer (EVA, 60 wt% of vinyl acetate) in the molten state and diluted EVA/xylene solution, finding a liquid-solid transition at Φ_c = 3.3 vol%, independently from the polymer chain regimes (entangled or Rouse regime). Inoubli *et al.* [42] observed that 2.5 vol% of silica in polybutylacrylate nanocomposite was very close to the percolation threshold.

Starting from these considerations, the objective of the present work is to investigate the linear viscoelastic behaviour of silica micro- and nanocomposites in the molten state, in order to find, at least from a qualitative point of view, a correlation between the filler characteristics (size and surface area) and the resulting dynamic rheological properties. In order to pursue this scope, a non-polar polymeric matrix, linear low-density polyethylene (LLDPE) and three types of untreated amorphous silicon dioxide (SiO_2) micro- and nanofillers (i.e. glass microspheres, precipitated silica microparticles, and fumed silica nanoparticles) were used. Experimental data were then analyzed according to some of the existing models [43–46], and a modification of the original De Kee-Turcotte model [44] was proposed to fit rheological data over the entire frequency range.

2. Experimental section

A Flexirene® CL10 linear low-density polyethylene (MFI at 190°C and 2.16 kg = 2.6 g/10′, M_n = 27000 g/mol, density = 0.918 g/cm^3). This material is produced by Polimeri Europa S.p.A. (Mantova, Italy) using Ziegler-Natta catalysis and butene as a comonomer (C_4-LLDPE).

Various types of amorphous silica micro- and nanoparticles were used as fillers:

i) Cores® silica glass microspheres, having a mean particle size of about 50 μm and a surface area lower than 1 m^2/g. On the particles sieved in a 32 μm mesh, a mean diameter of 18±3 μm was evaluated through optical microscopy.

ii) Sipernat® 160 precipitated silica microparticles, supplied by Degussa (Hanau, Germany). Precipitated silica consists of a three-dimensional network of coagulated primary silica particles. The latter grow to sizes higher than 10 nm before they coagulate to form the aggregated clusters in the micrometric range of size [47, 48]. Despite their micrometric dimensions (7–8 μm), these microparticles possess elevated surface area values (around 160 m^2/g), because of their high surface porosity.

iii) Aerosil® commercial fumed silica nanoparticles, supplied by Degussa (Hanau, Germany). According to the producer's datasheets, Aerosil 200 has a nominal specific surface area (SSA) of about 200 m^2/g, while for Aerosil 380 a nominal SSA value of about 380 m^2/g is reported on the material data sheet.

Density was measured through a Micromeritics Accupyc® 1330 helium pycnometer, while specific surface area was determined by an ASAP® 2010 Accelerated Surface Area and Porosimetry machine, according to the Brunauer-Emett-Teller (BET) procedure [49]. Table 1 summarizes the experimental density and SSA values of the silica micro- and nanoparticles used in this work.

Polyethylene chips and all fillers were used as received. The samples were prepared by melt compounding followed by hot pressing. The filler was melt compounded with LLDPE in a Thermo Haake® internal mixer, at 170°C for 15 min and 90 rpm. The materials were then hot pressed in a Carver® laboratory press at 170°C for 15 min at low pressure (0.2 kPa), in order to obtain square sheets about 0.8 mm thick. The filler content was varied between 1 and 4 vol%. In all figures and in the discussion session, glass microspheres were simply designated as Glass, precipitated silica microparticles were denoted as S160, while fumed silica nanopowders were designated with the letter A200 or A380 depending on the nominal specific surface area. The unfilled matrix is indicated as LLDPE, while the composites were denoted as LLDPE followed by the name of the filler and the

Table 1. Density and specific surface area values of micro- and nanosilica fillers utilized in this work

Type of filler	Density[a] [g/cm^3]	BET surface area[b] [m^2/g]
Glass microspheres	2.43 ± 0.01	0.5 ± 0.1
Sipernat 160	1.85 ± 0.01	168.3 ± 0.6
Aerosil 200	2.27 ± 0.02	196.6 ± 1.7
Aerosil 380	2.41 ± 0.02	320.8 ± 3.4

[a]Measured through a Micromeritics Accupyc® 1330 helium pycnometer

[b]Measured through ASAP® 2010 Accelerated Surface Area and Porosimetry machine

filler volume content (vol%). For example LLDPE-A200-2 indicates 2 vol% Aerosil 200 fumed silica nanocomposite sample.

Observations of the fracture surface of LLDPE-Glass-2 composites were taken by using a Philips® XL30 environmental scanning electron microscope (ESEM), at an acceleration voltage between 15 and 30 kV. Thin samples (0.6 mm) were cryofractured under impact conditions and prepared for the observations. Transmission electronic microscope (TEM) images of LLDPE-A380-2 and LLDPE-S160-2 samples were taken by a Philips®/FEI CM120 microscope, at an accelerating voltage of 80 kV. Thin sections of the samples were ultramicrotomed at a temperature of –70°C by using a Reichert-Jung® Ultracut FC4E crio-ultramicrotome.

Dynamic rheological tests were conducted by a TA Instruments® Ares Rheometer in parallel plate configuration, at a temperature of 190°C. Plates with a diameter of 25 mm and a distance of 0.8 mm were chosen for these tests. A maximum shear strain (γ_0) of 1% was imposed to the samples, while the frequency range was varied between 0.05 and 200 rad/s.

3. Results and discussions

3.1. Microstructural characterization

The rheological behaviour of particulate filled polymers strongly depends on the particle size and dispersion degree. In Figure 1a an ESEM image of the fracture surface of LLDPE-Glass-2 composite is reported. The typical microstructure of particulate filled microcomposites is evidenced, with the presence of spherical smooth microparticles with mean dimension of about 15–20 μm, homogeneously distributed through the sample. In Figures 1b and 1c TEM images of the fracture surfaces of LLDPE-S160-2 and LLDPE-A380-2 composites are respectively reported. Precipitated silica composite is characterized by the presence of almost equiaxial aggregates of about 400 nm in diameter, homogeneously dispersed in the matrix. Before melt compounding S160 microparticles had a mean diameter of about 7–8 μm. Therefore, the shear forces acting on the highly porous precipitated silica microparticles during the compounding process led to their partial disgregation. This hypothesis is confirmed by similar observations on polymers filled by precipitated silica as reported by Shim and

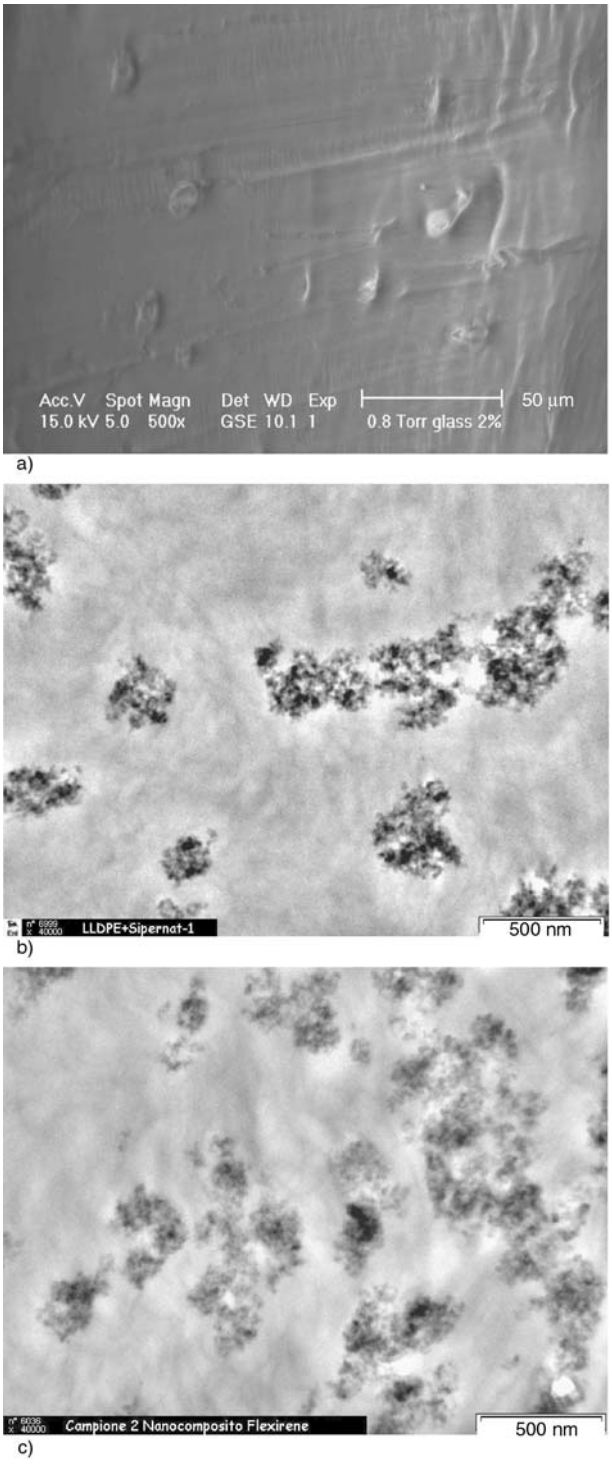

Figure 1. ESEM and TEM images of the fracture surfaces of LLDPE – 2 vol% composites: (a) LLDPE-Glass-2, (b) LLDPE-S160-2, (c) LLDPE-A380-2

Isayev for polydimethylsiloxane [47] and by Uotila *et al*. for polypropylene [48]. The mean diameter of S160 aggregates is comparable to that of A380 aggregates, consisting of isodimensional domains of about 200 nm homogeneously dispersed in the matrix. Therefore, despite the differences in the initial dimensions of the particles, the final micro-

structure of precipitated silica and fumed silica composites is very similar.

3.2. Rheological measurements

The effect of the filler content on the isothermal (190°C) frequency dependence of the dynamic shear storage modulus (G') of the prepared composites is reported in Figure 2. In the case of LLDPE-Glass-x samples, the typical rheological behaviour of microparticles filled polymers can be observed [50–53], with only a marginal improvement of G' in the entire frequency range. For precipitated silica composites the rheological behaviour is completely different. A strong G' enhancement can be easily detected even at relatively low silica content ($\Phi > 2$ vol%), especially in the low frequency region. These observations are in agreement with the existing scientific literature on the rheological properties of nanoparticles filled systems [1, 28, 29, 32, 33, 38, 54]. It is important to underline that G' of nanocomposites tends to become frequency independent in the low frequency region, which is the characteristic behaviour of an elastic solid (solid-like behaviour). According to Cassagnau [38], a similar trend observed in the low frequency region of polymer-clay nanocomposites can be attributed to strong interactions between the clay layers and the polymeric matrix, while the solid-like behaviour in fumed silica nanocomposites could be related to particle-particle interactions and to the consequent formation of a netlike structure. These interactions may arise from hydrogen bonds between the silanol groups on the surface of primary nanoparticles. As can be visualized in TEM images reported in Figure 1, fumed silica primary nanoparticles are fused together in aggregates, forming physical agglomerates with a diameter of 200–300 nm. In these conditions it is possible to hypothesize that the network

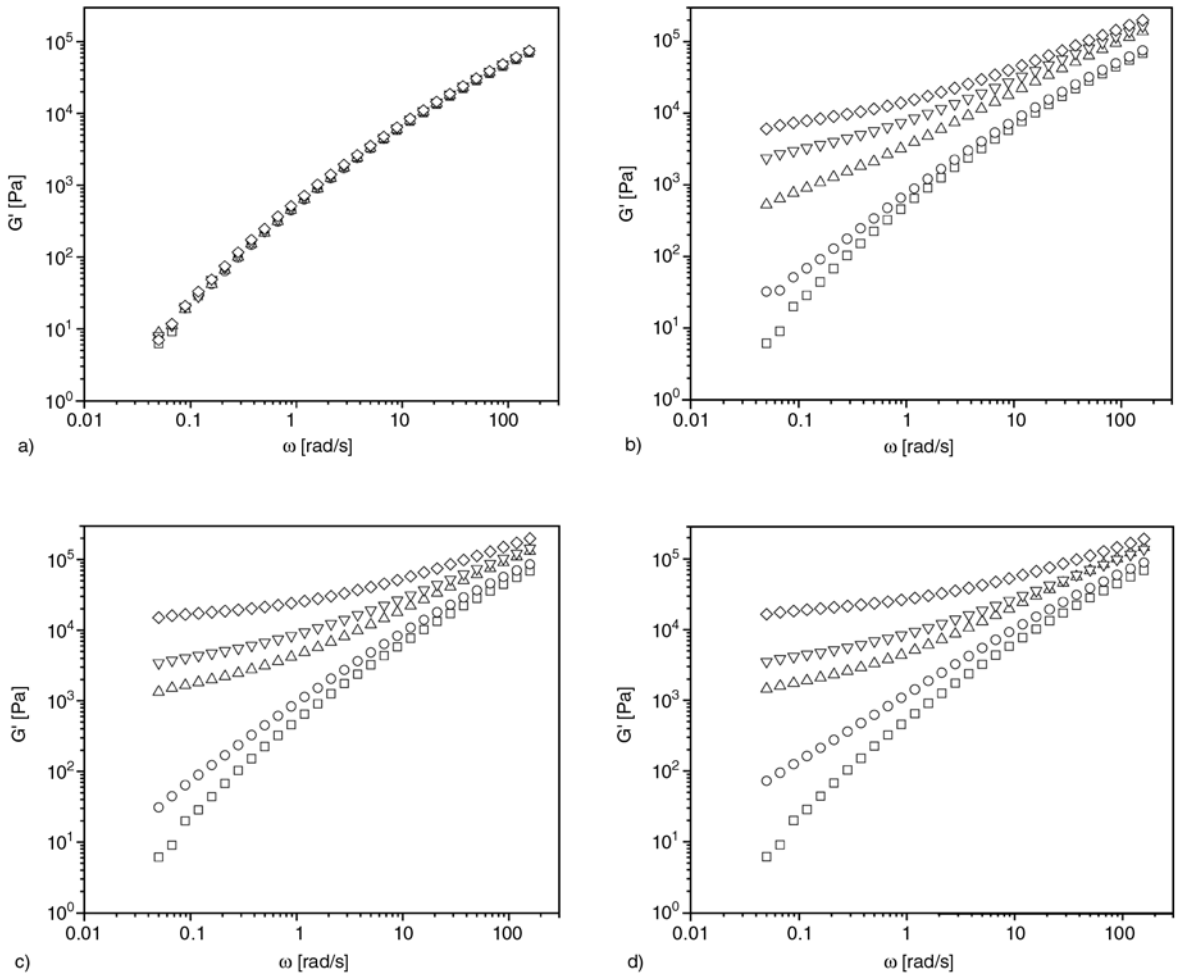

Figure 2. Storage modulus (G') curves of LLDPE and relative composites (T = 190°C): (a) LLDPE-Glass-x, (b) LLDPE-S160-x, (c) LLDPE-A200-x, (d) LLDPE-A380-x. (□) LLDPE, (○) x = 1 vol%, (△) x = 2 vol%, (▽) x = 3 vol%, (◇) x = 4 vol%.

responsible of the solid like behaviour shown by the nanofilled samples is formed by particle-particle interactions between silanol groups present on the surface of the nanoparticles. In this way the physical interactions between the agglomerates create a space filling network, able to block the flow of LLDPE macromolecules. At high test frequencies these bonds can be destroyed by shear forces, and the G' values approach those of the unfilled matrix. The same considerations hold also for fumed silica nanocomposites, but in this case the increase of G' values with the filler content is even more evident, especially when nanoparticles with high SSA values are used.

Loss tangent (tanδ) curves for pure LLDPE and relative micro- and nanocomposites are reported in Figure 3. Even in this case, the huge difference between the effects of glass microbeads and other fillers on the rheological behaviour of LLDPE is confirmed. If glass filled microcomposites are considered, the variation of the loss tangent is very limited even at high filler contents, while both precipitated and fumed silica induce a remarkable decrease of tanδ, accompanied by a shift of the peak of tanδ towards higher frequencies. The presence of a tanδ peak can be probably associated to the beginning of the breakdown of the silica network. Therefore, the little shift of the tanδ peak towards higher frequencies can be attributed to stronger interparticle interactions, favoured by the presence of a high number of silanol groups on the surface of the particles. Even in this case, the observed trend is more pronounced when fumed silica nanocomposites are considered, probably for the formation of an extended space filling silica network, due to the higher availability of silanol groups on the surface of primary nanoparticles. The hypothesis of the silica breakdown at tanδ peak is supported by various literature references. For example, Wu and Zheng [55] studied the dynamic rheological behaviour of HDPE/CB (carbon black) nanocomposites. They found that increasing the CB

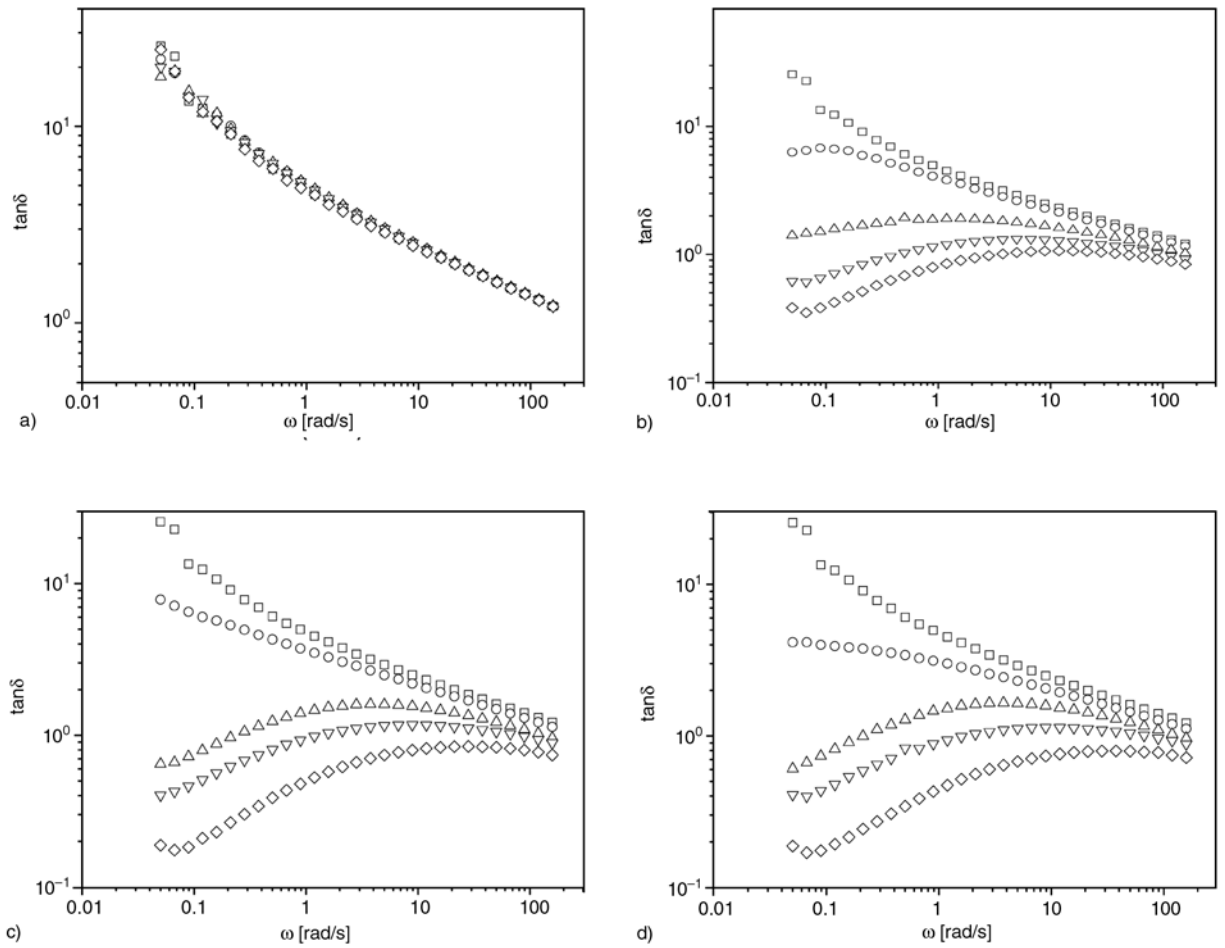

Figure 3. Loss tangent (tanδ) curves of LLDPE and relative composites (T = 190°C): (a) LLDPE-Glass-x, (b) LLDPE-S160-x, (c) LLDPE-A200-x, (d) LLDPE-A380-x. (□) LLDPE, (○) x = 1 vol%, (△) x = 2 vol%, (▽) x = 3 vol%, (◇) x = 4 vol%.

concentration, the plot of tanδ versus ω changed from linearity to an arc-shaped trend, with smaller tanδ values in the low frequency region. Considering that the peak of tanδ appeared for CB concentrations higher than 9 vol%, they defined this filler loading as a percolation threshold. Even in that case the magnitude of the peak decreased with an increase in the filler concentration, whereas tanδ values corresponding to the peak increased with the filler concentration. Romani *et al*. [56] attributed the existence of a tanδ peak to a critical relaxation behavior involved in a high-order structure within the polymer matrix, related to the existence of interparticle networks. Therefore, it is likely that similar considerations could be extended to LLDPE filled with aggregated physically interacting nanoparticles.

Figure 4 reports the frequency dependence of the shear viscosity for pure LLDPE and relative micro- and nanocomposites. Even in this case, only marginal viscosity increments can be detected for glass beads filled microcomposites, with the presence of a Newtonian plateau at low frequencies. For precipitated silica microcomposites and fumed silica nanocomposites viscosity enhancement is very pronounced, especially at low frequencies and for high silica loadings. The pseudoplastic plateau disappears for filler contents higher than 2 vol%, probably for the formation of a network of hydrogen bonded silica aggregates. The effect of fumed silica specific surface area can be evidenced only at low frequencies, with an increase of the shear viscosity as SSA increases. The increase of surface area may result in a higher number of silanol groups on the surface of the aggregates, leading to a higher number of hydrogen bonds and, consequently, to stronger particle-particle interactions. Therefore, the noticeable increase of shear viscosity values could be attributed to the interparticle interactions arising from hydrogen bonds between silanol groups present on the surface of the particles. This hypothesis is widely supported in the literature not only for suspensions, but also for filled polymer matrices in the molten state. As mentioned before, Cassagnau [38] concluded that the viscosity enhancement in polymer-clay nanocomposites was

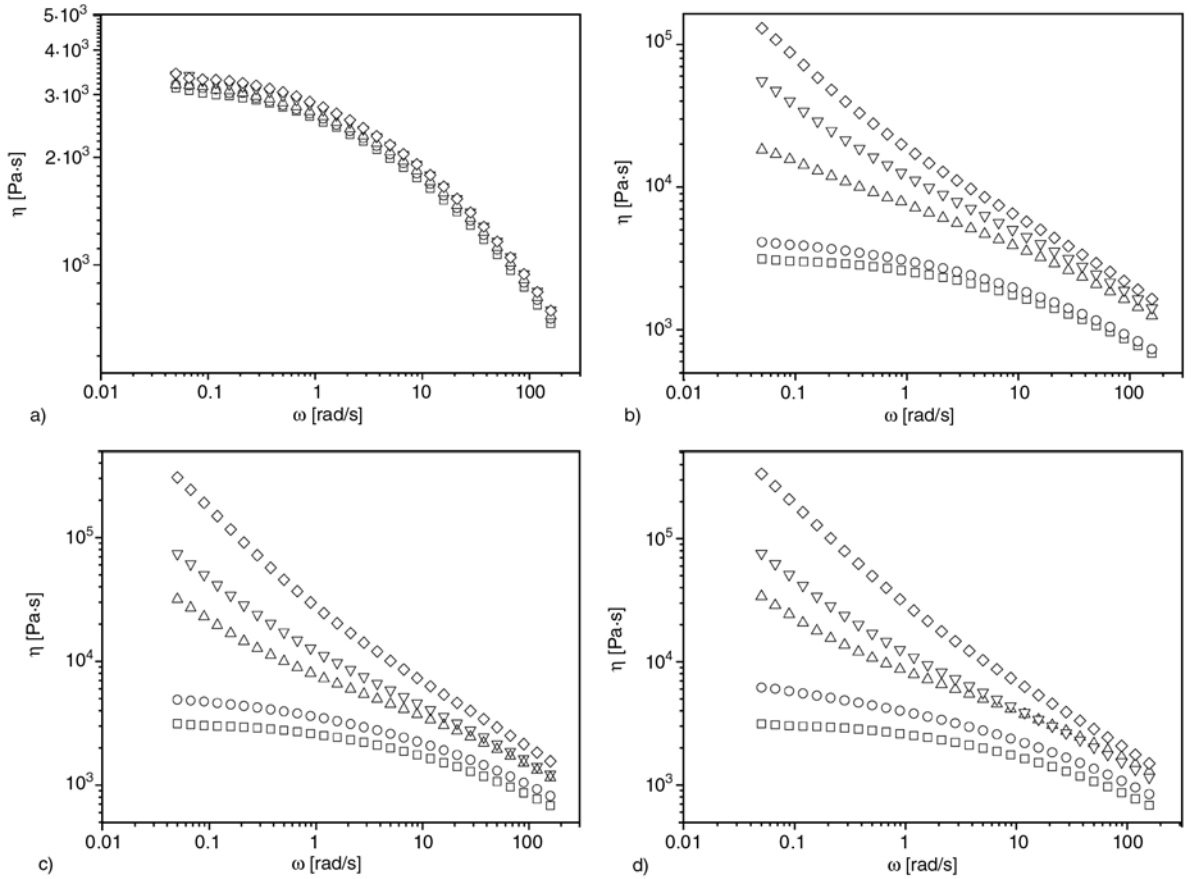

Figure 4. Viscosity (η) curves of LLDPE and relative composites (T = 190°C): (a) LLDPE-Glass-x, (b) LLDPE-S160-x, (c) LLDPE-A200-x, (d) LLDPE-A380-x. (□) LLDPE, (○) x = 1 vol%, (△) x = 2 vol%, (▽) x = 3 vol%, (◇) x = 4 vol%.

due to strong interactions between the clay layers and the polymeric matrix, while the solid-like behaviour in fumed silica nanocomposites was related to particle-particle interactions and to the subsequent formation of a netlike structure. This hypothesis is supported also by Bartholome [40], that considered filler networking due to the formation of hydrogen bonds as a first order parameter for silica nanocomposites based on common thermoplastics. Furthermore, considering that polyethylene has no polar groups in the main backbone, the possibility of having strong polymer-filler interactions and the physical absorption of polymer chains on the filler surface at the molten state appears relatively weak. Regarding the correlation between the viscosity drop and the destruction of the interparticle hydrogen bonds at high frequencies, it has to be considered that the higher the frequency the lower is the stress relaxation during each loading cycle and the higher is the stress acting transferred from the LLDPE matrix to the filler. This means that at high frequencies the energy involved to deform LLDPE macromolecules is much higher and perhaps superior to the energy required to break interparticle interactions. This hypothesis could also explain why the rheological behaviour of filled samples at high shear rates is similar to that of the unfilled matrix.

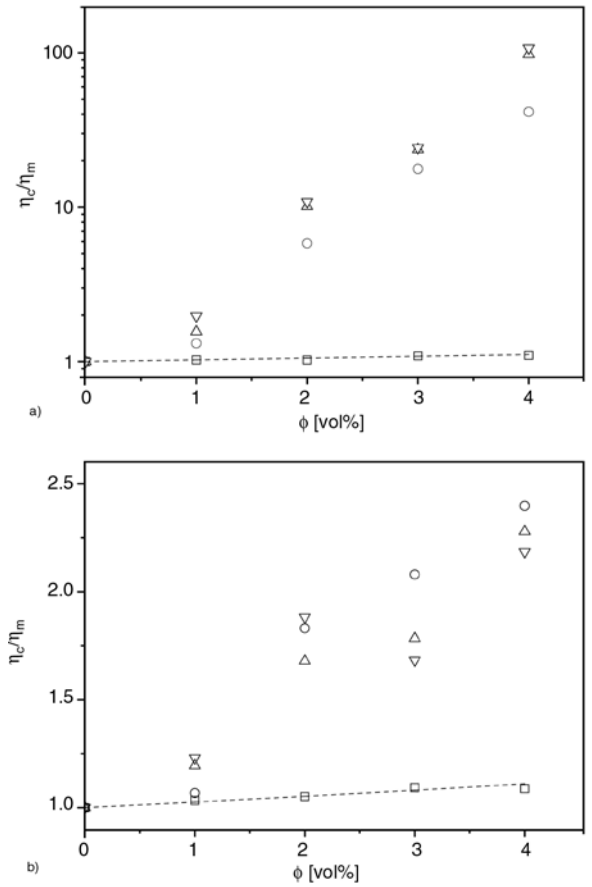

Figure 5. Relative viscosity values of LLDPE and relative composites (T = 190°C) at (a) ω = 0.05 rad/s and (b) ω = 158 rad/s. (□) LLDPE-Glass-x, (○) LLDPE-S160-x, (△) LLDPE-A200-x, (▽) LLDPE-A380-x. The dashed line represents the theoretical prediction of the relative viscosity according to the Batchelor model.

In order to better analyze the effect of the filler content on the rheological behaviour of the investigated micro and nanocomposites, relative viscosity at low (0.05 rad/s) and high (158 rad/s) frequencies has been reported in Figure 5 as a function of the volume content of the various fillers. It is clearly evident that the enhancement of the viscosity is much more pronounced at low frequencies, when the interparticle forces due to hydrogen bonding are more effective. While at 0.05 rad/s the viscosity of the LLDPE-A380-4 sample is about 100 times higher than that of the pure LLDPE, at 158 rad/s the viscosity of the same sample is only 2.4 times higher than that of the unfilled matrix. This confirms that in the high frequency regime the shear forces may lead to a breakage of the silica network, with a considerable reduction of viscosity values.

3.3. Modelling

Batchelor proposed a model to estimate the relative viscosity of polymer composites containing colloidal hard spheres in the limit of low shear rate, represented by the following Equation (1) [43]:

$$\frac{\eta_c}{\eta_m} = 1 + 2.5\Phi + 6.2\Phi^2 \quad (1)$$

where η_c and η_m are the viscosity of the composite and of the matrix, respectively. It can be easily noted that the proposed model is an extension of the Einstein equation [57], originally proposed to predict the effect of a rigid filler on the viscosity of a Newtonian liquid in the case of diluite suspension. Considering that the filler content in the prepared composites is relatively small (≤ 4 vol%), it is possible to use the above mentioned expression in order to fit shear viscosity data, as reported in Figure 5. It is immediately evident that the Batchelor model is able to fit the viscosity trend of glass filled LLDPE composites, both in the low and in the high frequency regions, while in the case of precipitated

silica and fumed silica composites the increase in relative viscosity is largely underestimated. As it could be expected, this model is unsuitable to catch the dependence of the rheological behaviour of polymeric nanocomposites from the filler content.

In the last decades quite a variety of empirical non-Newtonian viscosity models, constituted by 2, 3, 4 or 5 elements, have been proposed to analyze the frequency dependence of the shear viscosity of polymers [51]. For the materials investigated in this work the difficulty to find a suitable expression arises from the markedly different viscosity trends between unfilled LLDPE and fumed silica nanocomposites, due to the disappearance of the pseudo-plastic plateau in the low frequency regime.

From a historical point of view, the first attempt to solve the problems related to the appearance of an yield stress at vanishing shear rates was made by Bingham [58] in 1922, that proposed a model with two distinct constitutive equations to describe the rheological behaviour of the material at rest and during the flow. As reported by Malkin [53], the abovementioned expression should not be intended as rheological equation of state, because it only contains an empirical description of experimental data obtained in unidimensional shear deformations. Also Barnes [50] specified that this law is basically empirical in nature and arising from curve-fitting exercises. Furthermore, the same authors underlined that the derived equation could be applied over limited parts of the flow curve, and care should be taken in the use of these models when employed outside a certain shear rate range. However, Bingham model did not prove to be suitable for numerical analysis because in some complex applications parts of material flow while the rest behaves as a solid, with considerable difficulties in applying two different constitutive equations across them. To overcome these issues, Papanastasiou [59] proposed a modification of the Bingham model, but his expression resulted to be not sufficiently effective in predicting the rheological behavior of shear thinning fluids with a yield stress, typical of complex fluids. More recently, Mitsoulis *et al.* [45] modified the Herschel-Bulkley model [60] to predict shear thinning behavior of complex fluids, with an expression reported in Equation (2):

$$\eta = k\omega^{n-1} + \tau_0\omega^{-1}[1-e^{-m\omega}] \quad (2)$$

It is evident that when the parameter n is less than one, which is the typical case for shear-thinning fluids, the apparent viscosity tends to infinity when the shear rate tends to zero. Moreover, the dimension of parameter k depends on parameter n. This may cause a problem when constructing a parameter with the unit of time based on the parameters k and n [51]. In 1980, De Kee and Turcotte proposed a three-parameter model [44] described by the following Equation (3):

$$\eta = \tau_0\omega^{-1} + \eta_1 e^{-t_1\omega} \quad (3)$$

The first term on the right side of the equation includes a constant yield stress τ_0. This parameter is closely related to the breakage of the solid network formed by silica aggregates. The limiting viscosity η_1 represents the zero-shear viscosity value when the solid network is absent, while t_1 is a characteristic time, related to the velocity of the viscosity drop at high frequencies. Even in this case characteristic time and limiting viscosity were presented by the authors as empirical parameters, with no evident physical meaning or correlation with material parameters. Carreau underlined that η_1 and t_1 had to be intended as analytical model parameters and not as real material properties [51]. In the scientific literature it is often reported that this model fits very well viscosity data in the low frequency region, while deviations may be expected when the high frequency region is considered [52].

As reported in Equation (4), a modification of the original De Kee-Turcotte model has been proposed by Zhu *et al.* [46], in order to predict a finite value of the apparent viscosity when the shear rate approaches zero:

$$\eta = \tau_0\omega^{-1}[1-e^{-m\omega}] + \eta_1 e^{-t_1\omega} \quad (4)$$

In this expression, the dimensions of the parameters involved are independent of each other, and the apparent viscosity is bounded at vanishing shear rate. Even in this case the authors proposed this model without attributing any physical meaning to the various parameters of the expression, and the comparison with the previous models was carried out only on the basis of their fitting capabilities.

Considering the need of proper empirical models that could satisfactorily describe the dynamic rheological behaviour of polymer melts in a certain shear rate region, we are proposing a modification of the original De Kee-Turcotte expression in order

to obtain a satisfactory fitting of the rheological data in the high frequency region. In particular, the following empirical Equation (5) is proposed:

$$\eta = \tau_0 \omega^{-1} + \eta_1 e^{-t_1 \omega^{\alpha}} \quad (5)$$

It can be noted that a new parameter α is introduced the second term of the De Kee-Turcotte equation. This should improve the ability of the model to follow the non-linear viscosity drop at high frequencies as observed for the nanocomposites at high filler contents.

The fitting capabilities of the above mentioned models (Equations 2 to 5) are compared in Figure 6 in the case of pure LLDPE and A380 filled samples, while Table 2 summarizes the coefficient of linear regression (R^2) for the various fitting curves. It is evident that the expression proposed by Mitsoulis-Abdali (Equation 2) provides a good fitting for the pure LLDPE ($R^2 = 0.9961$), while viscosity values of LLDPE-A380-2 samples in the high frequency region are underestimated. As displayed in Figure 6c, this expression is not suitable to model the experimental data of nanocomposites at relatively high filler contents. As previously reported by other authors [52], even our data confirm that the original De Kee-Turcotte model (Equation 3) is not able to catch the rheological trends in the high frequency region, especially when a high amount of silica is added. The generalization proposed by Zhu (Equation 4), seems to improve the prediction capability of this model, even if some deviations are still evident in the high frequency region. It is evident that our model (Equation 5) is able to satisfactorily fit the viscosity data over the entire frequency range both for pure LLDPE and relative fumed silica nanocomposites (R^2 values higher than 0.999). The model proposed in this paper provides a satisfactory fitting of the viscosity–frequency curves for all the investigated materials (see Figure 7). In the case of the pure LLDPE sample, the experimental viscosity trend in the high frequencies region is not linear and can be modelled by a simple ω^{α} dependency, with the introduction of the α parameter that helps to fit more accurately the viscosity drop. For relatively high filler loadings

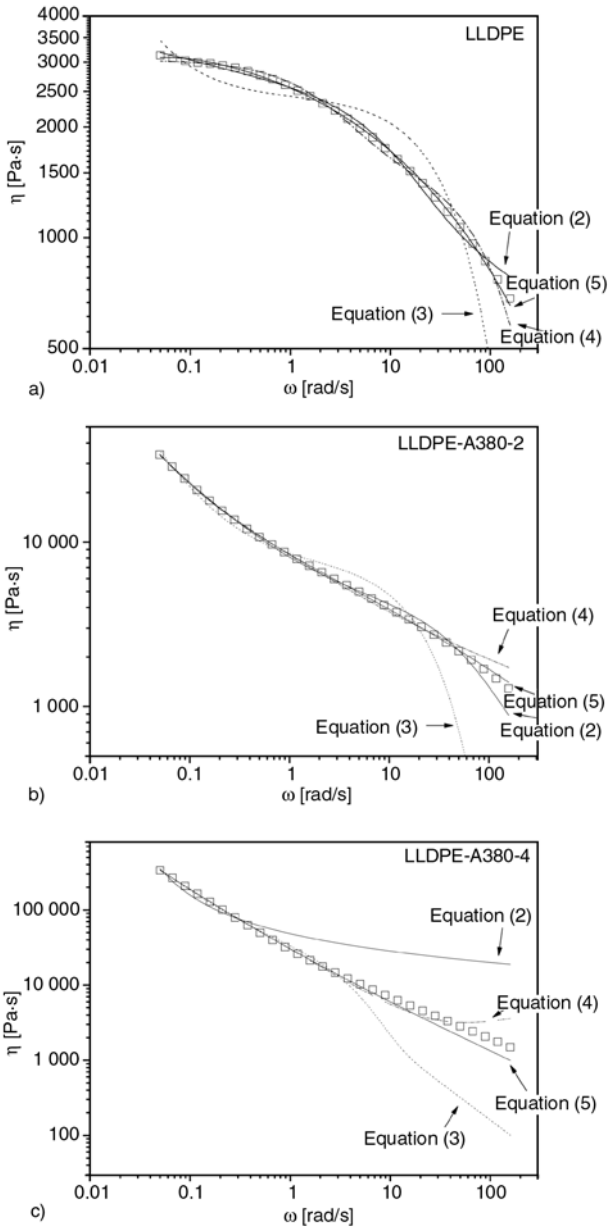

Figure 6. Experimental viscosity (η) curves of (a) pure LLDPE, (b) LLDPE-A380-2 and (c) LLDPE-A380-4 nanocomposites (T = 190°C), with the fitting lines according to various models. Mitsoulis-Abdali model (Equation (2)), De Kee-Turcotte model (Equation (3)), Zhu model (Equation (4)), and the new model proposed in this work (Equation (5)).

Table 2. R^2 values from the fitting of shear viscosity data of LLDPE, LLDPE-A380-2 and LLDPE-A380-4 samples with different models

	Mitsoulis-Abdali (Equation (2))	**De Kee-Turcotte (Equation (3))**	**Zhu (Equation (4))**	**Our model (Equation (5))**
LLDPE	0.9962	0.8953	0.9952	0.9994
LLDPE-A380-2	0.9994	0.9839	0.9993	0.9999
LLDPE-A380-4	0.9441	0.9983	0.9997	0.9998

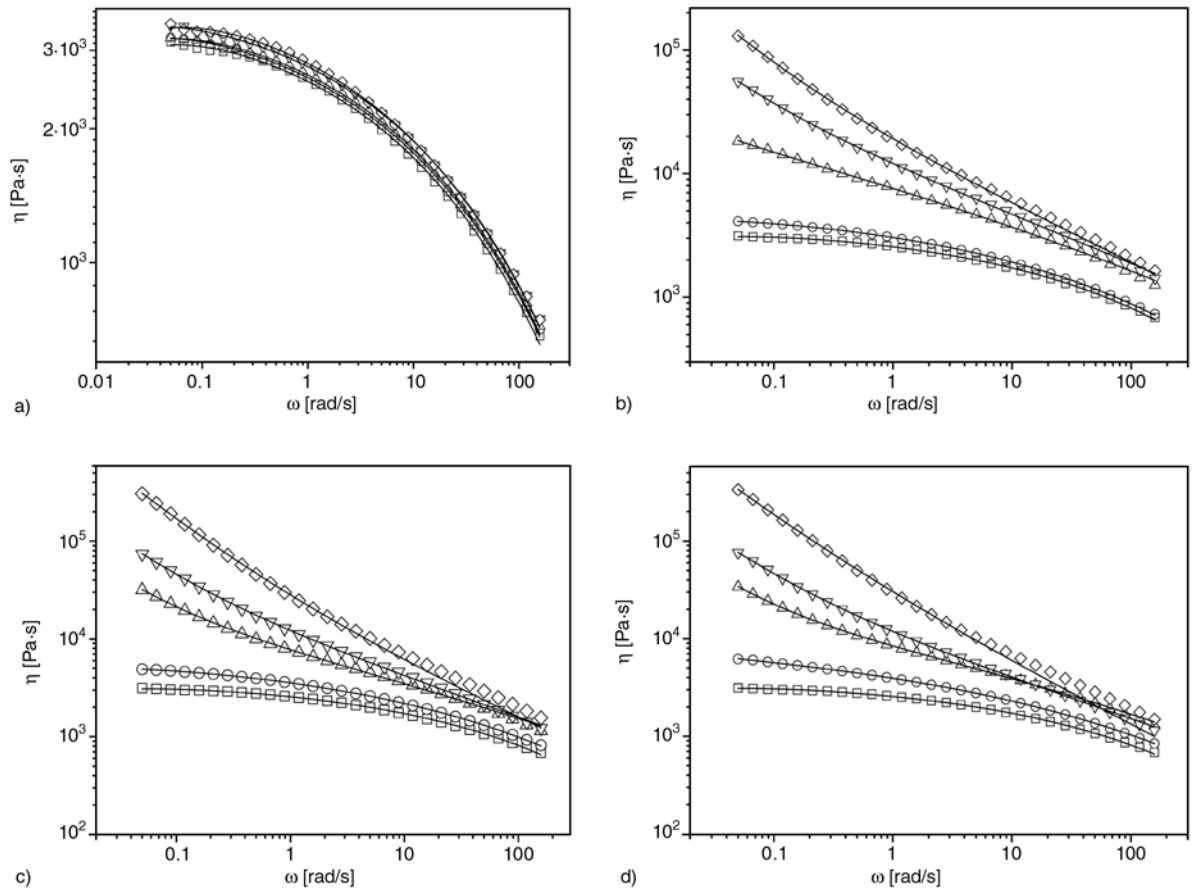

Figure 7. Experimental viscosity (η) curves of LLDPE and relative composites (T = 190°C). (a) LLDPE-Glass-x, (b) LLDPE-S160-x, (c) LLDPE-A200-x, (d) LLDPE-A380-x. (□) LLDPE, (○) x = 1 vol%, (Δ) x = 2 vol%, (▽) x = 3 vol%, (◇) x = 4 vol%. The continuous lines represent the fitted data according to the Modified De Kee-Turcotte model.

($\Phi > 2$ vol%) the value of t_1 tends to infinity and the second term of equation is practically zero. This means that the viscosity values are basically inversely proportional to the frequency. Considering the relatively high shear stress values for these composites, in the high frequency region viscosity values approach to zero with a trend similar to that of a line with a negative slope. This is the reason why in the considered frequency range the proposed model can be utilized both for the unfilled sample and for the nanocomposites.

Some additional considerations can be formulated by examining Figure 8, in which the influence of the filler content and type on the fitting parameters of Equation (5) is represented. A non-zero yield stress parameter (τ_0) can be related to the presence of a filler network in the material [51, 52]. As documented in Figure 8a, it is evident that yield stress (τ_0) is practically zero for pure LLDPE and glass filled composites. For precipitated silica filled composites yield stress starts to increase after a filler content of 2 vol%, while for fumed silica nanocomposites the enhancement of parameter τ_0 is evident even at a filler loading of 1 vol%. Therefore, the silica concentration after which yield stress increases can be interpreted as a percolation threshold, a critical filler loading after which the interparticle interactions may lead to the formation of a solid space filling network, and the viscosity greatly increases. In other words, the existence of a critical silica concentration above which the distance between the agglomerates is sufficiently low to allow the formation of a space filling network can be hypothesized. The appearance of a yield stress in shear viscosity curves for silica contents higher than 1 vol% is a direct proof of the network formation.

After the percolation threshold, traditional pseudoplastic behaviour of LLDPE, with a Newtonian plateau in the low frequency regime, disappears. Similar considerations hold for the limiting viscosity parameter η_1. For pure LLDPE and glass filled

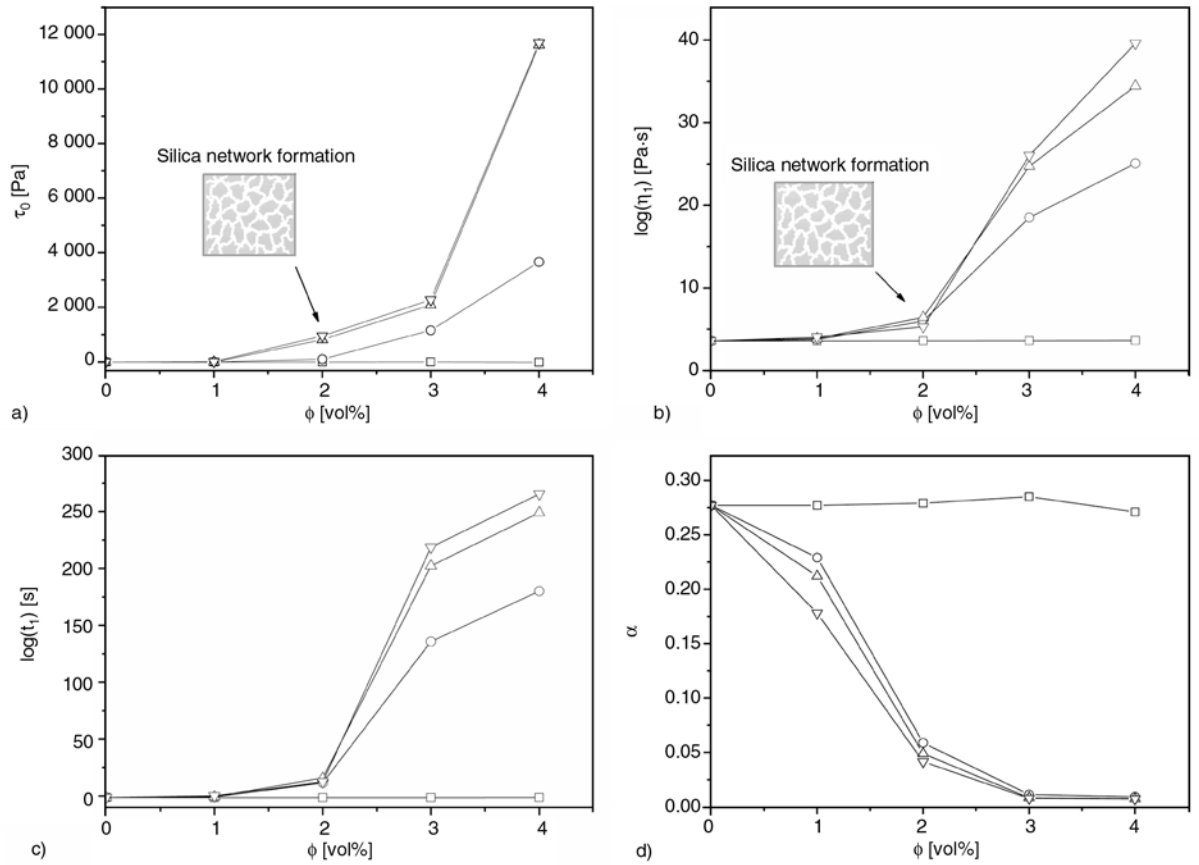

Figure 8. Evaluation of the Modified De Kee-Turcotte parameters derived from the fitting of the viscosity curves of LLDPE and relative composites: (a) τ_0, (b) η_1, (c) t_1, (d) α. (□) LLDPE-Glass-x, (○) LLDPE-S160-x, (△) LLDPE-A200-x, (▽) LLDPE-A380-x.

composites this parameter assumes a value of about 3000–4000 Pa·s, and it can be considered as the zero shear viscosity. For the other composites η_1 begins to increase for filler contents as low as 2 vol%. It is important to underline that at elevated silica volume fractions (3–4 vol%) η_1 value is around 10^{30} Pa·s, i.e. a typical viscosity value of a solid material. Even t_1 confirms this picture. In fact, this parameter rules the viscosity drop at high frequencies. For glass filled composites t_1 is practically the same of unfilled LLDPE, while for precipitated and fumed silica composites the characteristic time begins to increase for a silica loading higher than 2 vol%. Considering that the evaluation of the fitting parameters was carried out from an analytical point of view, the representation of the t_1 parameter with values of 10 up to the power 200 for the nanofilled samples underlines the fact that at high silica contents t_1 tends to infinity and the second term of the equation approaches to zero, leading to a ω^{-1} dependency with an high yield stress value. For the same reason α parameter is practically insensitive to the filler content for glass filled composites, while for precipitated and fumed silica filled samples α considerably drops with the filler content.

4. Conclusions

The effect of the filler morphology (mean particle size and surface area) on the dynamic rheological properties of LLDPE/silica micro- and nanocomposites was investigated on melt compounded samples.

TEM images revealed that fumed silica and precipitated silica composites are characterized by similar microstructures, with the presence of spherical silica aggregates homogeneously dispersed in the matrix, having a mean diameter lower than 400 nm. On the other hand, in traditional glass microcomposites spherical smooth microparticles, with mean size of about 15–20 μm, can be easily detected. The dispersion of silica aggregates at the nanoscale was strictly correlated to the rheological behaviour of the composites. While in the case of glass microbeads filled samples only marginal effects on

dynamic rheological properties could be detected, a very strong enhancement of the storage modulus (G') and of the viscosity (η) with the filler content, especially at low frequencies, was evidenced for fumed silica and precipitated silica composites, while loss tangent values were strongly reduced, with a shift of the tanδ peak towards higher frequencies. It was hypothesized that particle-particle interactions, arising from hydrogen bonds of silanolic groups present on the surface of primary nanoparticles, were effective in nanofilled samples, creating a space filling network able to block the viscous flow of LLDPE macromolecules.

Trying to find a suitable non-Newtonian model to fit shear viscosity data, a new empirical expression, based on a modification of the original three-parameter model proposed by De Kee and Turcotte, was successfully proposed. While in the case of glass filled samples fitting parameters were only marginally affected by the filler addition, when precipitated silica and fumed silica composites were considered a strong correlation with the filler loading was found.

References

[1] Sarvestani A. S.: Modeling the solid-like behavior of entangled polymer nanocomposites at low frequency regimes. European Polymer Journal, **44**, 263–269 (2008).
DOI: 10.1016/j.eurpolymj.2007.11.023

[2] Harzallah O., Dupuis D.: Rheological properties of suspensions of TiO_2 particles in polymer solutions. 1. Shear viscosity. Rheologica Acta, **42**, 10–19 (2003).
DOI: 10.1007/s00397-002-0250-2

[3] Le Meins J-F., Moldenaers P., Mewis J.: Suspensions in polymer melts. 1. Effect of particle size on the shear flow behavior. Industrial and Engineering Chemistry, **41**, 6297–6304 (2002).
DOI: 10.1021/ie020117r

[4] Osman M. A., Atallah A.: Interparticle and particle-matrix interactions in polyethylene reinforcement of viscoelasticity. Polymer, **46**, 9476–9488 (2005).
DOI: 10.1016/j.polymer.2005.07.030

[5] Osman M. A., Atallah A.: Effect of the particles size on the viscoelastic properties of filled polyethylene. Polymer, **47**, 2357–2368 (2006).
DOI: 10.1016/j.polymer.2006.01.085

[6] Zhang Q., Archer L. A.: Optical polarimetry and mechanical rheometry of polyethyleneoxide-silica dispersions. Macromolecules, **37**, 1928–1936 (2004).
DOI: 10.1021/ma035667v

[7] Zhu T., Thompson T., Wang S-Q., von Meerwall E. D., Halasa A.: Investigating linear and nonlinear viscoelastic behavior using model silica-particle-filled polybutadiene. Macromolecules, **38**, 8816–8824 (2005).
DOI: 10.1021/ma050922s

[8] Aranguren M. I., Mora E. M., DeGroot J. V., Macosko C. W.: Effect of reinforcing fillers on the rheology of polymer melts. Journal of Rheology, **36**, 1165–1182 (1992).
DOI: 10.1122/1.550306

[9] Cassagnau P., Melis F.: Non-linear viscoelastic behaviour and modulus recovery in silica filled polymers. Polymer, **44**, 6607–6615 (2003).
DOI: 10.1016/S0032-3861(03)00689-X

[10] Zhang Q., Archer L. A.: Poly(ethylene oxide)/silica nanocomposites: Structure and rheology. Langmuir, **18**, 10435–10442 (2002).
DOI: 10.1021/la026338j

[11] Kohl D. J., Beaucage G.: Rational design of reinforced rubber. Current Opinion in Solid State and Materials Science, **6**, 183–194 (2002).
DOI: 10.1016/S1359-0286(02)00073-6

[12] Medalia A.: Morphology of aggregates: VI Effective volume of aggregates of carbon black from electron microscopy; Application to vehicle absorption and to die swell of filled rubber. Journal of Colloid and Interface Science, **32**, 115–131 (1970).
DOI: 10.1016/0021-9797(70)90108-6

[13] Osman M. A., Atallah A., Schweizer T., Ottinger H. C.: Particle-particle and particle-matrix interactions in calcite filled high-density polyethylene-steady shear. Journal of Rheology, **48**, 1167–1184 (2004).
DOI: 10.1122/1.1784782

[14] Piau J-M., Dorget M., Palierne J-F., Pouchelon A.: Shear elasticity and yield stress of silica-silicone physical gels: Fractal approach. Journal of Rheology, **43**, 305–314 (1999).
DOI: 10.1122/1.550989

[15] Witten T. A., Rubinstein M., Colby R. H.: Reinforcement of rubber by fractal aggregates. Journal de Physique II, **3**, 367–383 (1993).
DOI: 10.1051/jp2:1993138

[16] Wolthers W., van den Ende D., Breedveld V., Duits M. H. G., Potanin A., Wientjes R. H. W., Mellema J.: Linear viscoelastic behavior of aggregated colloidal dispersions. Physical Review E, **56**, 5726–5733 (1997).
DOI: 10.1103/PhysRevE.56.5726

[17] Havet G., Isayev A.: A thermodynamic approach to the rheology of highly interactive filler-polymer mixtures: Part I Theory. Rheologica Acta, **40**, 570–581 (2001).
DOI: 10.1007/s003970100176

[18] Havet G., Isayev A.: A thermodynamic approach to the rheology of highly interactive filler-polymer mixtures. Part II. Comparison with polystyrene/nanosilica mixtures. Rheologica Acta, **42**, 47–55 (2003).
DOI: 10.1007/s00397-002-0253-z

[19] Montes H., Lequeux F., Berriot J.: Influence of the glass transition temperature gradient on the nonlinear viscoelastic behavior in reinforced elastomers. Macromolecules, **36**, 8107–8118 (2003).
DOI: 10.1021/ma0344590

[20] Pryamitsyn V., Ganesan V.: Mechanisms of steady-shear rheology in polymer-nanoparticle composites. Journal of Rheology, **50**, 655–683 (2006).
DOI: 10.1122/1.2234483

[21] Pryamitsyn V., Ganesan V.: Origins of linear viscoelastic behavior of polymer-nanoparticle composites. Macromolecules, **39**, 844–856 (2006).
DOI: 10.1021/ma051841z

[22] Simhambhatla M., Leonov A.: On the rheological modeling of filled polymers with particle-matrix interactions. Rheologica Acta **34**, 329–338 (1995).
DOI: 10.1007/BF00367150

[23] Dazhu C., Haiyang Y., Pingsheng H., Weian Z.: Rheological and extrusion behavior of intercalated high-impact polystyrene/organomontmorillonite nanocomposites. Composites Science and Technology, **65**, 1593–1600 (2005).
DOI: 10.1016/j.compscitech.2005.01.011

[24] Durmus A., Kasgoz A., Macosko C. W.: Linear low density polyethylene (LLDPE)/clay nanocomposites. Part I: Structural characterization and quantifying clay dispersion by melt rheology. Polymer, **48**, 4492–4502 (2007).
DOI: 10.1016/j.polymer.2007.05.074

[25] Gupta R. K., Pasanovic-Zujo V., Bhattacharya S. N.: Shear and extensional rheology of EVA/layered silicate-nanocomposites. Journal of Non-Newtonian Fluid Mechanics, **128**, 116–125 (2005).
DOI: 10.1016/j.jnnfm.2005.05.002

[26] Krishnamoorti R., Yurekli K.: Rheology of polymer layered silicate nanocomposites. Current Opinion in Colloid and Interface Science, **6**, 464–470 (2001).
DOI: 10.1016/S1359-0294(01)00121-2

[27] Ray S. S., Yamada K., Okamoto M., Ueda K.: New polylactide-layered silicate nanocomposites. 2. Concurrent improvements of material properties, biodegradability and melt rheology. Polymer, **44**, 857–866 (2003).
DOI: 10.1016/S0032-3861(02)00818-2

[28] Sepehr M., Utracki L. A., Zheng X., Wilkie C. A.: Polystyrenes with macro-intercalated organoclay. Part II. Rheology and mechanical performance. Polymer, **46**, 11569–11581 (2005).
DOI: 10.1016/j.polymer.2005.10.032

[29] Wu D., Wu L., Wu L., Zhang M.: Rheology and thermal stability of polylactide/clay nanocomposites. Polymer Degradation and Stability, **91**, 3149–3155 (2006).
DOI: 10.1016/j.polymdegradstab.2006.07.021

[30] Zhao J., Morgan A. B., Harris J. D.: Rheological characterization of polystyrene-clay nanocomposites to compare the degree of exfoliation and dispersion. Polymer, **46**, 8641–8660 (2005).
DOI: 10.1016/j.polymer.2005.04.038

[31] Zhong Y., Zhu Z., Wang S. Q.: Synthesis and rheological properties of polystyrene/layered silicate nanocomposite. Polymer, **46**, 3006–3013 (2005).
DOI: 10.1016/j.polymer.2005.02.014

[32] Abdel-Goad M., Pötschke P.: Rheological characterization of melt processed polycarbonate multiwalled carbon nanotube composites. Journal of Non-Newtonian Fluid Mechanics, **128**, 2–6 (2005).
DOI: 10.1016/j.jnnfm.2005.01.008

[33] Ganß M., Satapathy B. K., Thunga M., Weidisch R., Pötschke P., Jehnichen D.: Structural interpretations of deformation and fracture behavior of polypropylene/multi-walled carbon nanotube composites. Acta Materialia, **56**, 2247–2261 (2008).
DOI: 10.1016/j.actamat.2008.01.010

[34] Hu G., Zhao C., Zhang S., Yang M., Wang Z.: Low percolation thresholds of electrical conductivity and rheology in poly(ethylene terephthalate) through the networks of multi-walled carbon nanotubes. Polymer, **47**, 480–488 (2006).
DOI: 10.1016/j.polymer.2005.11.028

[35] Prashantha K., Soulestin J., Lacrampe M. F., Claes M., Dupin G., Krawczak P.: Multi-walled carbon nanotube filled polypropylene nanocomposites based on masterbatch route: Improvement of dispersion and mechanical properties through PP-g-MA addition. Express Polymer Letters, **2**, 735–745 (2008).
DOI: 10.3144/expresspolymlett.2008.87

[36] Prashantha K., Soulestin J., Lacrampe M. F., Krawczak P., Dupin G., Claes M.: Masterbatch-based multi-walled carbon nanotube filled polypropylene nanocomposites: Assessment of rheological and mechanical properties. Composites Science and Technology, **69**, 1756–1763 (2009).
DOI: 10.1016/j.compscitech.2008.10.005

[37] Song Y. S.: Rheological characterization of carbon nanotubes/poly(ethylene oxide) composites. Rheologica Acta, **46**, 231–238 (2006).
DOI: 10.1007/s00397-006-0137-8

[38] Cassagnau P.: Melt rheology of organoclay and fumed silica nanocomposites. Polymer, **49**, 2183–2196 (2008).
DOI: 10.1016/j.polymer.2007.12.035

[39] Kontou E., Niaounakis M.: Thermo-mechanical properties of LLDPE/SiO_2 nanocomposites. Polymer, **47**, 1267–1280 (2006).
DOI: 10.1016/j.polymer.2005.12.039

[40] Bartholome C., Beyou E., Bourgeat-Lami E., Cassagnau P., Chaumont P., David L., Zydowicz N.: Viscoelastic properties and morphological characterization of silica/polystyrene nanocomposites synthesized by nitroxide-mediated polymerization. Polymer, **46**, 9965–9973 (2005).
DOI: 10.1016/j.polymer.2005.07.057

[41] Cassagnau P.: Payne effect and shear elasticity of silica-filled polymers in concentrated solutions and in molten state. Polymer, **44**, 2455–2462 (2003).
DOI: 10.1016/S0032-3861(03)00094-6

[42] Inoubli R., Dagréou S., Lapp A., Billon L., Peyrelasse J.: Nanostructure and mechanical properties of polybutylacrylate filled with grafted silica particles. Langmuir, **22**, 6683–6689 (2006).
DOI: 10.1021/la0607003

[43] Batchelor G. K.: The effect of the Brownian motion on the bulk stress in a suspension of spherical particles. Journal of Fluid Mechanics, **83**, 97–117 (1977).
DOI: 10.1017/S0022112077001062

[44] De Ké D., Turcotte G.: Viscosity of biomaterials. Chemical Engineering Communications, **6**, 273–282 (1980).
DOI: 10.1080/00986448008912535

[45] Mitsoulis E., Abdali S. S., Markatos N. C.: Flow simulation of Herschel-Bulkley fluids through extrusion dies. The Canadian Journal of Chemical Engineering, **71**, 147–160 (1993).
DOI: 10.1002/cjce.5450710120

[46] Zhu H., Kim Y. D., De Kee D.: Non-Newtonian fluids with a yield stress. Journal of Non-Newtonian Fluid Mechanics, **129**, 177–181 (2005).
DOI: 10.1016/j.jnnfm.2005.06.001

[47] Shim S. E., Isayev A. I.: Rheology and structure of precipitated silica and poly(dimethyl siloxane) system. Rheologica Acta, **43**, 127–136 (2004).
DOI: 10.1007/s00397-003-0327-6

[48] Uotila R., Hippi U., Paavola S., Seppälä J.: Compatibilization of PP/elastomer/microsilica composites with functionalized polyolefins: Effect on microstructure and mechanical properties. Polymer, **46**, 7923–7930 (2005).
DOI: 10.1016/j.polymer.2005.06.099

[49] Brunauer S., Emmett P. H., Teller E.: Adsorption of gases in multimolecular layers. Journal of American Chemical Society, **60**, 309–319 (1938).

[50] Barnes H. A., Hutton J. F., Walters K.: An introduction to rheology. Elsevier, Amsterdam (1989).

[51] Carreau P. J., De Kee D. C. R., Chhabra R. P.: Rheology of polymeric systems. Hanser, Munich (1997).

[52] Gupta R. K.: Polymer and composite rheology. Marcel Dekker, New York (2000).

[53] Malkin A. Y.: Rheology fundamentals. ChemTech Publishing, Toronto (Canada) (1994).

[54] Renger C., Kuschel P., Kristoffersson A., Clauss B., Oppermann W., Sigmund W.: Rheology studies on highly filled nano-zirconia suspensions. Journal of the European Ceramic Society, **27**, 2361–2367 (2007).
DOI: 10.1016/j.jeurceramsoc.2006.08.022

[55] Wu G., Zheng Q.: Estimation of the agglomeration structure for conductive particles and fiber-filled high-density polyethylene through dynamic rheological measurements. Journal of Polymer Science Part B: Polymer Physics, **42**, 1199–1205 (2004).
DOI: 10.1002/polb.10773

[56] Romani F., Corrieri R., Braga V., Ciardelli F.: Monitoring the chemical crosslinking of propylene polymers through rheology. Polymer, **43**, 1115–1131 (2002).
DOI: 10.1016/S0032-3861(01)00679-6

[57] Einstein A.: Investigations on the theory of the brownian movement. Dover Publications, New York (1956).

[58] Bingham E. C.: Fluidity and plasticity. McGraw-Hill, New York (1922).

[59] Papanastasiou T. C.: Flows of materials with yield. Journal of Rheology, **31**, 385–404 (1987).

[60] Herschel W. H., Bulkley R.: Konsistenzmessungen von Gummi-Benzol-Losungen. Colloid and Polymer Science, **39**, 291–300 (1926).
DOI: 10.1007/BF01432034